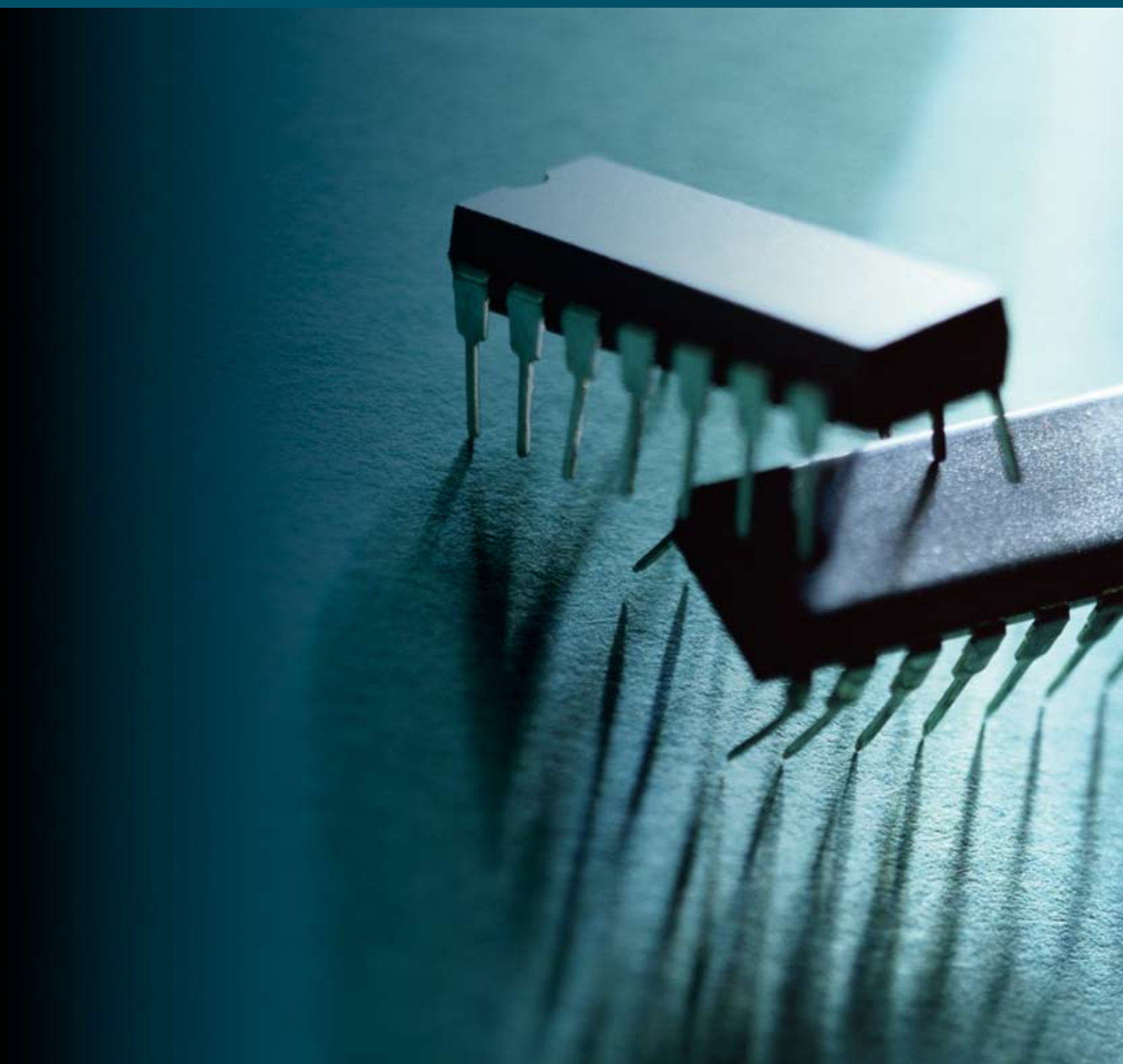


Active and Passive Electronic Components

Active and Passive Microwave Devices and Circuits

Guest Editors: T. S. Kalkur, Tibor Bercei, and Fahrettin Yakuphanoglu





Active and Passive Microwave Devices and Circuits

Active and Passive Electronic Components

Active and Passive Microwave Devices and Circuits

Guest Editors: T. S. Kalkur, Tibor Berceci,
and Fahrettin Yakuphanoglu



Copyright © 2008 Hindawi Publishing Corporation. All rights reserved.

This is a special issue published in volume 2008 of "Active and Passive Electronic Components." All articles are open access articles distributed under the Creative Commons Attribution License, which permits unrestricted use, distribution, and reproduction in any medium, provided the original work is properly cited.

Editor-in-Chief

T. S. Kalkur, University of Colorado, USA

Associate Editors

Abu Khari A'ain, Malaysia
Spartak Gevorgian, Sweden
Ashok K. Goel, USA
S. B. Krupanidhi, India
Brock J. La Meres, USA

John Lindsey, USA
Yicheng Lu, USA
Yalin Lu, USA
Chem Nayar, Australia
Adam Pawlikiewicz, USA

Krishnamachar Prasad, New Zealand
Tian-Ling Ren, China
Jose' A. Siqueira Dias, Brazil
Tai-Bor Wu, Taiwan
Fahrettin Yakuphanoglu, Turkey

Contents

Active and Passive Microwave Devices and Circuits, T. S. Kalkur, Tibor Berceli,
and Fahrettin Yakuphanoglu
Volume 2008, Article ID 320956, 2 pages

Dependence on Frequency of the Electromagnetic Field Distribution inside a Cylindrical Cavity Excited through an Off-Axis Aperture, Fabrizio Consoli, Luigi Celona, Giovanni Ciavola,
Santo Gammino, Fabio Maimone, Rocco Salvatore Catalano, Sebastiano Barbarino, David Mascali,
and Livia Tumino
Volume 2008, Article ID 859052, 4 pages

Printed Antenna Arrays with High Side Lobe Suppression, Aleksandar Nešić, Ivana Radnović,
and Zoran Mičić
Volume 2008, Article ID 542929, 6 pages

Isotropic Broadband E-Field Probe, Béla Szentpáli, István Réti, Ferenc B. Molnár, János Farkasvölgyi,
Károly Kazi, Zoltán Mirk, Aurél Sonkoly, and Zoltán Horváth
Volume 2008, Article ID 816969, 4 pages

Ka Band Phase Locked Loop Oscillator Dielectric Resonator Oscillator for Satellite EHF Band Receiver, S. Coco, F. Di Maggio, A. Laudani, and I. Pomona
Volume 2008, Article ID 632549, 6 pages

The Novel Microwave Stop-Band Filter, R. E. Chernobrovkin, I. V. Ivanchenko, A. M. Korolev,
N. A. Popenko, and K. Yu. Sirenko
Volume 2008, Article ID 745368, 5 pages

Passive Frequency Selective Surface Array as a Diffuser for Destroying Millimeter Wave Coherence,
Saiful Islam, Johan Stiens, Gert Poesen, Irina Jaeger, and Roger Vounckx
Volume 2008, Article ID 391745, 6 pages

A New Fractal-Based Design of Stacked Integrated Transformers, Goran Stojanović,
Milan Radovanović, and Vasa Radonić
Volume 2008, Article ID 134805, 8 pages

High Efficiency and Broadband Microstrip Leaky-Wave Antenna, Onofrio Losito
Volume 2008, Article ID 742050, 6 pages

Material Parameter Measurements for Microwave Antireflection Coating Development, Lajos Nagy
Volume 2008, Article ID 247958, 6 pages

Prospects of 4H-SiC Double Drift Region IMPATT Device as a Photo-Sensitive High-Power Source at 0.7 Terahertz Frequency Regime, Moumita Mukherjee, Nilratan Mazumder, and Sitesh Kumar Roy
Volume 2008, Article ID 275357, 9 pages

Modeling and Measurements of Novel Monolithic Filters, Aly H. Aly, Badawy El-Sharawy,
and Adalbert Beyer
Volume 2008, Article ID 537069, 8 pages

Editorial

Active and Passive Microwave Devices and Circuits

T. S. Kalkur,¹ Tibor Berceli,² and Fahrettin Yakuphanoglu³

¹ *Department of Electrical and Computer Engineering, University of Colorado, Colorado Springs, CO 80933, USA*

² *Broadband Infocommunications and Electromagnetics Department, Budapest University of Technology and Economics, Goldmann Gyorgy ter 3, 1111 Budapest, Hungary*

³ *Physics Department, Faculty of Arts and Sciences, Firat University, 23119, Elazig, Turkey*

Correspondence should be addressed to T. S. Kalkur, kalkur@eas.uccs.edu

Received 18 August 2008; Accepted 18 August 2008

Copyright © 2008 T. S. Kalkur et al. This is an open access article distributed under the Creative Commons Attribution License, which permits unrestricted use, distribution, and reproduction in any medium, provided the original work is properly cited.

New systems working at RF, microwave, and millimeter wave will give rise to new services for medical, security, home, entertain, and communication industries. Active and Passive Microwave Devices and Circuits are playing an important role in the design of these systems. This special issue of Active and Passive components is devoted towards the design, analysis, and fabrication of Active and Passive components.

In the first paper entitled “Dependence on frequency of the electromagnetic field distribution inside a cylindrical cavity,” the authors explain the relevant changes in the electron cyclotron resonance ion source behavior for small variations of the exciting radiation frequency.

The second paper in this issue “Printed antenna arrays with side lobe suppression” investigates approaches and their limitations to minimize side lobes in printed antenna arrays. It also proposes antenna structures with printed pentagonal dipole arrays.

The third paper “Isotropic broad-band E-field probe” discusses the development and characterization of isotropic broad-band E-field probe which has an isotropic reception from 100 MHz to 18 GHz.

In satellite communication networks, the noise performance and the required spectral purity of the low noise band receiver are of the important issues.

The fourth paper “Ka band phase locked loop oscillator for satellite EHF band receiver” deals with the design and fabrication of Ka band phase locked loop oscillator (PLL DRO) with a fundamental frequency 19.250 GHz for satellite EHF band receiver.

The fifth paper “The novel microwave stop-band filter” proposes new band rejection element for implementing stop band filter. This paper also describes the synthesis,

manufacture and testing of fifth-order Chebyshev filters implemented with this band rejection element.

The sixth paper “Passive frequency selective surface array as a diffuser for destroying millimeter wave coherence” proposes the design, construction, and testing of grounded frequency selective surfaces (FSS) as a diffuser for destroying millimeter wave coherence which is used to eliminate speckle in active millimeter wave imaging. The FSS arrays were designed with finite integral technique and fabricated by etching technique. The S-parameter was characterized with a free space MVNA and measurement of radiation patterns was done with a BWO in motorized setup.

In the seventh paper entitled “A new fractal-based design of stacked integrated transformers,” novel fractal stacked transformers were analyzed using full-wave EM simulations and compared in terms of the inductance and quality factor. The novel fractal stacked transformers show improved performance over conventional spiral inductor-based transformers.

A novel layout of leaky-wave antennas based on tapered design has been proposed and investigated in the eighth paper “High efficiency and broadband microstrip leaky-wave antenna.” This paper also shows that this structure is attractive for the design of high performance microstrip leaky-wave antennas for microwave and millimeter wave applications.

The ninth paper entitled “Material parameter measurements for microwave antireflection coating development” is on the material parameter measurements for microwave antireflection coating development.

Prospects of 4H-SiC double drift region IMPATT device as a photo-sensitive high-power source at 0.7 terahertz frequency regime is presented in the tenth paper entitled

“Prospects of 4H-SiC double drift IMPATT device as a photo-sensitive high power source at 0.7 terahertz frequency regime.”

The last paper entitled “Modeling and measurements of novel monolithic filters” presents novel miniaturized multilayer tunable high Q-filters based on hair pin resonators including ferroelectric materials and it is suitable for chip and package integration and narrow band applications.

ACKNOWLEDGMENTS

The editors are pleased to submit this special issue to Hindawi Publishing Corporation and hope that this issue accomplishes their goal of highlighting outstanding advances in the active and passive microwave devices and circuits. Thanks are expressed to all the reviewers who have read the abstracts and articles. Their contribution has been most valuable.

*T. S. Kalkur
Tibor Berceci
Fahrettin Yakuphanoglu*

Research Article

Dependence on Frequency of the Electromagnetic Field Distribution inside a Cylindrical Cavity Excited through an Off-Axis Aperture

Fabrizio Consoli,¹ Luigi Celona,¹ Giovanni Ciavola,¹ Santo Gammino,¹ Fabio Maimone,¹ Rocco Salvatore Catalano,² Sebastiano Barbarino,^{2,3} David Mascali,³ and Livia Tumino²

¹Laboratori Nazionali del Sud, Istituto Nazionale di Fisica Nucleare, Via S. Sofia 62, 95123 Catania, Italy

²Dipartimento di Fisica e Astronomia, Università degli Studi di Catania, Via S. Sofia 64, 95123 Catania, Italy

³Dipartimento di Ingegneria Informatica e delle Telecomunicazioni, Università degli Studi di Catania, Viale A. Doria 6, 95125 Catania, Italy

Correspondence should be addressed to Fabrizio Consoli, consoli@lns.infn.it

Received 18 November 2007; Accepted 18 March 2008

Recommended by Tibor Bercei

To explain the relevant changes in the electron cyclotron resonance ion source behaviour for small variations of the exciting radiation frequency, we determine the spatial distribution of the field within the cavity for every resonant mode.

Copyright © 2008 Fabrizio Consoli et al. This is an open access article distributed under the Creative Commons Attribution License, which permits unrestricted use, distribution, and reproduction in any medium, provided the original work is properly cited.

1. INTRODUCTION

In we want to study the electromagnetic field distribution in a perfectly conductive cylindrical cavity, for every resonant mode excited by a rectangular waveguide operating in the microwave range, through an aperture placed off axis on the top circular base (see Figure 1).

This situation is actually met in the modern electron cyclotron resonance (ECR) ion sources, where plasma is magnetically confined and excited by microwave fields. It was experimentally observed [1] that the plasma formation, the consequent amount of particles extracted from the source, and the related beam shape strongly depend on the frequency of the electromagnetic wave feeding the cavity. Indeed, by considering an ideal cavity, the frequency variation of the incoming radiation causes the excitation of a discrete number of modes (see Figure 1(b)), each coupled differently with the off-axis waveguide. Then, the electromagnetic field distribution inside the cavity will be different for each resonant frequency. Therefore, the particle motion will be affected by the selected mode, that is, by the excitation frequency. On the purpose to give a quantitative explanation of the problem we propose, in the preliminary phase of this

work, to give the description of the electromagnetic field within the cavity following Van Bladel's approach [2]. We consider as a reference for this study the experimental setup represented by the SERSE ion source operating at INFN-LNS in Catania since 1998 [3, 4], but the analysis described in the following is applicable to any similar apparatus.

2. DESCRIPTION OF THE EXPERIMENTAL SETUP

The particles inside the ion source cavity are subjected to a nonuniform confining magnetostatic field \vec{B} . It is possible to consider it as generated by the superimposition of a hexapole and two solenoids:

$$\begin{aligned} B_x &= x(-B_1z + 2S_{\text{ex}}y), \\ B_y &= -B_1yz + S_{\text{ex}}(x^2 - y^2), \\ B_z &= B_0 + B_1z^2, \end{aligned} \quad (1)$$

where S_{ex} is a constant related to the hexapole field, B_0 and B_1 to the solenoids ones. For the sake of simplicity, we consider

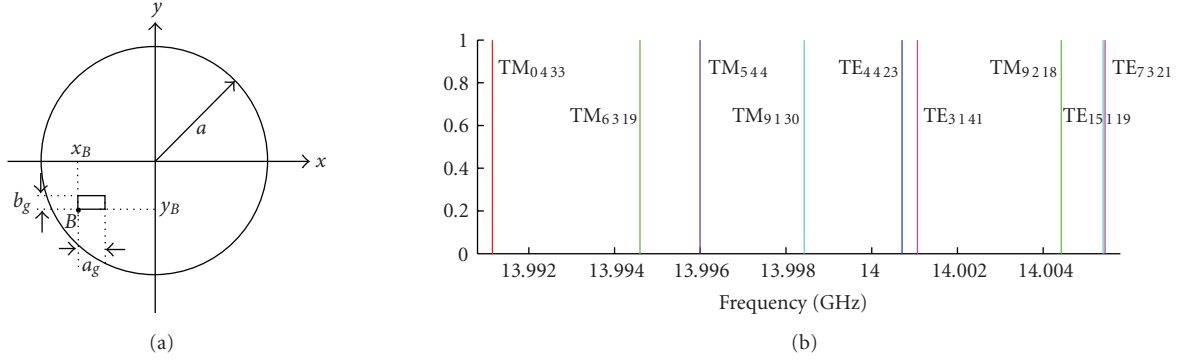


FIGURE 1: Scheme of the top base of the cylindrical cavity with the feeding waveguide, $a = 6.5$ cm, L (cavity length) = 45 cm, $a_g = 2b_g = 15.8$ mm, $x_B = -40.4$ mm, $y_B = -28.95$ mm. (b) Mode distribution near to 14 GHz, usual source excitation frequency.

here the presence of only one electron inside the cavity. The equation describing its motion in a magnetostatic field is

$$\frac{d\vec{v}}{dt} = \frac{q}{m_0\gamma(v)} [\vec{v} \times \vec{B}], \quad (2)$$

where \vec{v} , q , and m_0 are the velocity, the charge, and the rest mass of the electron, $\gamma(v) = [1 - (v/c)^2]^{-0.5}$ is the relativistic factor, c is the light velocity in vacuum, and $\vec{B} = B_x\hat{x} + B_y\hat{y} + B_z\hat{z}$ is given by the formulas (1). The particle trajectory achieved by the numerical solution of this differential equation with given initial conditions has a projection in the xy plane for $z = L/2$, like that star shape represented in all the pictures of Figure 2. By considering the different patterns achieved by varying these initial conditions, it was possible to observe that the motion shape and the directions of the trajectories tips are quite similar one to the others because they are determined by the magnetostatic field only.

3. DISTRIBUTION OF THE ELECTROMAGNETIC FIELD WITHIN THE CAVITY

In Figure 1(a), the scheme of the cylindrical cavity is shown with its feeding WR62 rectangular waveguide placed far from the cavity axis. The fields in stationary conditions, inside a lossless cavity in vacuum can be written as [2]

$$\begin{aligned} \vec{E} &= -\sum_m \left[c \frac{\omega_m}{\omega_m^2 - \omega^2} \frac{\int_S (\hat{z} \times \vec{E}_{TE10}) \cdot \vec{h}_m dS}{\int_V |\vec{e}_m|^2 dV} \right] \vec{e}_m, \\ \vec{H} &= -\frac{1}{i\omega\mu} \sum_m \left[\frac{\int_S (\hat{z} \times \vec{E}_{TE10}) \cdot \vec{g}_m dS}{\int_V |\vec{g}_m|^2 dV} \right] \vec{g}_m \\ &\quad + \sum_m \left[\frac{1}{i\mu} \frac{\omega}{\omega_m^2 - \omega^2} \frac{\int_S (\hat{z} \times \vec{E}_{TE10}) \cdot \vec{h}_m dS}{\int_V |\vec{h}_m|^2 dV} \right] \vec{h}_m, \end{aligned} \quad (3)$$

where the index m stands for a triple set of indices, $\mu = 4\pi \cdot 10^{-7}$ H/m, $c = 299792458$ m/s, S is the excitation aperture

surface, V is the cavity volume, ω and ω_m are the excitation and the mode characteristic angular frequencies, \vec{h}_m and \vec{e}_m are the solenoidal magnetic and electric eigenvectors (with $\vec{h}_m = (c/\omega_m)\vec{\nabla} \times \vec{e}_m$), \vec{g}_m is the irrotational magnetic eigenvector, and

$$\vec{E}_{TE10} = -Aie^{i\omega t} \frac{\omega\mu a_g}{\pi} \sin\left(\frac{\pi x}{a_g}\right) \hat{y} \quad (4)$$

is the field of the dominant mode in the rectangular waveguide. We indicate with a_g the waveguide width (see Figure 1), and A is a constant related to the waveguide power. If the frequency of the incoming wave does not coincide with one of the ω_m in (3), the field in the ideal lossless cavity is the sum of different finite terms, contributing to the total energy in the cavity. If, otherwise, for a given \bar{m} the frequency ω coincides exactly with $\omega_{\bar{m}}$, the term in (3) relative to this mode will diverge, that is, it will become much larger than the others. In the time domain, it means that the energy in the cavity constantly increases with time and with a rate depending on the coupling between the incoming wave and the mode \bar{m} [5]. An accurate general representation of the fields at the resonance can be therefore obtained by considering only the coefficient of the diverging term. The general expression of the electric field can be written as

$$\begin{aligned} \vec{E}_{TM} &= ie^{i\omega t} A \frac{c^2\mu a_g \omega}{L^2\pi a} \\ &\quad \times \sum_{n,r} \frac{1}{1 - (\omega/\omega_{nr})^2} \frac{\epsilon_n}{\omega_{nr}^2 x_{nr} J_{n+1}^2(x_{nr})} \left\{ \begin{array}{l} \text{Re}\{I_{nr}^{TM}\} \\ \text{Im}\{I_{nr}^{TM}\} \end{array} \right\} \\ &\quad \times \left[\frac{rx_{nr}}{a} J_n\left(\frac{x_{nr}\rho}{a}\right) \sin\left(\frac{r\pi z}{L}\right) \left\{ \begin{array}{l} \sin n\phi \\ \cos n\phi \end{array} \right\} \hat{e}_\rho \right. \\ &\quad \left. + \frac{rn}{\rho} J_n\left(\frac{x_{nr}\rho}{a}\right) \sin\left(\frac{r\pi z}{L}\right) \left\{ \begin{array}{l} \cos n\phi \\ -\sin n\phi \end{array} \right\} \hat{e}_\phi \right. \\ &\quad \left. - \frac{Lx_{nr}^2}{\pi a^2} J_n\left(\frac{x_{nr}\rho}{a}\right) \cos\left(\frac{r\pi z}{L}\right) \left\{ \begin{array}{l} \sin n\phi \\ \cos n\phi \end{array} \right\} \hat{e}_z \right], \end{aligned} \quad (5)$$

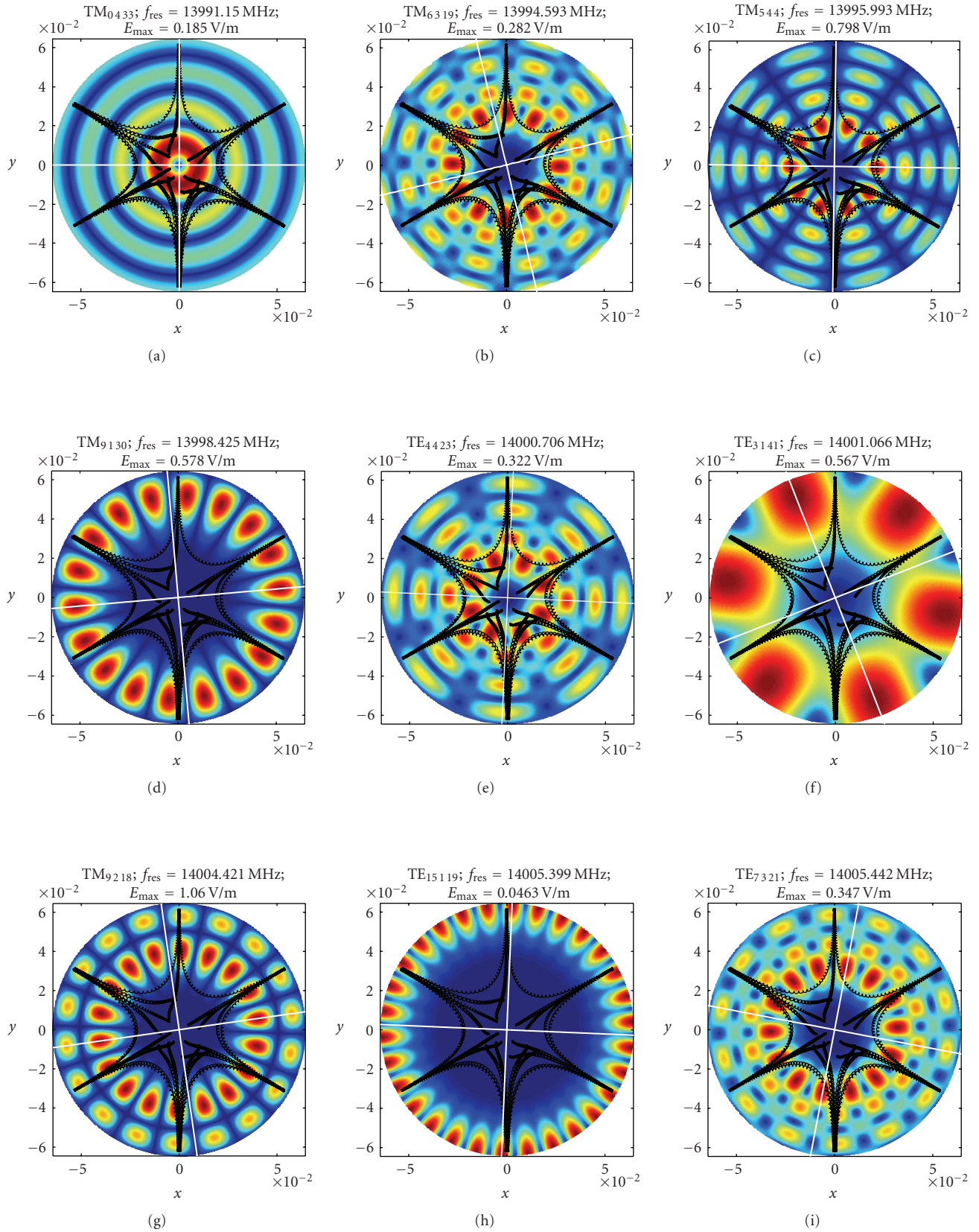


FIGURE 2: Modulus of the electric field without the term $\{1/[1 - ((\omega/\omega_{nr})^2)]\}$ in the plane $z = L/2$ for modes close to the 14 GHz frequency for 1 W of the incoming wave power. For each mode the maximum field value is estimated after an equal time interval, supposed large enough to neglect the second-order terms. The white normal axes indicate the mode rotation caused by the coupling with the rectangular waveguide.

for the TM modes, with ε_n the Neumann's factor (equal to 1 for $n = 0$, equal to 2 if $n = 1, 2, \dots$), $x_{n\nu}$ the ν -root of the Bessel function of n order, and

$$I_{n\nu}^{\text{TM}} = - \int_S \sin \left[\frac{\pi(x - x_A)}{a_g} \right] \left[e^{-i(n+1)\phi} J_{n+1} \left(\frac{x_{n\nu} \rho}{a} \right) + e^{-i(n-1)\phi} J_{n-1} \left(\frac{x_{n\nu} \rho}{a} \right) \right] dS, \quad (6)$$

and for the TE modes

$$\begin{aligned} \vec{E}_{\text{TE}} &= ie^{i\omega t} A \frac{c^2 \mu a_g \omega}{L^2 \pi a} \\ &\times \sum_{n,\nu,r} \frac{1}{1 - (\omega/\omega_{n\nu r})^2} \frac{\varepsilon_n r x'_{n\nu}}{\omega_{n\nu r}^2 (x'_{n\nu})^2 - n^2} J_n^2(x'_{n\nu}) \\ &\times \left\{ \begin{array}{l} \text{Im} \{ I_{n\nu}^{\text{TE}} \} \\ \text{Re} \{ I_{n\nu}^{\text{TE}} \} \end{array} \right\} \sin \left(\frac{r\pi z}{L} \right) \\ &\cdot \left[\frac{n}{\rho} J_n \left(\frac{x'_{n\nu} \rho}{a} \right) \begin{Bmatrix} \cos n\phi \\ -\sin n\phi \end{Bmatrix} \hat{e}_\rho \right. \\ &\quad \left. - \frac{x'_{n\nu}}{a} J_n' \left(\frac{x'_{n\nu} \rho}{a} \right) \begin{Bmatrix} \sin n\phi \\ \cos n\phi \end{Bmatrix} \hat{e}_\phi \right], \end{aligned} \quad (7)$$

with $x'_{n\nu}$ the ν -root of the first derivative of the Bessel function of n order and

$$I_{n\nu}^{\text{TE}} = \int_S \sin \left[\frac{\pi(x - x_A)}{a_g} \right] \left[- e^{i(n+1)\phi} J_{n+1} \left(\frac{x'_{n\nu} \rho}{a} \right) + e^{i(n-1)\phi} J_{n-1} \left(\frac{x'_{n\nu} \rho}{a} \right) \right] dS. \quad (8)$$

The integrals (6) and (8) represent the coupling for the TM and TE cases, giving a different amount of energy to be transferred from the incoming electromagnetic wave to each mode. In Figure 2, the modulus of the electric field without the term $1/(1 - (\omega/\omega_{n\nu r})^2)$ is shown in the xy plane for $z = L/2$, for the modes with resonance between 13991.15 MHz and 14005.44 MHz. For each of them, the geometric degeneration is uniquely resolved by the exciting waveguide, and the related rotation is indicated by two normal white axes. The maximum modulus has been calculated for 1 W of the waveguide power, and after a time interval large enough to neglect the second-order terms. It can be an estimation of the actual energy coupled to each mode.

4. CONCLUSION

It has been shown that the field distribution inside the cavity of an electron cyclotron resonance ion source can be changed significantly by means of small frequency variations that have a huge effect both on the spatial distribution of minima and maxima and on the amount of energy coupled from the

feeding waveguide to the cavity. The modes have a completely different pattern. Preliminary calculations, not shown here, indicated that some electromagnetic field configurations are more effective to accelerate the confined electrons, because of their proper spatial intensity distribution respect to the star shaped trajectory, representative of the particle motion in presence of the magnetostatic field only. It has a direct effect on the rate of ionisation and therefore on the plasma formation.

REFERENCES

- [1] S. Gammino, "3rd and 4th generation ECRIS: some possible scenarios," in *Proceedings of the 17th International Workshop on ECR Ion Sources and Their Applications*, IMP, Lanzhou, China, September 2006.
- [2] J. Van Bladel, *Electromagnetic Fields*, Springer, Berlin, Germany, 1985.
- [3] S. Gammino and G. Ciavola, "The contribution of the INFN-LNS to the development of electron cyclotron resonance ion sources," *Review of Scientific Instruments*, vol. 71, no. 2, pp. 631–636, 2000.
- [4] F. Consoli, S. Barbarino, L. Celona, G. Ciavola, S. Gammino, and D. Mascali, "Investigation about the modes in the cylindrical cavity of an ECR ion source," *Radiation Effects and Defects in Solids*, vol. 160, no. 10–12, pp. 467–475, 2005.
- [5] J. C. Slater, *Microwave Electronics*, Van Nostrand, London, UK, 1963.

Research Article

Printed Antenna Arrays with High Side Lobe Suppression

Aleksandar Nešić, Ivana Radnović, and Zoran Mičić

IMTEL Institute, Bulevar Mihajla Pupina 165b, 11070 Novi Beograd, Serbia

Correspondence should be addressed to Ivana Radnović, ivana@insimtel.com

Received 27 November 2007; Accepted 18 March 2008

Recommended by Tibor Berceci

The problem of side lobe suppression (SLS) in printed antenna arrays has been investigated in the paper. Influence of several factors that make difficult design and realization of antenna arrays with relatively high SLS has been analyzed. We introduced a new type of printed antenna array with symmetrical pentagonal dipoles and symmetrical tapered feed network with Chebyshev distribution enabling SLS better than 34 dB in E-plane. Agreement between simulated and measured results is very good. The antenna is suitable for integration with other microwave circuits. Presented antenna is low cost and very simple for realization.

Copyright © 2008 Aleksandar Nešić et al. This is an open access article distributed under the Creative Commons Attribution License, which permits unrestricted use, distribution, and reproduction in any medium, provided the original work is properly cited.

1. INTRODUCTION

Microwave antenna arrays are usually used in telecommunication systems such as indoor and outdoor wireless LANs, point to point and point to multipoint and also in radar microwave and millimeter systems. One of the main antenna characteristics is SLS in radiation patterns which is defined for telecommunication systems (usually for microwave links) by international standards and recommendations [1]. In conventional radar systems, requirements for SLS are much severe since responses from side lobes practically are false targets. Depending on the antenna class, required SLS in telecommunications systems is about 20 to 40 dB. For example, in AWACS and F-16 radar systems, this suppression is better than 50 dB.

Such impressive SLSs are hardly achievable with conventional microstrip antenna arrays (with patches). In microstrip antenna arrays presented in literature, side lobe levels are suppressed 25 dB (related to main lobe) at best. A relatively small number of publications dealing with this issue are available [2–4].

2. LIMITING FACTORS IN REALIZATION OF PRINTED ANTENNA ARRAYS WITH HIGH SIDE LOBE SUPPRESSION

There are several problems in realization of printed antenna arrays with relatively high SLS. The main of them are tolerances in fabrication, mutual coupling between radiating ele-

ments, limitations in feasibility of feed network realization, and surface wave effect as well as parasitic radiation from a feeding network.

Due to effects mentioned above, it is quite difficult to obtain sidelobe suppression better than 25 dB in microstrip antenna arrays [2]. Tolerances affect various parameters on which sidelobe suppression depends are as follows: (1) dimensions of radiating element, (2) dimensions of feeding lines (width and length) including branches that represent impedance transformers, and (3) distance between radiating elements.

(1) and (2) influence tolerances of phase and amplitude of radiating elements on which SLS depends directly. As it is known, microstrip patches have relatively narrow bandwidth, that is, quick change of impedance with its dimensions change. The consequence of this is notable phase as well as amplitude deviation from optimized values. Another factor is tolerance of feed network dimensions (microstrip lines and impedance transformers) on which amplitude and phase deviations depend directly.

Another group of factors that affect side lobe suppression includes (4) surface wave effect, (5) parasitic radiation from a feed network, especially when the feed network is printed on the same dielectric substrate as the antenna elements, and (6) mutual coupling between radiating elements. However, mutual coupling effect can be easily incorporated into design of the feed network. The above factors are the most noticeable in conventional microstrip antenna arrays with patches as radiating elements that are printed on a dielectric

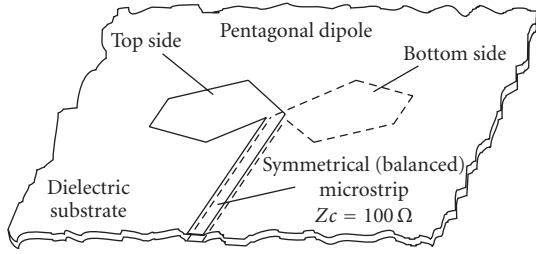


FIGURE 1: Pentagonal dipole as a basic element of the antenna array printed on dielectric substrate.

substrate and are fed by conventional (unbalanced) microstrip lines.

3. SIDE LOBE SUPPRESSION

In order to decrease side lobe levels, various tapered distributions are used in antenna arrays: cosine, cosine-squared, Gaussian, Taylor, and Chebyshev. These distributions are being chosen depending on required side lobe attenuation, possible pedestal in distribution (I_{\max}/I_{\min} ratio), desired position of radiating elements, desired position, that is, distribution of side lobes, distance between radiating elements, number of radiating elements, and expected tolerances in realization.

Pozar and Kaufman in [2] show that variation in frequency of 1% causes, in patch antenna arrays, the phase change of 12.5° which dramatically decreases SLS from 40 dB (in ideal case) to 26 dB. Only due to parasitic radiation from a microstrip feeding line, SLS decreases from 40 dB to about 30 dB. Other parasitic factors that degrade side lobe suppression in patch antenna arrays such as surface wave effect and diffraction are also significantly influenceable, so one cannot expect SLS better than 25 dB. The exception is case when each radiating element is fed through a separate tunable phase shifter and attenuator and when the feed network is not on the same dielectric substrate with elements [2].

Beside conventional printed antenna arrays with patches fed by conventional asymmetrical microstrip line, there are printed antenna arrays with printed dipoles, usually of pentagonal shape (one half of them on one side and another half on the opposite side of the substrate). These dipoles operate on the second resonance and are fed by a symmetrical (balanced) microstrip line, Figure 1, [5].

Behind the array, there is a reflector plate [6] or the linear array is placed between two plates which form a corner reflector [5]. Figure 2 shows real and imaginary parts of pentagonal dipole impedance versus frequency, printed on dielectric substrate of 0.254 mm thickness and $\epsilon_r = 2.1$. It is obvious that impedance variation with frequency is very slow which is of crucial importance for arrays with high SLS. Also, due to the fact that feed network is symmetrical and consists of symmetrical microstrip lines, parasitic radiation from it is practically eliminated. Majority of factors that make difficult realization of printed antenna arrays with high side lobe suppression has been eliminated in these printed arrays.

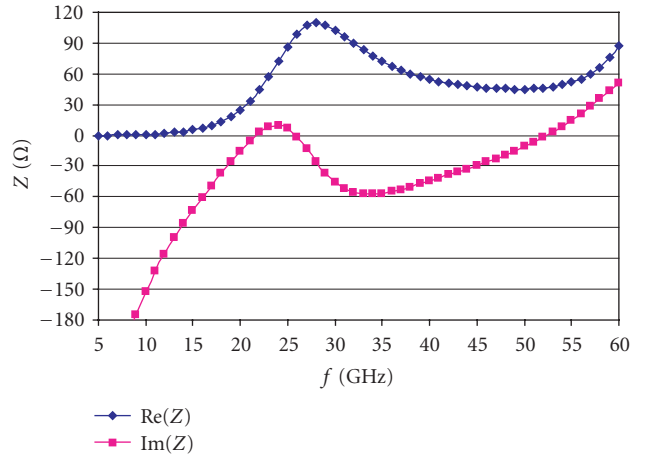


FIGURE 2: Real and imaginary part of pentagonal dipole impedance versus frequency ($\epsilon_r = 2.1$, $h = 0.254$ mm, and $S = \lambda_0/4$) when aperture angle (α) is 180° .

Because of tolerances in photolithographic process as well as dilatations caused by temperature change, deviations from projected values of position, amplitude, and phase of radiating elements in the array occur. We will investigate influence of these tolerances in the case of printed antenna array with 8 broadband pentagonal dipoles operating on second resonance and with mutual distance of $0.85\lambda_0$. Dipoles are fed by feed network enabling Dolph-Chebyshev distribution of the second order with pedestal (I_{\max}/I_{\min}) of 17 dB.

Realizable values of relative tolerances have been assumed at operating frequency of 26 GHz:

- (i) *deviations in distances between radiating elements in the array:* 1% or 2% of λ_0 ,
- (ii) *amplitude deviations along tapered lines:* 1 dB or 2 dB,
- (iii) *phase deviations:* 2° or 4° (corresponds to about $40 \mu\text{m}$ and $80 \mu\text{m}$ tolerances in length of the feeding line).

Using [7], SLS has been calculated: (a) in ideal case; (b) in case of higher deviation only in position of radiating elements; (c) in case of greater amplitude errors only; (d) in case of greater phase errors only; (e) in real cases when all minor errors exist; and (f) when all existing errors are of greater value. Results are presented in Table 1. Errors were randomly distributed in the simulation process (Monte Carlo method).

Figures 3(a), 3(b), 3(c), 3(d), 3(e), and 3(f) show simulated radiation patterns for the cases given in the table above.

For the purpose of better insight in the assumed values resulting from tolerances in realization, we give the absolute values of assumed errors at 26 GHz: tolerances in radiating elements positioning are $230 \mu\text{m}$ Figures 3(b), 3(f); phase errors result from tolerances in feed lines' lengths that are $40 \mu\text{m}$ Figure 3(e) and $80 \mu\text{m}$ Figures 3(d), 3(f). Amplitude

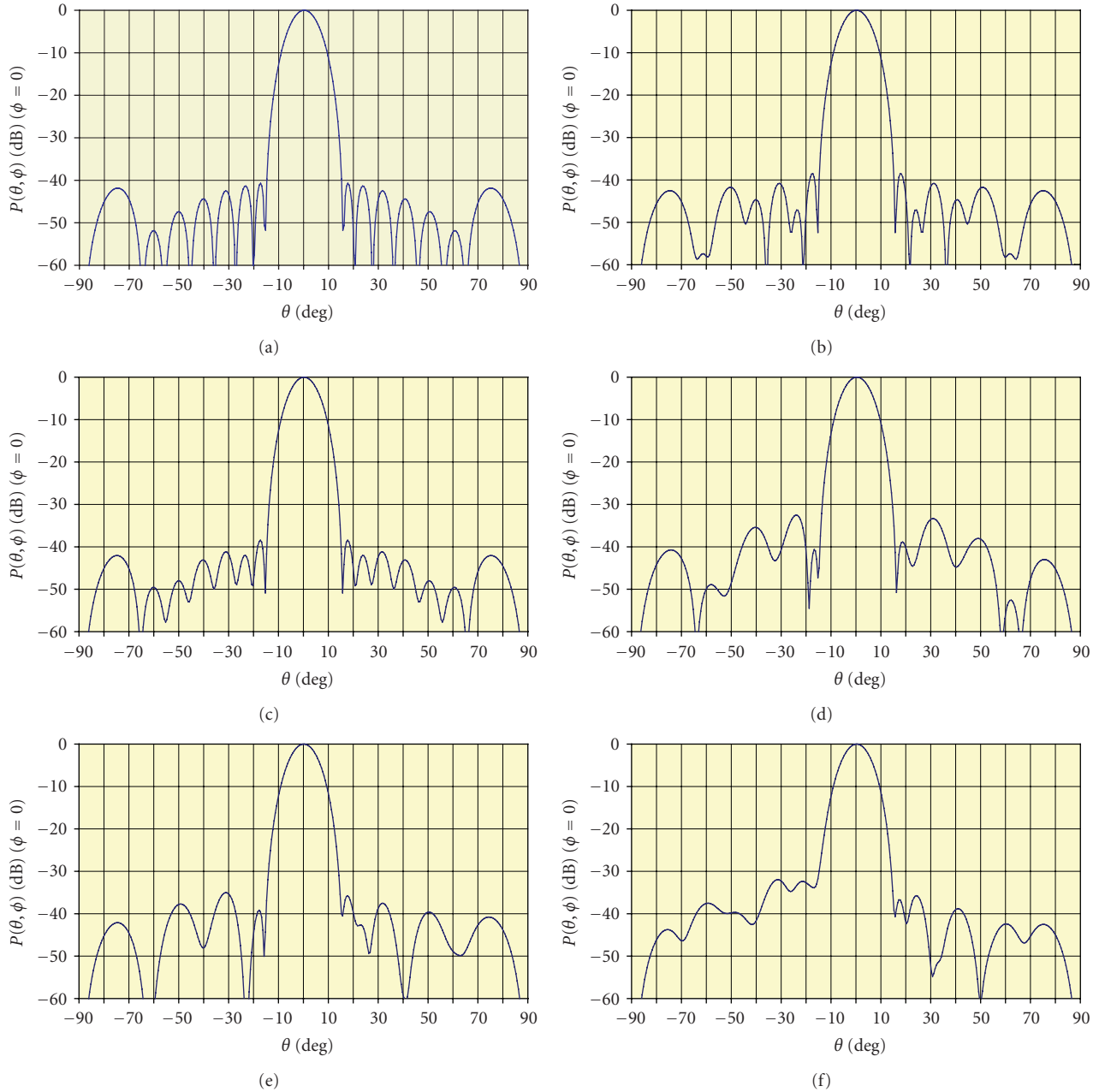


FIGURE 3: (a), (b), (c), (d), (e), and (f) Simulated radiation patterns for several cases of deviations (amplitude, phase, and radiating elements positioning deviations).

errors occur as a consequence of tolerances in impedance transformer lines widths.

4. CONCEPT, DESIGN, AND REALIZATION OF PRINTED TAPERED LINEAR ANTENNA ARRAY WITH CORNER REFLECTOR

Proposed antenna array consist of three parts: (1) axial array of eight printed pentagonal dipoles (Figure 4, Detail B) (2) feeding network printed on the same dielectric substrate with the pentagonal dipoles (Figure 4, Detail A) and (3) corner reflector consisting of two metal plates. Distance between

the dipoles (at the center frequency) is chosen in such a way to obtain relatively high-array gain with sufficient SLS in tapered array. In our case, the distance between axial dipoles is $0.85\lambda_0$. Also, with such distance between axial dipoles, mutual coupling is very low making the design and optimization of the antenna array relatively easy. Pentagonal dipoles' dimensions were optimized with program package WIPL-D [8] so to obtain impedance of $100\ \Omega$ at the center frequency of 26 GHz. During the optimization the influence of symmetrical microstrip feeding line of $Z_c = 100\ \Omega$ was taken into account. In this case, we have adjusted dimensions of pentagonal dipoles in printed array to obtain impedance

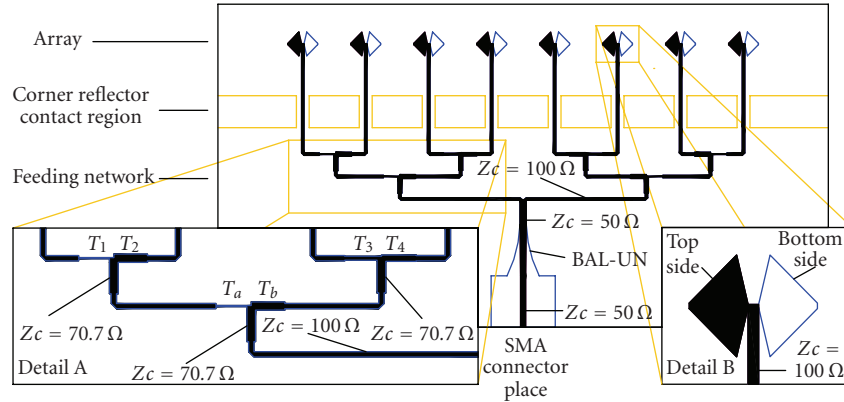


FIGURE 4: Printed antenna array and tapered feeding network integrated on the same dielectric substrate ($\epsilon_r = 2.1$, $h = 0.254$ mm, and $\text{tg}\delta = 4 \times 10^{-4}$). Detail A: tapered feeding network. Detail B: Pentagonal dipole with a symmetric microstrip feeding line of $Z_c = 100 \Omega$.



FIGURE 5: Realized antenna array with corner reflector compared to US quarter.

of 100Ω at the center frequency of 26 GHz, taking into consideration the reflector influence. Since the dipoles are electrically symmetrical elements, the feeding network with tapering is realized with symmetrical (balanced) microstrip lines.

By using LINPLAN program package [7], we calculated distribution coefficients that could be achieved with a printed feeding network. Dolph-Chebyshev distribution of the second order with I_{\max}/I_{\min} of 17 dB has been chosen. Distances between dipoles are $0.85\lambda_0$. Under these conditions, we have obtained distribution coefficients enabling highest SLS of 40.72 dB (@ $\Theta = \pm 18^\circ$). In order to attain desired distribution, we designed feeding network in symmetrical microstrip technique with $\lambda/4$ transformers, T_{1-4} and $T_{a,b}$ (Figure 4, Detail A). With obtained structure, we carried out full-wave analysis [9] in the frequency range

from 24 GHz to 28 GHz. Corrections of phase deviations were accomplished by changing the lengths of particular branches in the feeding network, while amplitude deviations remained uncorrected. After these corrections, we achieved symphase feeding of all dipoles in the array.

Corner reflector is designed using the results from [10], which contains very detailed experimental results obtained by variation of length (L), width (W), aperture angle between corner reflector plates (α), and distance of radiating element from apex (S). Suitable radiation pattern with relatively high gain and high SLS in H-plane is obtained with $L = W = 4\lambda_0$, $\alpha = 45^\circ$, and $S = 0.7\lambda_0$.

Axial array with feeding network and BAL-UN [11] is placed between two metallic plates forming a corner reflector with $\alpha = 45^\circ$. Beamwidth in H-plane (azimuth) depends mainly on the angle between the metallic plates and length of the reflector plates (L), while SLS in E-plane depends only on the linear antenna array, Figure 5.

Feeding lines for dipoles penetrate the junction of two reflector plates. In the place of this junction, there are holes through which symmetrical microstrip lines of the feeding network pass. Influence of the metallic plate on the microstrip lines is minimized by selecting the sufficient holes' diameter (2 mm).

5. OBTAINED RESULTS AND COMMENTS

Simulated and measured results are presented in Table 2 and Figures 6–8. The discrepancy between simulated and measured SLS is due to tolerances in photolithography and mounting process because relatively small inaccuracies can significantly influence precise distribution. The return loss measured at SMA connector is presented in Figure 8. The measured gain of the antenna is about 1 dB smaller than the simulated because the feeding network, BAL-UN, and transition from microstrip to SMA connector were not taken into account. Photograph of the realized antenna array with tapered distribution and 45° corner reflector operating in 26 GHz range is shown in Figure 5.

TABLE 1

	Radiating elements positioning error	Amplitude error	Phase error	Side lobe suppression of the highest lobe [dB]
a	0	0	0	40.72
b	$0.02\lambda_0$	0	0	38.56
c	0	2 dB	0	38.87
d	0	0	4°	32.66
e	$0.01\lambda_0$	1 dB	2°	35.05
f	$0.02\lambda_0$	2 dB	4°	32.02

TABLE 2: Simulated and measured results at 26 GHz. G: gain; HSLSE, HSLSH: highest side lobe suppression (E-plane, H-plane); F/B: front to back ratio; HPBWE: E-plane 3 dB beamwidth, HPBWH: H-plane 3 dB beamwidth.

	G [dBi]	HSLSE [dB]	HSLSH [dB]	F/B [dB]	HPBWE [°]	HPBWH [°]
Simul.	21.4	38.4	35	32	10.5	23.8
Meas.	20.8	34.7	32.6	35.4	10.7	23.8

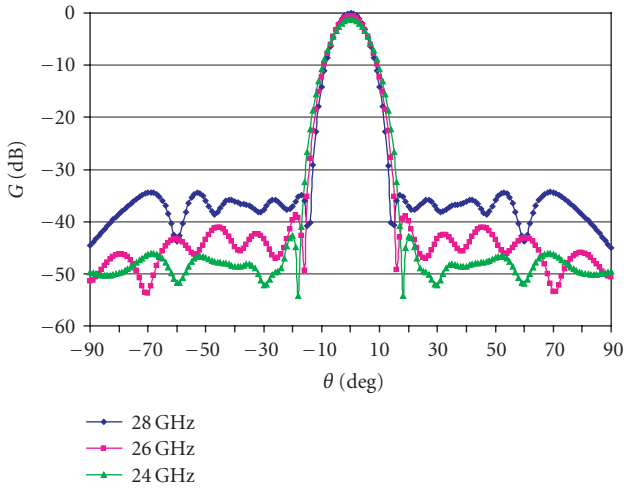


FIGURE 6: Normalized simulated E-plane radiation pattern at 24 GHz, 26 GHz, and 28 GHz.

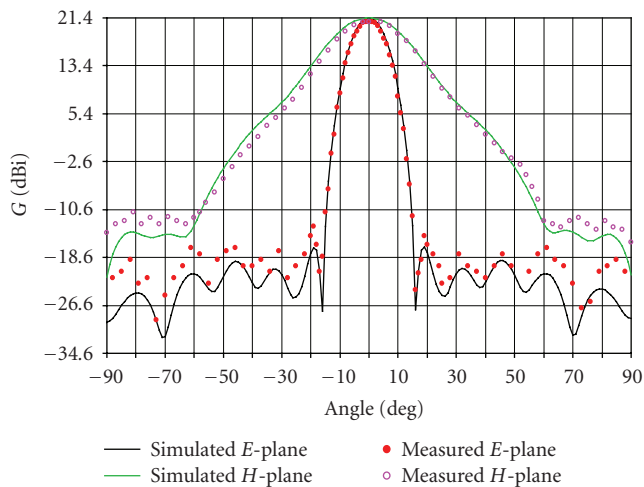


FIGURE 7: Simulated and measured radiation pattern in H- and E-plane at 26 GHz (highest side lobe is suppressed about 35 dB in relation to the main lobe).

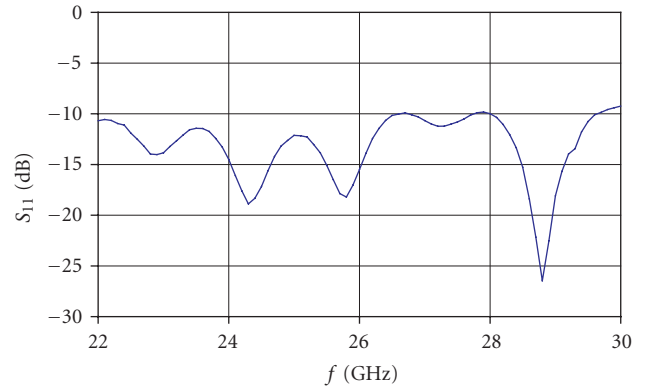


FIGURE 8: Measured return loss of the antenna array.

6. CONCLUSION

The paper investigates possibilities and limitations in printed arrays side lobe suppression. All relevant factors on which SLS depends are particularly analyzed: phase deviations, amplitude deviations, radiating elements positioning deviations, mutual coupling between elements, and parasitic radiation from the feed network. It is shown that SLS, satisfactory for most microwave telecommunication and especially radar systems, is hardly achievable with conventional microstrip antenna arrays with patches due to their narrow bandwidth that is, quick variation of impedance with dimensions change, parasitic radiation from the feed network, and surface wave effect.

Antenna structure with printed pentagonal dipoles forming the array is proposed. The dipoles operate on the second resonance and are fed by a symmetrical (balanced) microstrip line. Array consisting of 8 axially placed dipoles is fed through the feed network with impedance transformers enabling Chebyshev distribution with pedestal $I_{\max}/I_{\min} = 17$ dB. We have analyzed effects of particular parameters with assumed tolerances on which SLS depends. Linear antenna array realized in this way is placed between two metallic plates forming a corner reflector which enables

achieving relatively high SLS and narrow beamwidth even in H-plane. Measured beamwidth in E-plane at 26 GHz is 10.7° . Experimentally obtained E-plane SLS at 26 GHz, which depends only on the antenna array, is better than 34 dB and is, to the authors' knowledge, the best result published so far. The array is realized using standard photolithographic process with moderate precision of $\pm 10 \mu\text{m}$. Simulated and measured results are in very good accordance.

REFERENCES

- [1] IEEE Std 802.16c-2002, "IEEE standard for local and metropolitan area networks—part 16: air interface for fixed broadband wireless access systems—amendment 1: detailed system profiles for 10-66 GHz," December 2002.
- [2] D. M. Pozar and B. Kaufman, "Design considerations for low sidelobe microstrip arrays," *IEEE Transactions on Antennas and Propagation*, vol. 38, no. 8, pp. 1176–1185, 1990.
- [3] J. Hirokawa and M. Ando, "Sidelobe suppression in 76 GHz post-wall waveguide-fed parallel-plate slot arrays," *IEEE Transactions on Antennas and Propagation*, vol. 48, no. 11, pp. 1727–1732, 2000.
- [4] Y. Kimura, M. Takahashi, J. Hirokawa, M. Ando, and M. Haneishi, "76 GHz alternating-phase fed single-layer slotted waveguide arrays with suppressed sidelobes in the E-plane," in *Proceedings of the IEEE Antennas and Propagation Society International Symposium (APS '03)*, vol. 3, pp. 1042–1045, Columbus, Ohio, USA, June 2003.
- [5] A. Nešić, Z. Mičić, S. Jovanović, I. Radnović, and D. Nešić, "Millimeter wave corner reflector antenna array," in *Proceedings of the 35th European Microwave Conference (EUMC '05)*, vol. 3, pp. 1871–1874, Paris, France, October 2005.
- [6] A. C. Wilson and H. V. Cottony, "Radiation patterns of finite-size corner-reflector antennas," *IEEE Transactions on Antennas and Propagation*, vol. 8, no. 2, pp. 144–157, 1960.
- [7] M. Mikavica and A. Nešić, *CAD for Linear and Planar Antenna Arrays of Various Radiating Elements*, Artech House, Norwood, Mass, USA, 1992.
- [8] B. M. Kolundzija, J. S. Ognjanovic, and T. K. Sarkar, *Wipl: Electromagnetic Modeling of Composite Wire and Plate Structures: Software and User's Manual*, Artech House, Boston, Mass, USA, 1995.
- [9] "IE3D User's Manual," Zeland Software, Inc., Fremont, Calif, USA.
- [10] A. Nešić, I. Radnović, and V. Brankovic, "Ultrawideband printed antenna array for 60 GHz frequency range," in *Proceedings of the IEEE Antennas and Propagation Society International Symposium (APS '97)*, vol. 2, pp. 1272–1275, Montreal, Canada, July 1997.
- [11] A. Nešić and S. Dragas, "Frequency scanning printed array antenna," in *Proceedings of the IEEE Antennas and Propagation Society International Symposium (APS '95)*, vol. 2, pp. 950–953, Newport Beach, Calif, USA, June 1995.

Research Article

Isotropic Broadband E-Field Probe

Béla Szentpáli,¹ István Réti,¹ Ferenc B. Molnár,¹ János Farkasvölgyi,² Károly Kazi,² Zoltán Mirk,² Aurél Sonkoly,³ and Zoltán Horváth³

¹ *Research Institute for Technical Physics and Materials Science, P.O. Box 49, H-1525 Budapest, Hungary*

² *Bonn Hungary Electronics Ltd., P.O. Box 164, 1325 Budapest, Hungary*

³ *LINEARLAB Ltd., Budapest Fóti út 56, 1047 Budapest, Hungary*

Correspondence should be addressed to Béla Szentpáli, szentpali@mfa.kfki.hu

Received 30 November 2007; Accepted 11 March 2008

Recommended by T. Kalkur

An E-field probe has been developed for EMC immunity tests performed in closed space. The leads are flexible resistive transmission lines. Their influence on the field distribution is negligible. The probe has an isotropic reception from 100 MHz to 18 GHz; the sensitivity is in the 3 V/m–10 V/m range. The device is an accessory of the EMC test chamber. The readout of the field magnitude is carried out by personal computer, which fulfils also the required corrections of the raw data.

Copyright © 2008 Béla Szentpáli et al. This is an open access article distributed under the Creative Commons Attribution License, which permits unrestricted use, distribution, and reproduction in any medium, provided the original work is properly cited.

1. INTRODUCTION

The generation and measurement of defined electromagnetic fields for radiated immunity test on open-area test site are rather expensive and time-consuming. Further the environmental, meteorological conditions strongly influence the measurements. Therefore, there is a real need for performing the investigations in closed measuring chambers built in laboratory rooms. Different methods have been proposed in the literature as anechoic chambers, reverberation boxes or TEM cells [1, 2]. In all cases, there is a chance for the resonance in the chamber and/or the appearance of spurious modes and therefore the exposed electric field can differ from the expected one. The purpose of this work was the development of an E-field probe for the independent control of the actual value of the microwave field. There are field measuring devices in the trade; however, they are hardly suitable for building in the measuring chamber as a remote controlled accessory. Further, because they are intended to be used in free space or in large anechoic rooms, there is no special attention on the reflections from the equipment, which can disturb the distribution of the field in small chambers. In this paper, a device is described which overcomes these limitations; it can be mounted in the measuring chamber, and it has only minimal effect on the field distribution;

and the readout is performed outside the measuring chamber.

The device is made up of a field sensor and a 2m-long flexible cable delivering the signal to the connector on the wall of the chamber. It is important that the probe and its cable do not alter the field distribution in greater extent than 1 dB. The sensitivity of the probe should be isotropic because the test is made at all degrees of polarization. There is even a test method which applies rotating polarization [3]. Further the sensitivity should be high enough for measuring the field strength of 3 V/m, which is the lowest specified value by the IEC-ETSI in the frequency range of 30 MHz–18 GHz. We remind here that there are a great variety of prescribed field values in the different standards, starting from the mentioned lowest up to 200 V/m (MIL-STD-461E). The aim of this work was the development of a field probe for intensities from 3 V/m up to 10 V/m. The relative distribution of the electric field is determined by the testing arrangements; the magnitude of the electric field at each point in the measuring box is proportional to the square root of input power. This is why the limited sensitivity range of the probe does not affect significantly the application; the actual value of the field can be easily tuned in the range, where the measurement can be performed. However, the sensor should take even higher fields without degradation because it remains on the place during the test.

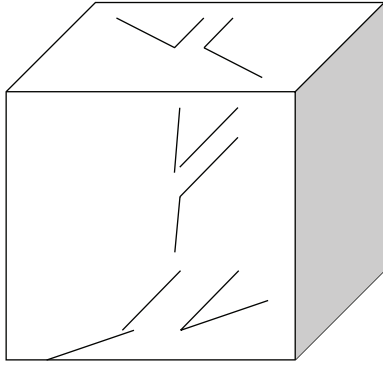


FIGURE 1: The draft of the sensing head.

2. THE CONSTRUCTION AND FEATURES

The traditional isotropic E-field probe construction, with three mutually orthogonal short dipole antenna was applied [4, 5] as it is shown in Figure 1. The sensing dipoles were fabricated by painting with silver paste through a mask. The three antennas were arranged along the faces of the cube fabricated from a styrofoam. The zero-bias detector diodes were mounted in the gap of the antennas also by silver paste. The connections between the sensors and the amplifier are 2-m-long flexible resistive transmission lines fabricated by screen printing from resistive carbon paste on 0.125 mm thick polyester foil [6, 7]. The 7mm-long dipoles are perpendicular to the resistive lines. Therefore, any field component parallel to the carbon wires results in only common-mode signal on the diode. The end of the resistive line is mounted in a DS type connector; it fits into the socket mounted on the inner wall of the measuring chamber. Facing to it on the outer wall of the chamber there is the equivalent socket into which the amplifier is connected.

The effect of the resistive transmission lines on the microwave field distribution was checked first in the GTEM cell [8]. A monopole antenna was fabricated from a semirigid cable by removing the outer conductor at the 12-mm-long end part. This antenna was fixed in the GTEM cell and the transmission was measured and saved between the feed point of the cell and this antenna in the case when the cell was empty. Then the resistive transmission line was placed into the GTEM cell and the transmission measurement was performed again. The difference of the first and the second transmission spectra was registered. The measurements were made by placing the sensing monopole in 5 measuring points within a $0.5 \times 0.5 \text{ m}^2$ square and orienting it to 3 mutually orthogonal directions in each measuring position (IEC 61000-4-20); Figure 2 shows one typical measurement.

The conclusion of the numerous investigations was that the difference in the transmission was always less than 1 dB in the case of the resistive lines, even when they were arranged in very different ways. On the other hand, any other conductive wires or coaxial cables resulted in significantly greater effects, at least at one frequency the difference exceeds the 6 dB. It happened also in the case of the thinnest available coaxial cable having only an outer diameter of

1.8 mm. Objects having dimensions much smaller than the wavelength as small metal boxes, or coaxial adapters, and so forth showed also small effect on the field, except when they were placed in the immediate vicinity of the monopole.

The resistive line is a lowpass filter as it is shown in Figure 3. The cut-off frequency is about 800 Hz. This is the reason for the application of the simple envelop detector only, having direct DC output. This is the price for the nondisturbing character of the probe.

At low levels, the output of the detectors are proportional to the square of the electric field. Therefore, the sum of the three signals will be the correct vectorial sum of the square of the total field strength, its square root is the effective value of the field, independent from the polarization. At higher levels, the output flattens down as the diode impedance lowers at higher biases. This effect was investigated by placing the detector in front of an antenna feed with variable powers. The situation is shown in Figure 4(a), where the detector output is depicted in the function of the power. In the saturation region, where the sensitivity of the detector decreases, the output signal will not proportion to the square of the field, therefore the sum of the three signals will not result the correct value of the total field. A possible normalization method is shown in Figure 4(b). It can be seen measured point pairs of the Figure 4(a) fit rather well to the exponential function, that is, the detector DC output power characteristic will be linear in log-log scale. This observation offers a method of normalization: the components of the E^2 can be determined from the logarithm of the DC signal. The other method is the regulation of the radiated power and keeping the detector always in the low-level range.

The sensitivity of the probe was calibrated in free space in an anechoic chamber with the help of calibrated antennas [9]. Figure 5 shows the normalized output voltage of one sensor at 10 V/m field strength. The normalization was done according to the second method: the power was regulated in such a way that the output was always lower than 25 mV. This value is within the square-law region with an accuracy of about 8%. In cases when this power was less than necessary for producing the 10 V/m, the measured DC values were multiplied by the ratio of the necessary power and the actual power. The structure has a resonance at around 13 GHz. This resonance can be hardly tuned by the length of the dipole; we suppose that it is linked to the diode.

The directional sensitivity can be characterized by the ratio of the outputs at parallel and perpendicular polarizations. It is better than 1 : 100. The immunity of the probe against high electric fields was also checked. The 210 V/m field at the resonance frequency did not induced any observable degradation. Therefore, the probe should not be removed from the measuring chamber even at high field tests.

The DC output signals of the three detectors are individually amplified and digitalized with a resolution of 12 bit. The bit values of the voltage (LSBs) are feed to a personal computer via the serial port. A special program has been written in Windows environment which reads in and displays on the monitor the LSB values. The observer can save the actual data by mouse click in dedicated dat files. Each file

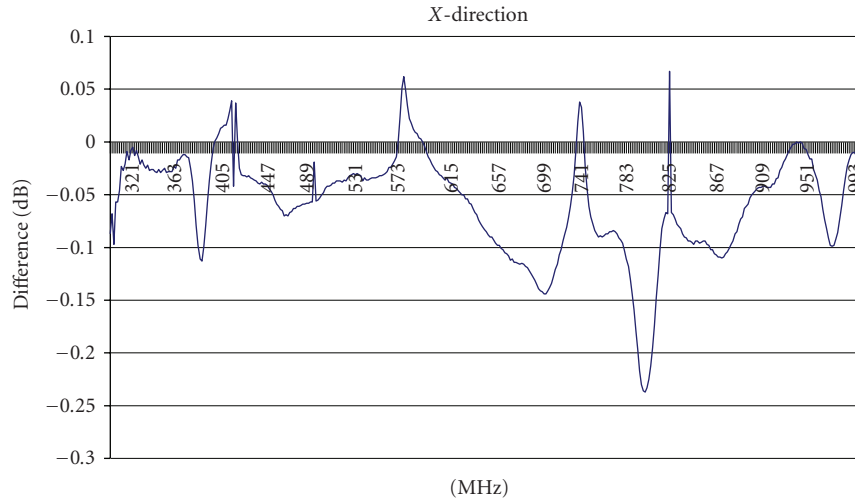


FIGURE 2: The difference in the transmission of the GTEM cell with and without loading in the screen printed resistive lines.

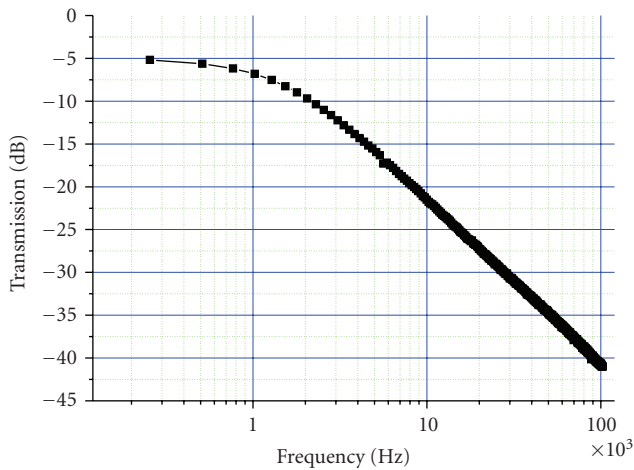


FIGURE 3: The measured transmission of the 2m-long resistive wire pair.

contains three LSB values, respectively, the three detectors. The syntax of the file name is: xxxx*****n.dat. The first four characters are the frequency of the measurement in GHz. The next characters are the identification of the investigation. The numeric character in the last position is the number of successive measurements under equivalent circumstances, it counts automatically. The processing of the raw data is carried out by a macro written in Excel. At first the values obtained from identical measurements are averaged, after that the zero shifts are corrected. Namely, the zero levels of the of the amplifiers are shifted in the positive direction, therefore any accidental temperature drift will not suppress them to negative voltage and even the smallest input equal only to 1 LSB can be detected. The actual value of the shift is measured at zero field and this value—usually less than 10 LSBs—is subtracted from the average of the measured data. The next step is the multiplication by the individual

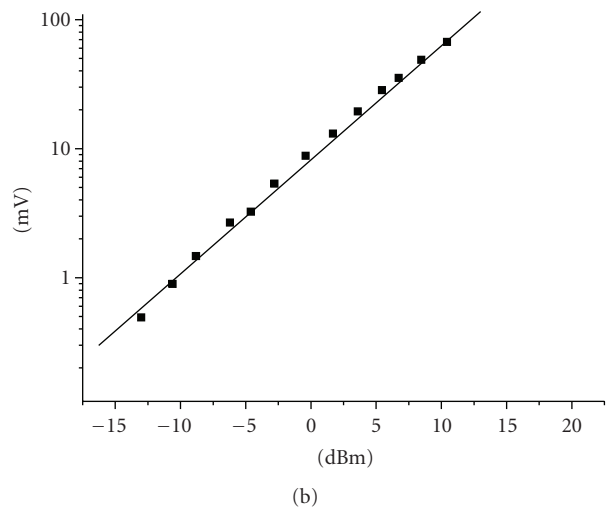
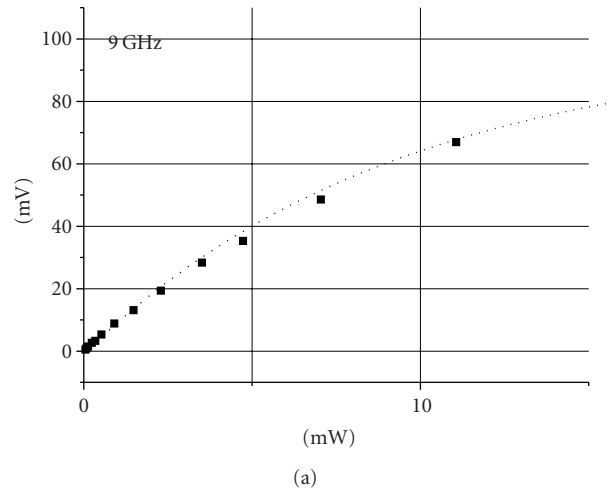


FIGURE 4: (a) The detector output voltage in the function of the power feed in the calibrated antenna. The dotted line is the exponential fit. (b) The same curve plotted in log-log scale.

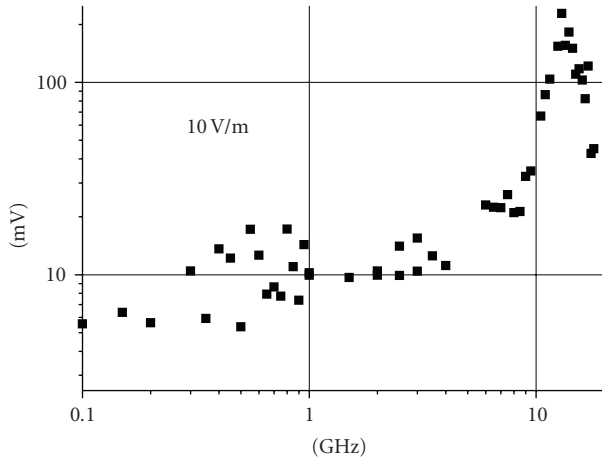


FIGURE 5: The diode DC output normalized to 10 V/m field strength.

frequency dependent sensitivities of the three detectors. The macro program reads out from the file name the frequency and applies the belonging sensitivity values. After that, the program sums the three components and calculates the square root too.

The basic realization of the device work according to the mentioned second method, and the detected signals can be observed only in the square-law region of the diodes. For this the amplification is set for 1 LSB = $6\ \mu\text{V}$, that is, the maximum of the scale is $4096 \cdot 6\ \mu\text{V} = 24.5\ \text{mV}$. However, the Excel macro can evaluate the E^2 values from the logarithmic calibration too. Of course the amplification factor should be decreased in this case.

3. CONCLUSIONS

A microwave E-field probe has been developed for measuring the field distribution in chambers used for radiated immunity test. The device is an accessory of the measuring chamber, it is connected to the connector mounted on the inner wall of the chamber by a 2m-long flexible resistive cable, which does not perturb significantly (less than 1 dB) the field distribution. The sensitivity is frequency dependent. The measured data are digitalized and feed into personal computer for further processing, which is performed expediently by special Microsoft Excel macro.

ACKNOWLEDGMENTS

The laboratory works of Mr. Tamás Berkó and Mr. Géza Laczkovich are appreciated. This work has been supported by the Hungarian Ministry of Economy and Transport under Contract no. GVOP-3.1.1.-2004-05-0354/3.0.

REFERENCES

[1] R. De Leo and V. M. Primiani, "Radiated immunity tests: reverberation chamber versus anechoic chamber results," *IEEE*

Transactions on Instrumentation and Measurement, vol. 55, no. 4, pp. 1169–1174, 2006.

- [2] F. Xiao, Y. Suganuma, K. Murano, M. Tayarani, and Y. Kami, "Design of a four-septum TEM cell for immunity/susceptibility test," *IEICE Transactions on Communications*, vol. E88-B, no. 8, pp. 3146–3151, 2005.
- [3] K. Murano, F. Xiao, and Y. Kami, "An immunity/susceptibility test method using electromagnetic wave of rotating polarization," *IEEE Transactions on Instrumentation and Measurement*, vol. 53, no. 4, pp. 1184–1191, 2004.
- [4] H. Bassen and G. S. Smith, "Electric field probes—a review," *IEEE Transactions on Antennas and Propagation*, vol. 31, no. 5, pp. 710–718, 1983.
- [5] G. S. Smith, "Analysis of miniature electric field probes with resistive transmission lines," *IEEE Transactions on Microwave Theory and Techniques*, vol. 29, no. 11, pp. 1213–1224, 1981.
- [6] B. Szentpáli, V. N. Tuyen, and G. Thúröczy, "Novel E-field probe for measurements in phantoms," in *Proceedings of the 10th Microcoll Conference*, pp. 453–456, Budapest, Hungary, March 1999.
- [7] B. Szentpáli, "Human exposure to electromagnetic fields from mobile phones," *Facta Universitatis, Series: Electronics and Energetics*, vol. 13, no. 1, pp. 51–72, 2000.
- [8] Type pyramid 1.8. producer: TKI-network Ltd.
- [9] Model 3115 double-ridged waveguide horn antenna and 3142C biconilog antenna, producer: ETS lindgren.

Research Article

Ka Band Phase Locked Loop Oscillator Dielectric Resonator Oscillator for Satellite EHF Band Receiver

S. Coco,¹ F. Di Maggio,² A. Laudani,¹ and I. Pomona²

¹ DIEES, University of Catania, V. A. Doria 6, 95125 Catania, Italy

² Selex Communications, V. S. Sonnino 6, 95045 Misterbianco (CT), Italy

Correspondence should be addressed to A. Laudani, alaudani@diees.unict.it

Received 30 November 2007; Revised 5 May 2008; Accepted 28 July 2008

Recommended by T. Kalkur

This paper describes the design and fabrication of a Ka Band PLL DRO having a fundamental oscillation frequency of 19.250 GHz, used as local oscillator in the low-noise block of a down converter (LNB) for an EHF band receiver. Apposite circuital models have been created to describe the behaviour of the dielectric resonator and of the active component used in the oscillator core. The DRO characterization and measurements have shown very good agreement with simulation results. A good phase noise performance is obtained by using a very high Q dielectric resonator.

Copyright © 2008 S. Coco et al. This is an open access article distributed under the Creative Commons Attribution License, which permits unrestricted use, distribution, and reproduction in any medium, provided the original work is properly cited.

1. INTRODUCTION

In satellite network links, the phase noise performance and the required spectral purity of the local oscillator of the LNB receiver are very important issues [1–3]. In this case, a fundamental local oscillator locked to a very stable external reference can be the best architectural solution.

In this paper, we present the design and fabrication of a Ka band phase locked loop (PLL) dielectric resonator oscillator (DRO) used as local oscillator in the low-noise block of a down converter (LNB) for an EHF band receiver.

In order to obtain the best performance in terms of low-phase noise and output spurious the dielectric resonator oscillator architecture at the fundamental frequency (19250 GHz) has been chosen. A good phase noise performance is obtained by using a very high Q dielectric resonator. In order to analyze the behavior of the dielectric resonator and the active component used in the oscillator core, apposite circuital models have been created. The circuit simulations have been performed by using the harmonic balance solver available in advanced design system (ADS) simulation tool.

The oscillator circuit is fabricated by using SMT components mounted on a multilayer substrate: this represents a quite unusual realization for EHF applications. Two pro-

totypes have been constructed and a full characterization has been carried out and the measurements show very good agreement with simulation results and then the PLL DRO has been integrated in a low-noise block down converter for EHF band satellite communication terminals.

The design, simulations, fabrication, and measurements have been carried out at Selex-Communications site of Misterbianco (CT), Italy.

2. OSCILLATOR DESIGN

The fundamental oscillation frequency is 19250 GHz. The architecture of the DRO circuit is based on a series feedback network, exhibiting a good performance in terms of a low drift of the oscillation frequency with respect to load variations [4–7]. A GaAs FET (Excelics EPB018A7) was chosen as active component both for its easy assembling and for its good gain and noise performance at working frequencies.

Because of the scarce information provided by the manufacturer for this component (only S parameters and gain at 1 dB compression point are given), it has been necessary to create an apposite nonlinear model to be used for the simulations. As starting point we used a Triquint own model available in the advance design system simulation tool

TABLE 1: LNB receiver performances.

Input frequency range	202 ÷ 21.2 GHz
Output frequency range	90 ÷ 1950 MHz
Gain	55 dB
Noise figure	1.6 dB
Gain flatness	
Any 500 MHz	3.5 dB
Any 40 MHz	1.6 dB
Spurious emission	>60 dBc
Phase noise	
@ 1 KHz	78 dBc/Hz
@ 10 KHz	84 dBc/Hz
@ 100 KHz	105 dBc/Hz
@ 1 MHz	120 dBc/Hz

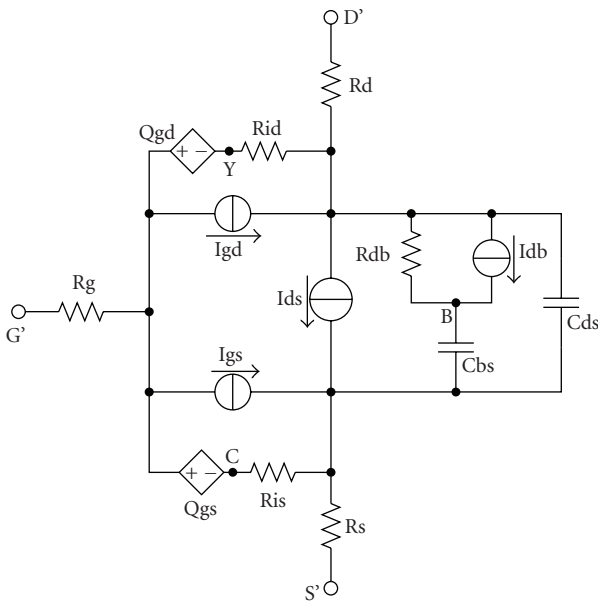


FIGURE 1: Triquint own model.

(Figure 1). This model has been improved by adding series inductances and resistances to the three device terminals and other capacitances in order to take into account the parasitic effects of the package (Figure 2).

Model parameters have been evaluated by using the information available from the manufacture. A dielectric resonator of high permittivity ceramic material has been chosen as resonant element; it is characterized by high temperature stability and a dielectric constant ranging between 30 and 40. In order to obtain high values of the quality factor (1000–40000), a metallic cover has been used. The desired phase noise characteristics are achieved thanks to the high-impedance path coupling the DRO to the other components. In order to simulate the behavior of the dielectric resonator within the oscillator circuit,

an apposite S parameters model was created. This model foresees two microstrip lines placed in close proximity of the resonator and an apposite block describing the coupling effects between the dielectric resonator and the microstrip lines by using S parameters.

The simulation results for this model gives a resonant frequency of 19.250 GHz as expected.

To obtain good phase noise performance, the oscillator has been locked to an external reference by using a PLL architecture. The block diagram of the PLL is shown in Figure 3. The DRO output is compared with a 10 MHz reference in the main PLL circuit. The external reference signal is first filtered by another PLL circuit (cleaner) used to lock the output signal of a voltage controlled crystal oscillator (VCXO). The charge pump output is used to drive a varactor loaded with a microstrip stub inside the cavity in which the overall DRO is housed. The loop bandwidth is then optimized according to the phase noise specifications. A microcontroller shown in Figure 3 manages frequency assignment for the two PLLs.

3. TECHNOLOGY

Bare die devices mounted on the traditional hard substrate (Alumina) are generally used for EHF applications. On the other hand, in very complex circuits for low-frequency applications multilayer substrates and surface mounted technology are normally used. For the realization of this PLL DRO oscillator we made the choice of using a new ceramic multilayer substrate and packaged surface mounted devices (SMD), now available for high-frequency applications. In this way, all the complex oscillator circuit has been compactly fabricated in a small-size area employing easy mounting and low-cost materials. The multilayer substrate is composed by a ceramic layer ($\epsilon_r = 9.9$), on which the microstrip lines have been realized, and four FR4 ($\epsilon_r = 4.4$) layers used for the other interconnections. The final compact layout is shown in Figure 4. The dielectric resonator is visible inside the cavity. Even if at these frequencies distributed DC-blocks are generally used because of their low-insertion losses, in our case a more compact solution employing ceramic capacitances has been adopted. The prototype fabricated is shown in Figure 5. The board has been housed inside a metallic structure, closed by a cylindrical metallic waterproof cover (Figure 5).

4. SIMULATIONS AND MEASUREMENTS

The two circuitual models have been used in the simulation of the complete oscillator circuit (Figure 6). Each lumped and distributed component has been optimized in order to reach the required phase noise and output power. The computed phase noise and output signal spectrum are shown in Figure 7. The phase noise and the output spectrum measured at the LNB output interface are shown in Figure 8. The CW input signal at 20700 MHz has been fed by a source generator. The measurements exhibit a very good

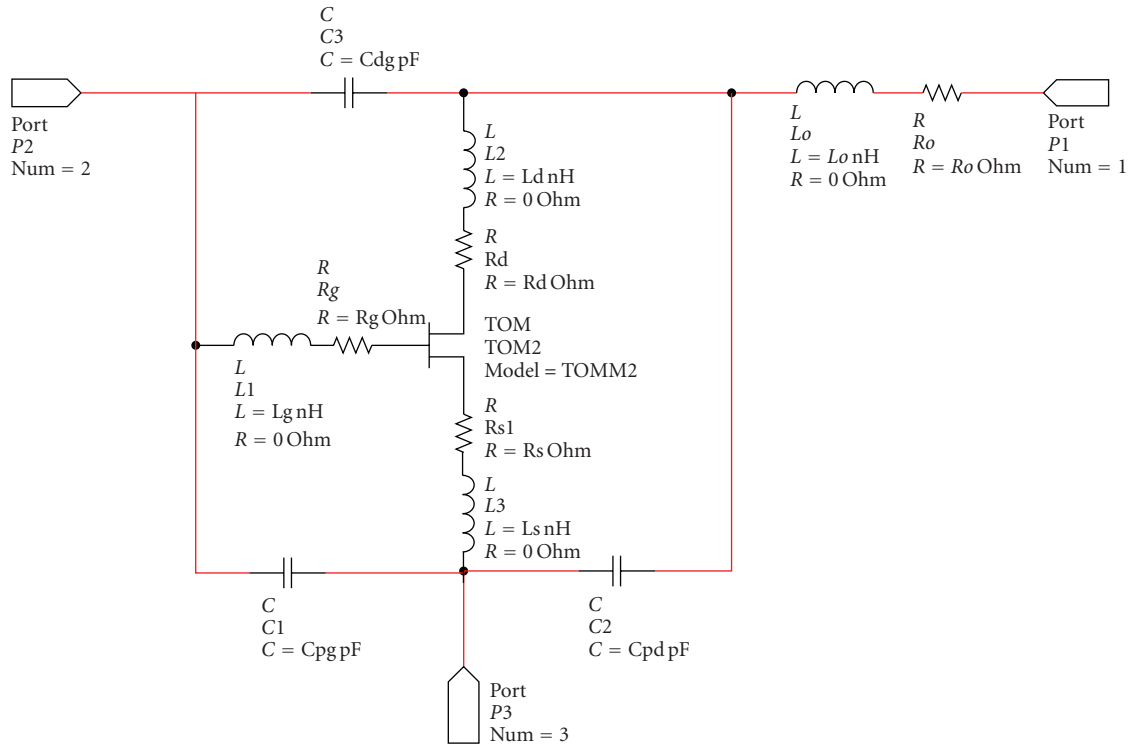


FIGURE 2: Improved model taking into account the parasitic effects of the package.

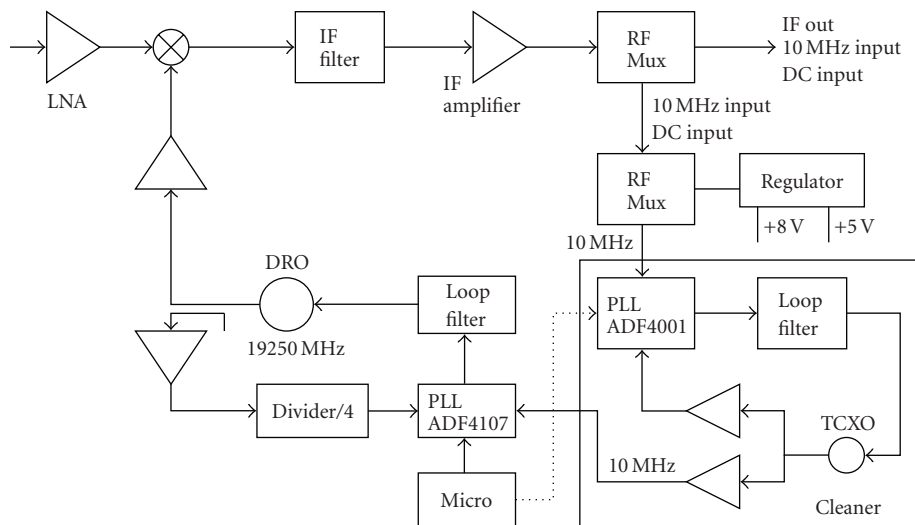


FIGURE 3: PLL block diagram.

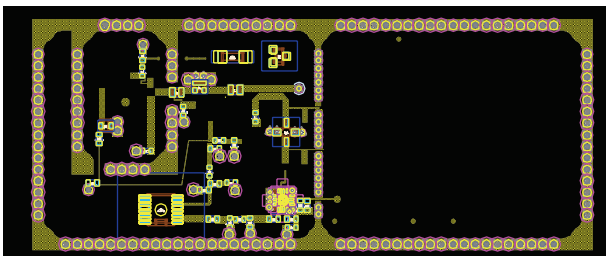


FIGURE 4: Final compact layout.

performance both in terms of phase noise and in terms of spectral purity.

5. LNB TEST RESULTS

The PLL DRO described above has been integrated in the low-noise block of the down converter for EHF band satellite communication terminals. The most significant performances obtained are summarized in Table 1.

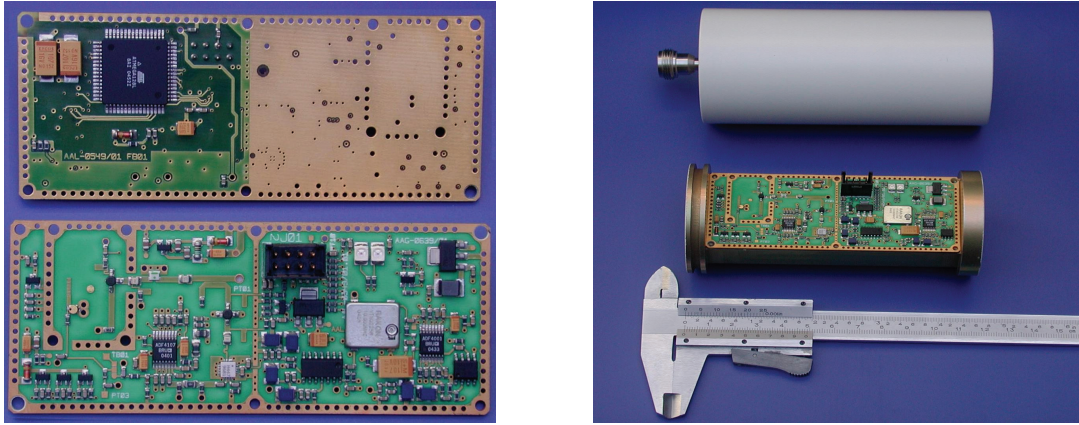


FIGURE 5: The prototype.

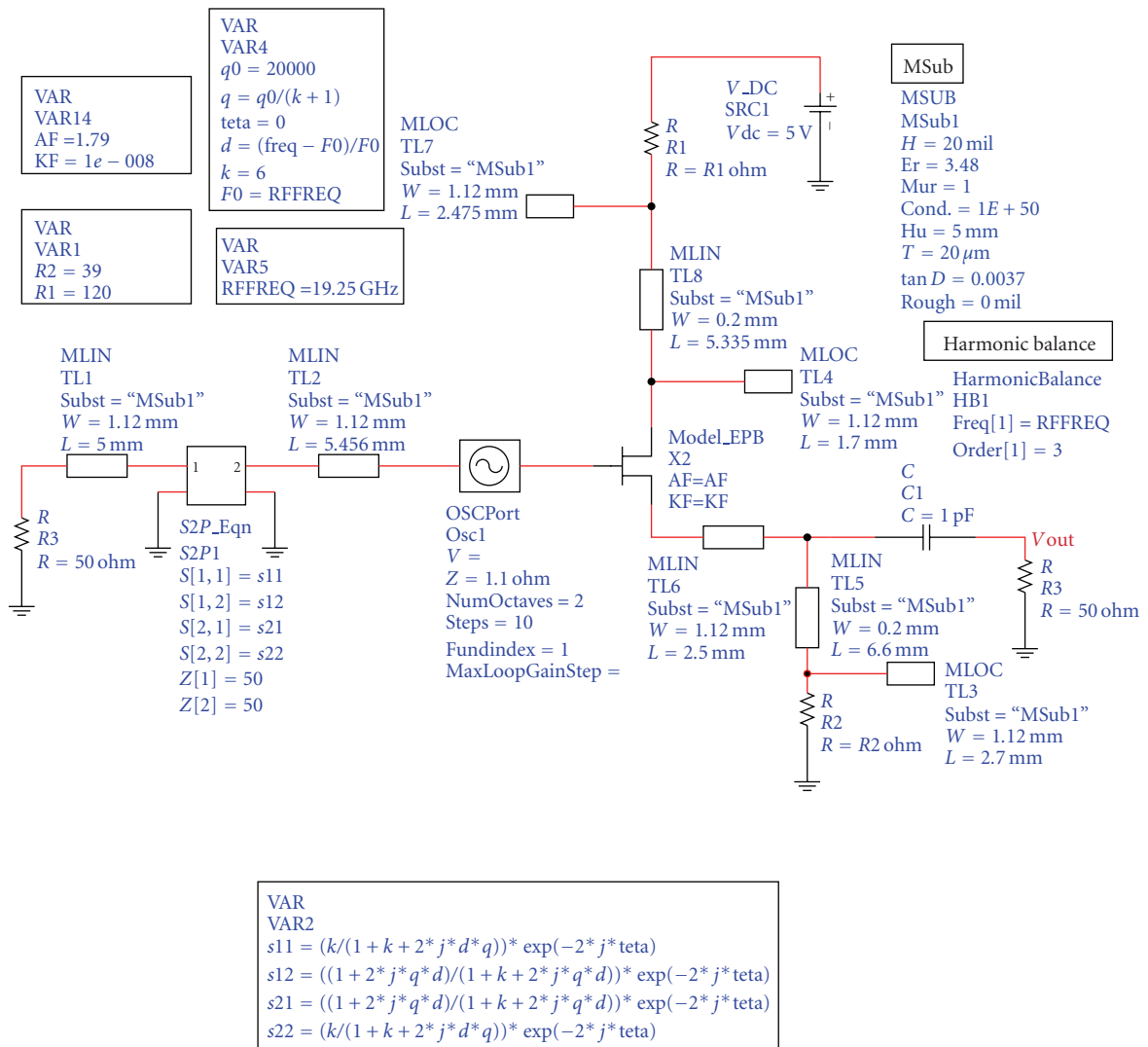


FIGURE 6: The complete oscillator circuit used for simulation.

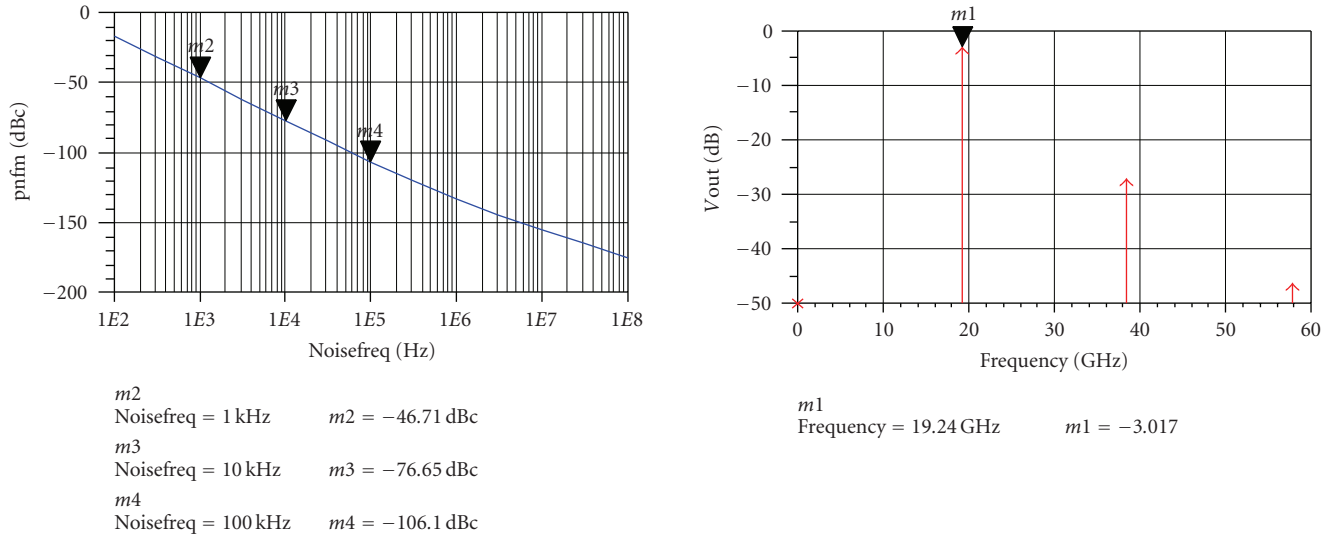


FIGURE 7: Simulation results.

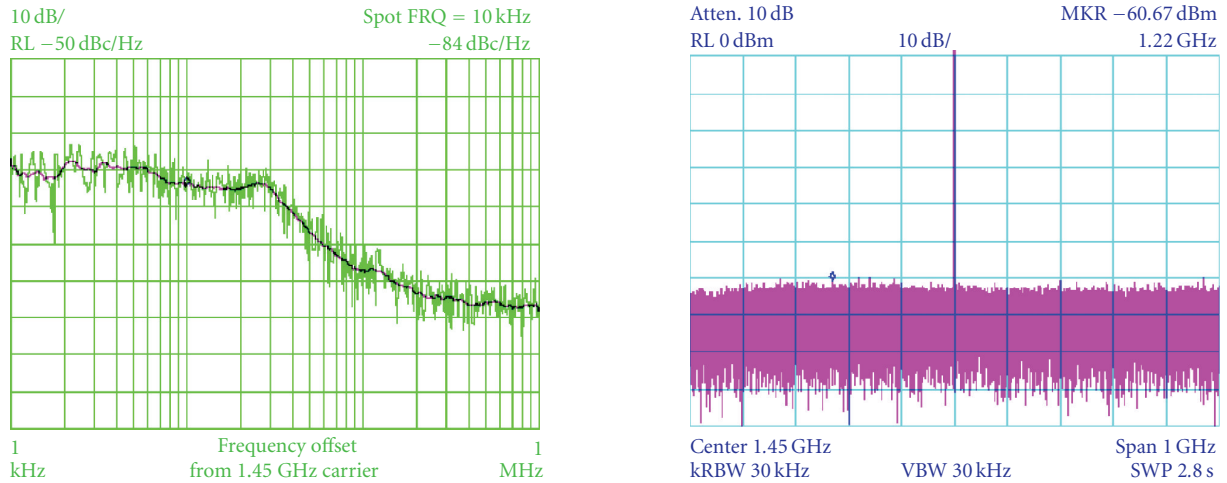


FIGURE 8: The phase noise and the output spectrum measured at the LNB output interface.

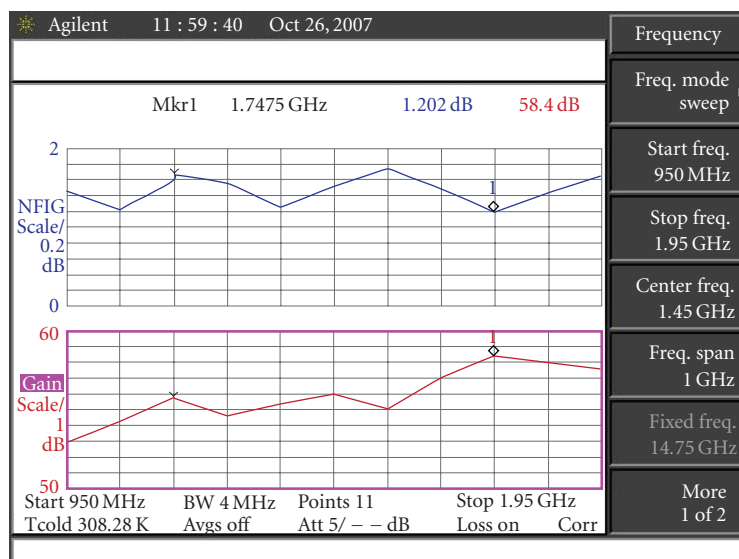


FIGURE 9: LNB gain and noise figure.

The phase noise measured is compatible with end-to-end forward performances as recommended in DVB-S2 standard. The LNB noise figure and gain are shown in Figure 9.

6. CONCLUSIONS

In this paper, a state-of-the-art phase locked DRO for an EHF low-noise block down converter is presented. The circuitual models, appositely created to describe the behavior of the dielectric resonator and the active component used in the oscillator core, have provided a good methodology in order to speed the design process. The DRO has been used in a low-noise block down converter for EHF band satellite communication terminals. The phase noise obtained makes this LNB receiver particularly suitable for DVB-S2 applications.

REFERENCES

- [1] R. G. Rogers, *Low Phase Noise Microwave Oscillator Design*, Artech House, Boston, Mass, USA, 1991.
- [2] B. Hitch and T. Holden, "Phase locked DRO/CRO for space use," in *Proceedings of the 51st IEEE International Frequency Control Symposium*, pp. 1015–1023, Orlando, Fla, USA, May 1997.
- [3] D. H. Shin, K. K. Ryu, D. P. Chang, M. Q. Lee, and I. B. Yom, "A 26.4 GHz phase locked oscillator for space application," in *Proceedings of the 17th Asia-Pacific Microwave Conference (APMC '05)*, vol. 5, p. 4, Suzhou, China, December 2005.
- [4] W. H. Hayward, *Introduction to Radio Frequency Design*, The American Radio Relay League, Newington, Conn, USA, 1994.
- [5] R. W. Rhea, *Oscillator Design and Simulation*, Noble, Mumbai, India, 1995.
- [6] U. L. Rohde, *Microwave and Wireless Synthesizers: Theory and Design*, Wiley-Interscience, New York, NY, USA, 1997.
- [7] E. A. Sweet, *MIC & MMIC Amplifier and Oscillator Circuit Design*, Artech House, Boston, Mass, USA, 1990.

Research Article

The Novel Microwave Stop-Band Filter

R. E. Chernobrovkin, I. V. Ivanchenko, A. M. Korolev, N. A. Popenko, and K. Yu. Sirenko

Institute of Radiophysics and Electronics, National Academy of Sciences of Ukraine, 12 Proskury Street, 61085 Kharkov, Ukraine

Correspondence should be addressed to N. A. Popenko, buran@ire.kharkov.ua

Received 30 November 2007; Revised 5 March 2008; Accepted 15 April 2008

Recommended by Tibor Bercei

The stop-band filter with the new band-rejection element is proposed. The element is a coaxial waveguide with the slot in the centre conductor. In the frame of this research, the numerical and experimental investigations of the amplitude-frequency characteristics of the filter are carried out. It is noted that according to the slot parameters the two typical resonances (half-wave and quarter-wave) can be excited. The rejection band of the single element is defined by the width, depth, and dielectric filling of the slot. Fifth-order Chebyshev filter utilizing the aforementioned element is also synthesized, manufactured, and tested. The measured and simulated results are in good agreement. The experimental filter prototype exhibits the rejection band 0.86 GHz at the level -40 dB.

Copyright © 2008 R. E. Chernobrovkin et al. This is an open access article distributed under the Creative Commons Attribution License, which permits unrestricted use, distribution, and reproduction in any medium, provided the original work is properly cited.

1. INTRODUCTION

Review of the microwave filters technology, applications perspective, as well as filter designs is described in [1]. The narrow-band tunable filters are usually realized by using the rectangular waveguide with the dielectric resonator [2] or microstrip resonators [3]. In order to provide the wideband filter, the resonators with low Q-factor such as the ring resonator with direct-connected orthogonal feed lines [4] or coplanar stripline resonators [5] are applied.

The slot resonator as a basic element of the microwave filter has been proposed earlier in the paper [6]. The main advantages of this resonator are the small sizes, the simplicity of manufacturing, as well as a possibility of its natural integration into the coaxial line. In this paper, the slot resonators on the TEM waves are used in designing the stop-X-band filter.

The paper is organized as follows. In Section 2, the different designs of the band-rejection element as well as the EM field distributions in the slot are considered. Furthermore, the behavior of the resonance frequency and the loaded Q-factor is studied depending on the slot dimensions. The results of experimental investigations of the rejection filter with a single slot are discussed in Section 3 and point to the capability of developing the more complicated

filter designs. Section 4 is devoted to the synthesis and experimental investigations of the Chebyshev rejection filter prototype.

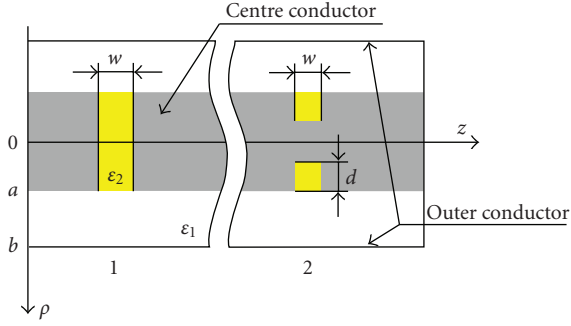
2. BAND-REJECTION ELEMENT

Schematic view of the novel band-rejection element is presented in Figure 1. The band-rejection element is the axial-symmetrical structure which consists of the coaxial waveguide with the centre conductor radius a , and outer conductor b , respectively. The coaxial waveguide is filled by the dielectric with permittivity ϵ_1 . The slot in the centre conductor has the width w and the depth d (Figure 1) and it is filled by the dielectric with permittivity ϵ_2 . Two different filter designs can be realized by means of both the complete slot $d = a$ (Figure 1(1)) and the partial slot $d < a$ (Figure 1(2)).

In order to excite the resonance with the component $H_p = 0$ in this structure, the condition $w \ll d$ has to be realized [6]. In this case, the magnetic field distribution is the axial-symmetrical one. It should be noted that the two types of resonance can be excited in this structure depending on the relation between the slot depth d and the centre conductor radius a (Figure 1). The maximal magnitude is located in the slot centre for $d = a$ (Figure 2(a));

TABLE 1: Geometrical and physical parameters of the band-rejection element.

	$w = 0.5$ mm $d = 6.0$ mm $\epsilon_2 = 1$	$w = 0.5$ mm $d = 5.0$ mm $\epsilon_2 = 1$	$w = 1.5$ mm $d = 5.0$ mm $\epsilon_2 = 1$	$w = 0.5$ mm $d = 9.0$ mm $\epsilon_2 = 3.78$	$w = 1.5$ mm $d = 9.0$ mm $\epsilon_2 = 3.78$
f_0 GHz	9	11	10.7	10.3	10.27
Q-factor	17	17	5	91	37
	Quarter-wave resonance			Half-wave resonance	

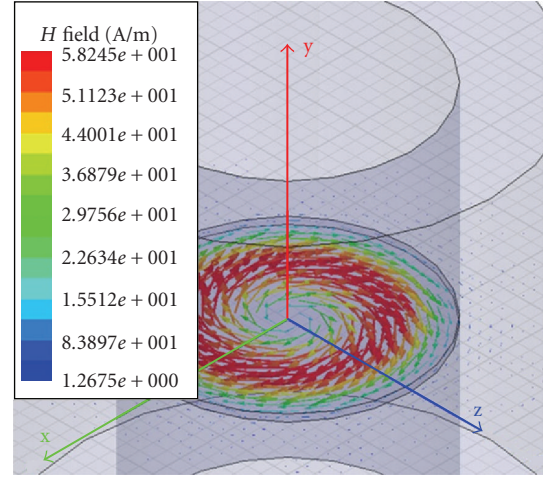
FIGURE 1: The problem geometry: (1) $a = d$; (2) $a > d$.

whereas for $d < a$, the maximal magnitude is located on the centre conductor surface (Figure 2(b)). Based on the amplitude distributions of the magnetic field noted above, the authors of [6] called “half-wave resonance” when $d = a$ (Figure 2(a)) and “quarter-wave resonance” when $d < a$ (Figure 2(b)).

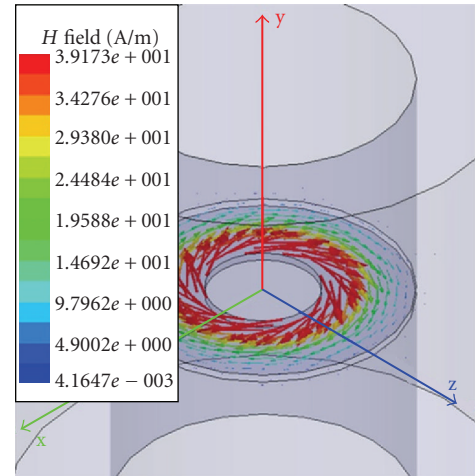
From the beginning, let us analyze the influence of the depth (d), width (w), and permittivity (ϵ_2) on the single-slot performance. For the quarter-wave resonance ($d < a$), the slot-depth increase leads to moving the resonance frequency from $f_0 = 9$ GHz to $f_0 = 11$ GHz (Figures 3(a) and 3(b), Table 1). In this case, the slot-width variation from 0.5 mm to 1.5 mm results in the Q-factor changing about 72% whereas the resonant frequency is slightly changed (Figures 3(b) and 3(c), Table 1).

We note that for the half-wave resonance ($a = d$), the slot width variation points to the similar results (Figures 4(a) and 4(b)). It is quite clear that the dielectric filling of the slot leads to changing the resonant frequency of the single element. So, the dielectric filling of the slot allows reducing the radius of the centre conductor of the given coaxial waveguide. In this case, there is a possibility to provide the efficient rejection-band control of the aforementioned filter.

With these remarks in mind, one may summarize that the resonance frequency is defined by the slot depth and the dielectric permittivity ϵ_2 . At the same time, the Q-factor depends on the slot width and dissipations in the dielectric and the metal. For the illustration of these statements, the dependences of numbered above parameters on the slot dimensions are shown for both the half-wave ($d = a$) and quarter-wave ($d < a$) (Figures 5 and 6) resonances. In both cases, the radius of centre and outer conductors are constant. We have chosen the permittivity $\epsilon_2 = 1$ for the slot when $d < a$ and $\epsilon_2 = 3.78$, $\tan\delta = 0.0001$



(a)



(b)

FIGURE 2: The magnetic field distribution in the slot: (a) $d = a$; (b) $d < a$.

for the slot when $d = a$. The choice of such values of dielectric permittivity ϵ_2 allows us to remain in the same frequency band. For both slots, the resonance frequency has the linear dependence on the slot depth (Figure 5). Q-factor reduction is explained by increasing the radiation losses with the slot-width increase (Figure 6). The highest value of Q-factor can be achieved by using the slot-width parameter $d = a$.

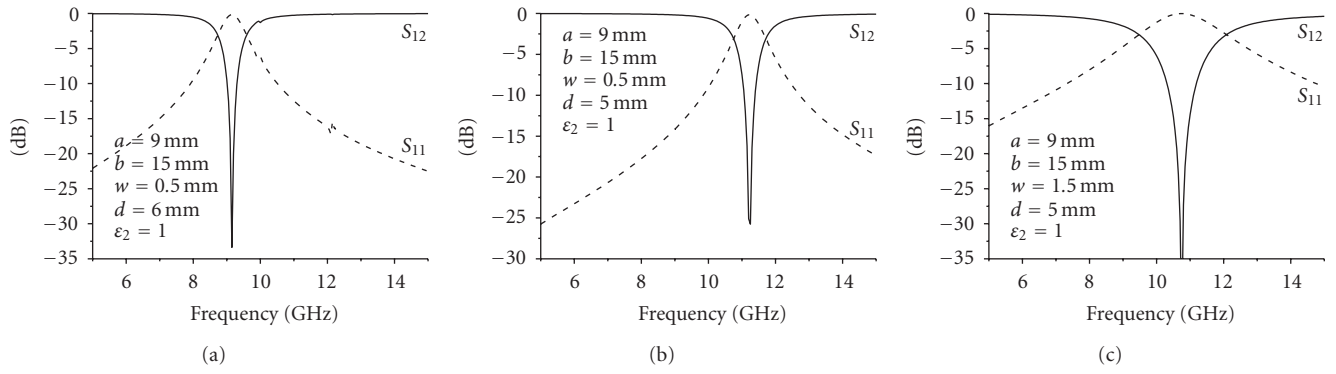


FIGURE 3: Amplitude-frequency characteristics of the band-rejection element in the case of the quarter-wave resonance.

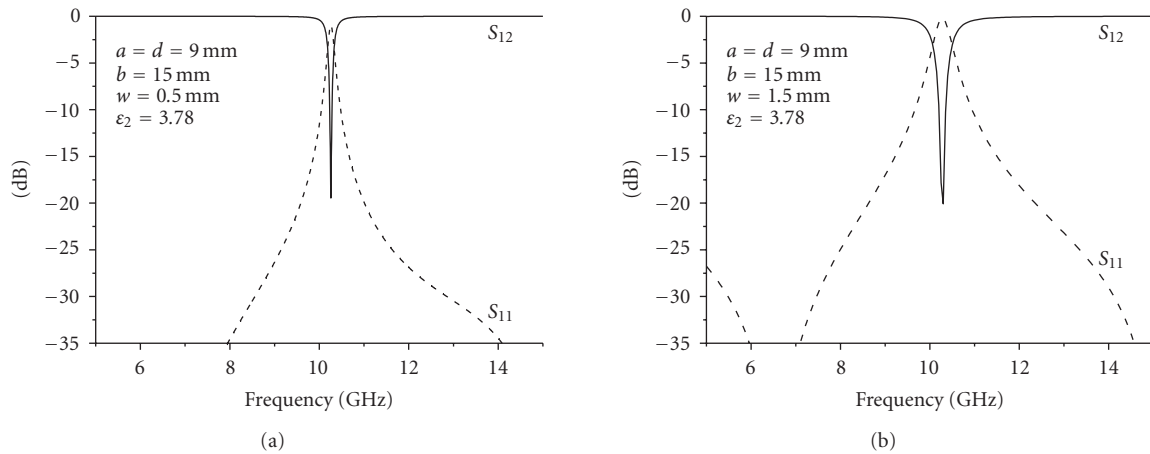


FIGURE 4: Amplitude-frequency characteristics of the band-rejection element in the case of the half-wave resonance.

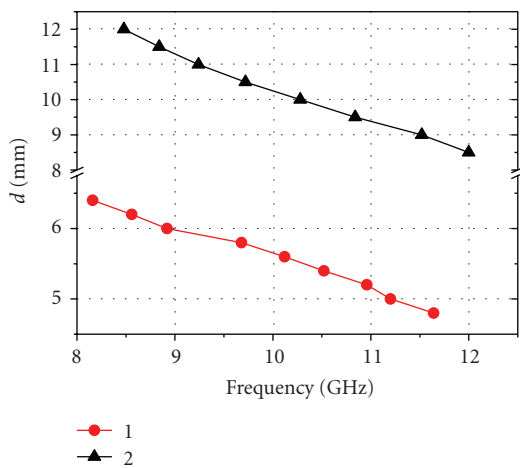


FIGURE 5: The dependence of the resonance frequency on the slot depth: (1) $a = 9 \text{ mm}$, $b = 15 \text{ mm}$, $w = 0.5 \text{ mm}$, $\epsilon_1 = \epsilon_2 = 1$; (2) $a = d$, $b = 15 \text{ mm}$, $w = 0.5 \text{ mm}$, $\epsilon_1 = 1$, $\epsilon_2 = 3.78$.

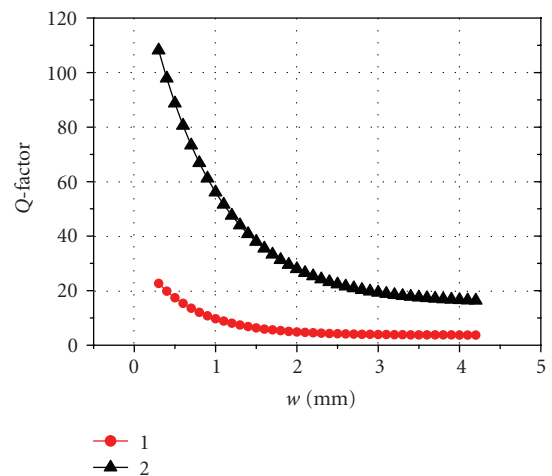


FIGURE 6: The dependence of the loaded Q-factor on the slot width: (1) $a = 9 \text{ mm}$, $b = 15 \text{ mm}$, $d = 5.5 \text{ mm}$, $\epsilon_1 = \epsilon_2 = 1$; (2) $a = d = 9 \text{ mm}$, $b = 15 \text{ mm}$, $\epsilon_1 = 1$, $\epsilon_2 = 3.78$.

3. EXPERIMENTAL VERIFICATION

Experimental investigations of characteristics of the single-slot filter prototypes were carried out on the Agilent network

analyzer PNA-L N5230A in the frequency band 8–14 GHz. The manufactured filter prototype is shown in Figure 7. The filter parameters are as follows: $d = a = 9 \text{ mm}$, $b = 15 \text{ mm}$, $\epsilon_1 = 1$, and $\epsilon_2 = 3.78$. A fair agreement

TABLE 2: The parameters of the Chebyshev filter.

The number of resonators	Ripple [dB]	f_1 [GHz]	f_2 [GHz]	f_0 [GHz]	$f_2 - f_1$ [GHz]	Source and load [OH]
5	0.1	9.5	10.5	10	1	50



FIGURE 7: General view of the filter prototype with the single slot.

between the measured and simulated S_{12} -parameters for the single slot with different widths ($w = 1$ mm and $w = 2$ mm) is observed (Figure 8). The dissimilarity at the resonance frequency is less than 0.05 GHz and can be explained by the manufacturing inaccuracy of the filter as well as by the difference between the real dielectric permittivity in the experiment and that used in the simulations.

4. SYNTHESIS OF THE CHEBYSHEV FILTER

The stop-band filter with initial parameters mentioned in Table 2 will be synthesized below. The slots filled with the air ($\epsilon_2 = 1$) in the case of quarter-wave resonance were chosen as a basic element of this filter. Equivalent circuit of the filter is shown in Figure 9 (top). Based on the simulated results, the values of all elements of the equivalent circuit as well as the resonant frequency and Q-factor of each resonator were determined. The initial values of the geometric parameters of slots (w and d) were chosen from Figures 5 and 6. The desirable impedances were provided by the changing of centre conductor radius a . Further filter optimization was carried out by means of the full wave simulator developed by us earlier [6]. In this case, the resonators are located at the distance $3\lambda/4$ ($\lambda = 30$ mm) from each other to provide the minimal coupling between resonators (Figure 9, bottom). As the goal function, the S-parameters were chosen, and the slot width w and the slot depth d were varied within the limits $\pm 5\%$.

The optimized filter with parameters highlighted in Table 3 was designed, manufactured, and investigated. The S-parameters of the filter prototype noted above are shown in Figure 10. Based on the analysis of these data, we can formulate some conclusions, namely, (i) the measured S-parameters are in good agreement with the simulated ones at the most frequency points over the entire pass-band and

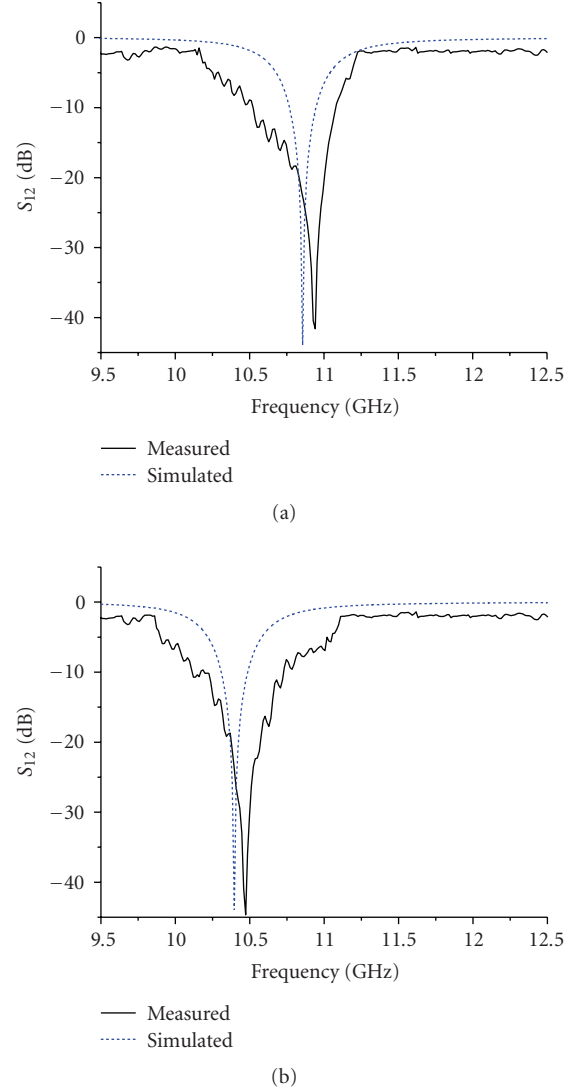
FIGURE 8: S_{12} -parameter of the filter prototype with the single slot: (a) $w = 1$ mm; (b) $w = 2$ mm.

TABLE 3: The geometrical parameters of the filter.

The number of resonators	1	2	3	4	5
w	0.29 mm	1.0 mm	1.25 mm	1.0 mm	0.29 mm
d	5.6 mm	5.6 mm	5.6 mm	5.6 mm	5.6 mm
a	9 mm	10.7 mm	11.72 mm	10.7 mm	9 mm

stop-band; (ii) the rejection band is 0.86 GHz at the level -40 dB.

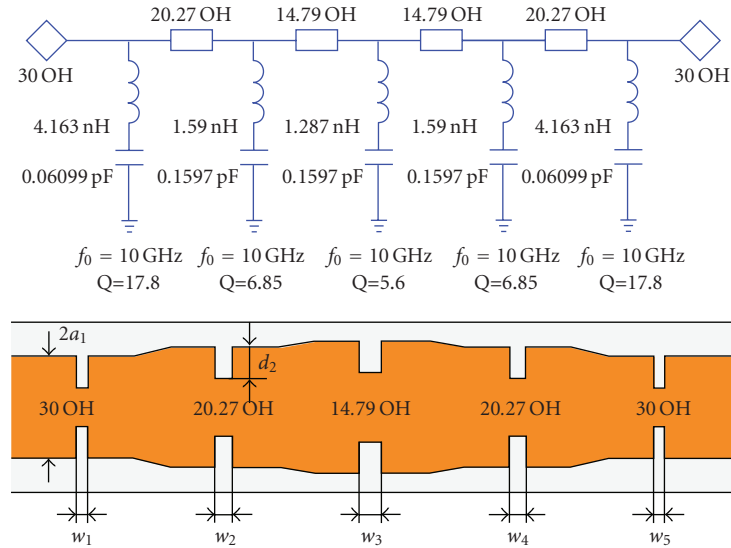


FIGURE 9: Low-pass block diagram and the general view of the Chebyshev filter prototype.

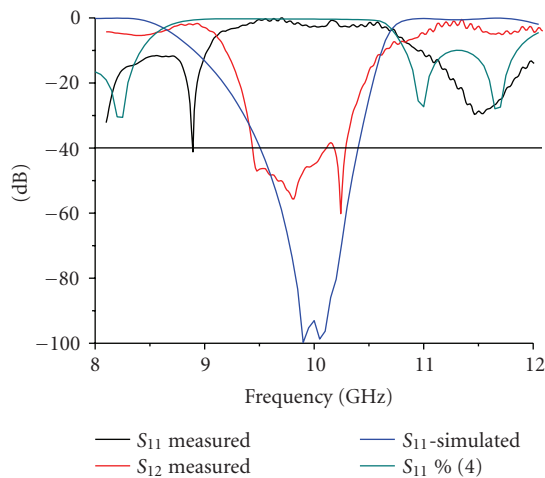


FIGURE 10: The measured and simulated S-parameters of the Chebyshev filter prototype.

5. CONCLUSIONS

The original band-rejection element as the slot in the centre conductor of the coaxial waveguide for designing the microwave stop-band filters is presented. The half-wave and quarter-wave resonances which are excited in this element have been studied and analyzed. The band-rejection element has been designed and manufactured. It has been found that for both cases the slot-width increase from $w/a = 0.056$ to $w/a = 0.23$ leads to decreasing the loaded Q-factor on 22%. The resonance frequency depends on the slot depth. The good coincidence of calculated and measured data is observed. Fifth-order Chebyshev filter with the given band-rejection element has been also synthesized, manufactured, and investigated. The measured S-parameters are in good agreement with the numerical ones at the most frequency points over the entire pass-band and stop-band. Notice

that the filter characteristics are close to the simulated ones without any trimming elements. The rejection band is 0.86 GHz at the level -40 dB. The proposed stop-band filter can be naturally integrated into the coaxial waveguides and seems to be very attractive in different applications.

REFERENCES

- [1] I. C. Hunter, L. Billonet, B. Jarry, and P. Guillon, "Microwave filters-applications and technology," *IEEE Transactions on Microwave Theory and Techniques*, vol. 50, no. 3, pp. 794–805, 2002.
- [2] Y. M. Poplavko, Y. V. Prokopenko, V. I. Molchanov, and A. Dogan, "Frequency-tunable microwave dielectric resonator," *IEEE Transactions on Microwave Theory and Techniques*, vol. 49, no. 6, pp. 1020–1026, 2001.
- [3] C. Quendo, E. Rius, and C. Person, "Narrow bandpass filters using dual-behaviors resonators," *IEEE Transactions on Microwave Theory and Techniques*, vol. 51, no. 3, pp. 734–743, 2003.
- [4] L.-H. Hsieh and K. Chang, "Compact, low insertion-loss, sharp-rejection, and wide-band microstrip bandpass filters," *IEEE Transactions on Microwave Theory and Techniques*, vol. 51, no. 4, pp. 1241–1246, 2003.
- [5] Y.-H. Suh and K. Chang, "Coplanar stripline resonators modeling and applications to filters," *IEEE Transactions on Microwave Theory and Techniques*, vol. 50, no. 5, pp. 1289–1296, 2002.
- [6] V. P. Pazynin and K. Yu. Sirenko, "The pulse TE_{0n} - and TM_{0n} -waves transform by axially-symmetrically waveguide units. Slot resonators," *Electromagnetic Waves and Electronic Systems*, vol. 10, no. 10, 2005 (Russian).

Research Article

Passive Frequency Selective Surface Array as a Diffuser for Destroying Millimeter Wave Coherence

Saiful Islam, Johan Stiens, Gert Poesen, Irina Jaeger, and Roger Vounckx

Laboratory for Micro- and Photonelectronics, Department of Electronics and Informatics, Vrije Universiteit Brussel, Pleinlaan 2, 1050 Elsene, Belgium

Correspondence should be addressed to Saiful Islam, sislam@etro.vub.ac.be

Received 30 November 2007; Accepted 15 May 2008

Recommended by Tibor Berceci

This paper presents the design, construction, and testing of grounded frequency selective surface (FSS) array as a diffuser for destroying millimeter wave coherence which is used to eliminate speckle in active millimeter wave imaging. To create stochastically independent illumination patterns, we proposed a diffuser based on random-phase distributions obtained by changing the incident frequency. The random-phase diffuser was obtained by mixing up the phase relations between the cells of a deterministic function (e.g., beam splitter). The slot length of FSS is the main design parameter used to optimize the phase shifting properties of the array. The critical parameters of the diffuser array design, such as phase relation with slot lengths, losses, and bandwidth, are discussed. We designed the FSS arrays with finite integral technique (FIT), fabricated by etching technique, and characterized the *S*-parameters with a free-space MVNA, and measured the radiation patterns with a BWO in motorized setup.

Copyright © 2008 Saiful Islam et al. This is an open access article distributed under the Creative Commons Attribution License, which permits unrestricted use, distribution, and reproduction in any medium, provided the original work is properly cited.

1. INTRODUCTION

Free-space active millimeter wave (mm-wave) systems have gained more and more attraction during the last few years due to their indoor security applications. There is no incoherent mm-wave source, and highly coherent mm-wave sources produce speckle in active mm-wave imaging of conceal objects because of interference phenomenon [1]. The speckle problem is especially important for active mm-wave imaging as the wavelength in this frequency range is close to the object dimension [2, 3]. We present here a frequency selective surface (FSS)-based diffuser array to destroy the coherence of mm-wave sources. This optical technique utilizes stochastically independent phase patterns obtained from a grounded FSS array. Nongrounded FSSs have limited bandwidth and can be viewed as filters for plane waves at any angles of incidence [4]. They are well known in the literature for their filtering characteristics at microwave and millimeter wave frequencies. Generally, FSSs are based on two-dimensional periodic lattice decorated with resonant elements—including dielectric or metallic circuit designs [5]. This paper considers the building block of a simpler and more versatile architecture, where the reflection

phase depends on the resonant slot length. Such elements are widely employed as grounded FSS. Using ground plane to the back side of FSS and also by choosing the proper slot dimensions and unit cell dimensions, such structure can be designed for full W-band (75–110 GHz) application. The resonant frequency and the phase of such slotted FSSs can be controlled by varying slot lengths [6, 7]. The phase variation with slot length variation is more significant near the resonant frequency [7]. This property of the grounded FSS is important to design a random-phase diffuser to destroy the coherence of mm-wave sources. So, it is a novel idea to use FSS cells with different slot length to control the phase of individual element of a diffuser array. A diffuser system is an antenna array which receives coherent plane wave and reflects noncoherent wave by introduction different phase delay in the reflected wave at each single frequency within the W-band. The diffuser applies the temporal phase variation to the reflected wave. Actually, due to the different amount of phase delay, the coherent plane wave after reflection will convert to noncoherent illumination. The diffuser is like a phase shifter to modulate the phase properties of coherent wave. If we excite the proposed array with a monochromatic wave (single-frequency), the reflected

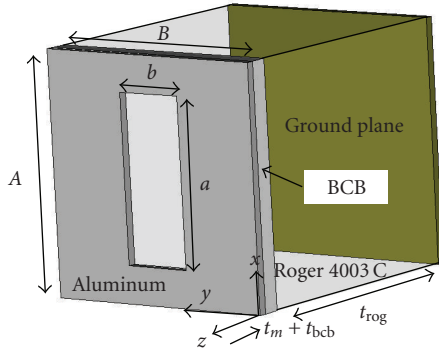


FIGURE 1: Unit cell of rectangular slot grounded FSS.

wave is still a monochromatic, but the phase pattern will be different, and the amplitude will be direction-dependent. To design such a diffuser different phase delay, elements are needed. In the proposed diffuser system, the delay element is replaced with FSS cells of different slot lengths.

Reflect array with patch antenna requires tight fabrication tolerances to achieve desired phase value, as the patch size versus phase curves are extremely nonlinear [8]. Because of the rapid phase change around resonance, most reflectarray elements have lengths within $\pm 5\%$ of the nominal resonant length [8, 9]. This causes phase errors which results for changes in frequency greater than a few percent. Random phase errors due to etching tolerances, is usually more critical for patch antenna than Slot FSS because of the large slope of the phase versus patch-size curves. This effect also limits the bandwidth. So, it is difficult to design deterministic function or to get controlled phase response at the desired frequency. By using thick substrate, the slope of phase versus patch size curve can be reduced but the quality factor (Q) and the total phase range decrease. As explained in [10], the dual resonant response of a two layer-grounded FSS array of dissimilar size patch elements was used to overcome the limitations associated with the use of thick substrates, but the structure cannot be printed on a single substrate surface; double-side mask alignment is needed. This means difficulties with the design accurately. The present design excludes the possibility of obtaining dual frequency operation since independent control of the dimensions of the slot length is normally required in each unit cell. It is easier than multilayer design in “[10].” The phase versus frequency curve of grounded FSS is more linear so no need of tight fabrication tolerances like patch antenna. The proposed periodic array structure can be printed on a single substrate surface; double-side mask alignment is not needed [11]. The structure is the superior alternative to other broadband elements as the construction of the structure is very much simpler and cheaper.

This paper is organized as follows. Section 2 describes the design, fabrication, and testing of slot length dependence phase variation of grounded FSS. In practice, the designs of FSSs with different slot lengths show that FSS can be used as phase-delay circuit. In Section 3, the same concept is applied to design an FSS array compose of

different slot lengths to split the coherent mm-wave beam for a deterministic function analysis. In Section 4, the FSS cells of the beam splitter array explained in Section 3 were rearranged to get a stochastically independent phase patterns. The reshuffled array gives diffused radiation pattern at every frequency in W-band which proves that the proposed coherent destroyer is capable to destroy the coherence of mm-wave by generating random-phase reflection.

2. W-BAND GROUNDED FSSs

The design of W-band quasioptical filters, consisting of periodically perforated slots on metal backed Roger 4003C substrate, is considered. As shown in Figure 1, the structure consists of rectangular slots in $1.5 \mu\text{m}$, aluminum on top of $1489 \mu\text{m}$ grounded Roger 4003C substrate of dielectric constant $\epsilon_r = 3.38$, and loss tangent 0.0027 . Before metallization, a $10 \mu\text{m}$ benzo-cyclo-butene (BCB) layer was deposited between the aluminum layer and Roger 4003C to level the roughness of the Roger 4003C surface. As the thickness of the dielectric wafer Roger 4003C is in the order of the half wavelength, the structure behaves like a Fabry-Perot resonator. During the simulation, the structure can be tuned out so that the FSS geometry can be adapted to a slightly different wafer thickness, without deterioration of the device characteristics. The resonant frequency can be set properly by choosing the space between the slots (A and B in Figure 1) and the slot length “ a ” and slot width “ b .” The simulations of the structure were carried out by using commercial CST microwave studio software. Starting the simulation with initial values obtained from calculation of the approximate resonance condition, final values were determined from CST simulation results. The unit cell dimensions were optimized to the value of $A = B = 1400 \mu\text{m}$.

We considered three grounded FSSs with slot lengths of $896 \mu\text{m}$, $970 \mu\text{m}$ and $1076 \mu\text{m}$ and their slot width of $400 \mu\text{m}$ to check the slot length dependence phase variation. These values are obtained from the CST simulation. The CST simulation software performs simulation by using numerical tools of finite integral technique (FIT). In this case, the numerical method provides a universal spatial discrimination scheme, applicable to various electromagnetic problems, ranging from static field calculations to high-frequency applications in time domain. FIT is static up to the THz range. Due to the fact that a computer is only capable of calculating problems which have finite expansion, we need to specify the boundary conditions. The basic functions are calculated numerically by using the perfect boundary approximation. The perfect boundary conditions were chosen to get the tangential electric and tangential magnetic fields components uniform inside the slot but outside to zero. The electric boundary $E_t = 0$ (i.e., all tangential electric fields and normal magnetic fluxes are set to zero) was chosen in the “ y ” axis direction and the perfect magnetic boundary $H_t = 0$ (i.e., all tangential magnetic fields and normal electric fluxes are set to zero) was chosen in the “ x ” axis direction as in Figure 1.

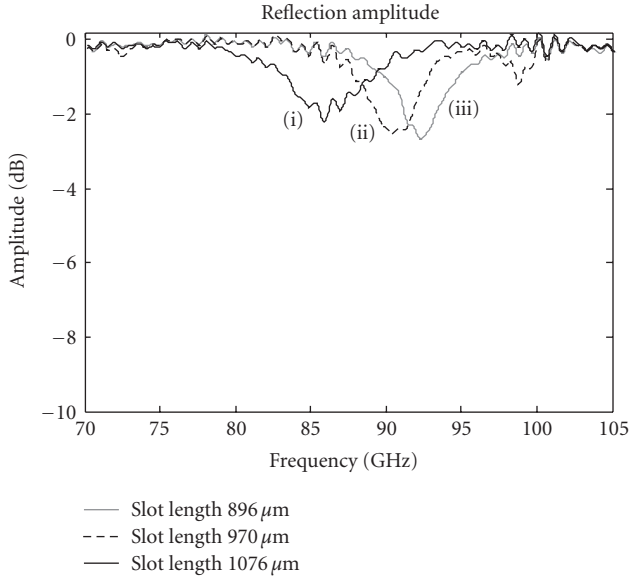


FIGURE 2: Measured reflection amplitudes of different slot length grounded FSSs. (Slot length of curve (i) 1076 μm , curve (ii) 970 μm , and curve (iii) 896 μm .)

2.1. Measurement results of FSSs

As discussed in our paper [7], the measurement amplitude and phase of a grounded FSS fit well with simulation results. To show the slot length dependence phase variation (i.e., phase delay), only the measurement amplitude and phase curves of the FSSs measured with free-space millimeter wave vector network analyzer (MVNA) are presented here. The reflection amplitudes of the three FSSs are shown in Figure 2. The minimum reflections (S_{11}) at resonant frequencies are -2.17 dB, -2.53 dB, and -2.68 dB for curves (i), (ii), and (iii), respectively, which prove that the FSSs reflect in full W-band, and the total W-band phase is useable in reflection mode. The realization of slot FSS in compare to the patch demonstrate that for FSS, the maximum transmission occurs at the resonant frequency. Therefore, there are losses at resonance since some portion of the energy is lost in the area between FSS and the ground plane. The FSS suffers higher losses at the resonance in compare to patch, but the phase variation with frequency of the FSS is more linear than patch antenna. This property is more advantageous than the higher reflection gain.

Figure 3 shows the effect of slot length variation on phase of FSSs in W-band. Near resonance, a small change of resonant slot length causes a large phase variation in the FSS phase curve. For example, in Figure 3, at 91.61 GHz, the phase values of the curves (i), (ii), and (iii) are -259.3° , -176.6° , and -79.16° , respectively. So, the phase delay between the curve (i) and curve (iii) is 180° . At 91.61 GHz, the slot length variation of $106 \mu\text{m}$ [curve (i)-(ii)] gives a phase delay 82.7 degree, and resonance slot length difference of $180 \mu\text{m}$ [(i)-(iii)] gives a phase delay of 180 degree. Figure 3 also shows that by changing the slot lengths, the phase delay and phase gradient can be controlled. We

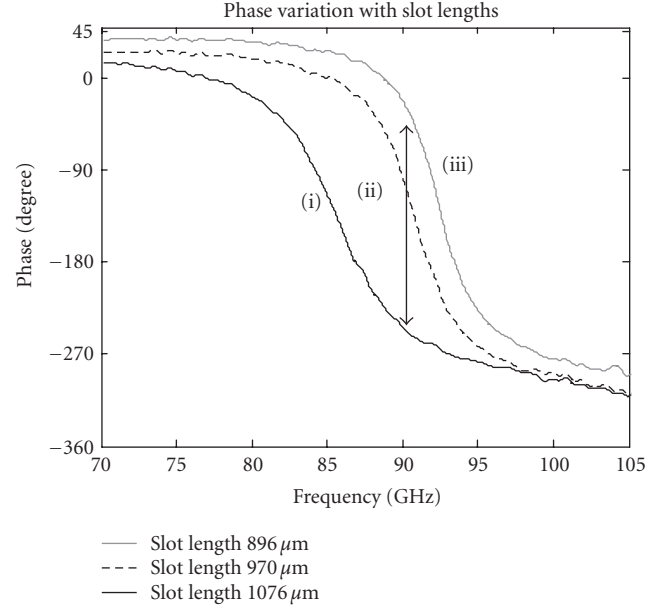


FIGURE 3: Measured phase versus frequency curves, slot lengths as variable parameter. (Slot length of curve (i) 1076 μm , curve (ii) 970 μm , and curve (iii) 896 μm .)

measured total 350° phase variation in the W-band. This value can be increased by decreasing the slot length and by introducing higher order modes.

3. DETERMINISTIC FUNCTION

Till now, we have shown how phase delay can be introduced by using FSS of different slot lengths. This investigation demonstrates that each FSS cell with unique slot length is equivalent to a delay element, and the amount of delay is determined by the slot length. As an example of deterministic function realization, mm-wave beam splitter by FSS array is consider in this section. The idea of this design is to introduce variable phase delay in constant phase of a coherent mm-wave plane wave to split the beam in two directions to observe the phase-delay effect. The schematic diagram of the beam splitter array is shown in Figure 4, where every pattern represents a different slot length. As the slot length variation is in the order of micron and is less significant in figure, schematic diagrams are presented instead of real photo arrays. The beam splitter array was designed with 20×20 cells of FSS composite of 20 different slot lengths, divided in to two subarrays as shown in Figure 4. Each pattern of Figure 4 represents unique slot length. The column wise patterns represent different slot lengths and their phase values are listed in Table 1. In the left 10×20 cells subarray, all the cells have negative phase values and in the right 10×20 cells subarray, all cells have positive phase values. The different length FSS cells were distributed column wise in such a way that from the center of the array, the phase delay will increase in both left and right sides of the array shown in Figure 4. Table 1 shows the slot lengths of FSS cells, their corresponding phase values (obtained from CST simulations at 94 GHz), and the respective phase delays. The

TABLE 1: Slot lengths, corresponding phase values, and phase delays of beam splitter. The patterns of the left most column of the table represent different columns of Figure 4.

	Phase (degree)	Slot length (μm)	Delay (degree)
	-138°	1097	-61°
	-128°	1048	-54°
	-116°	1013	-47°
	-103°	990	-40°
	-89°	972	-34°
	-75°	959	-29°
	-61°	949	-23°
	-47°	941	-17°
	-30°	931	-11°
	0°	917	0°
	32°	903	32°
	49°	895	49°
	63°	888	63°
	78°	879	78°
	91°	870	91°
	105°	858	105°
	116°	846	116°
	127°	832	127°
	138°	812	138°
	147°	785	147°

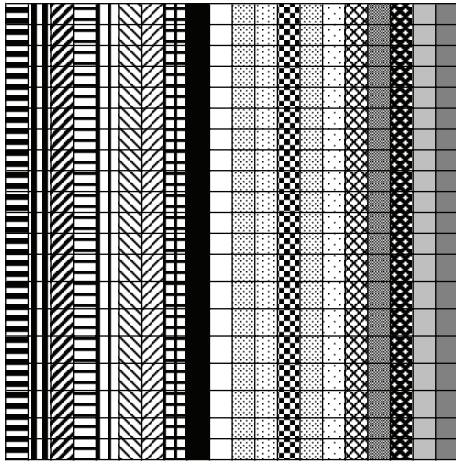


FIGURE 4: Schematic drawing of beam splitter FSS array. (Patterns follow the values listed in Table 1.)

amounts of phase delays were calculated by using the formula of geometrical optics, considering the interspacing distances of the FSS cells (i.e., distance between the centers of two successive unit cells) and for an off axis beam focal distance of 30 cm from the antenna surface. The FSS array was designed in a way that both subarrays will bend the beam and will focus 30 cm away from the antenna face. Due to left and right bending, splitted radiation will be obtained in each frequency.

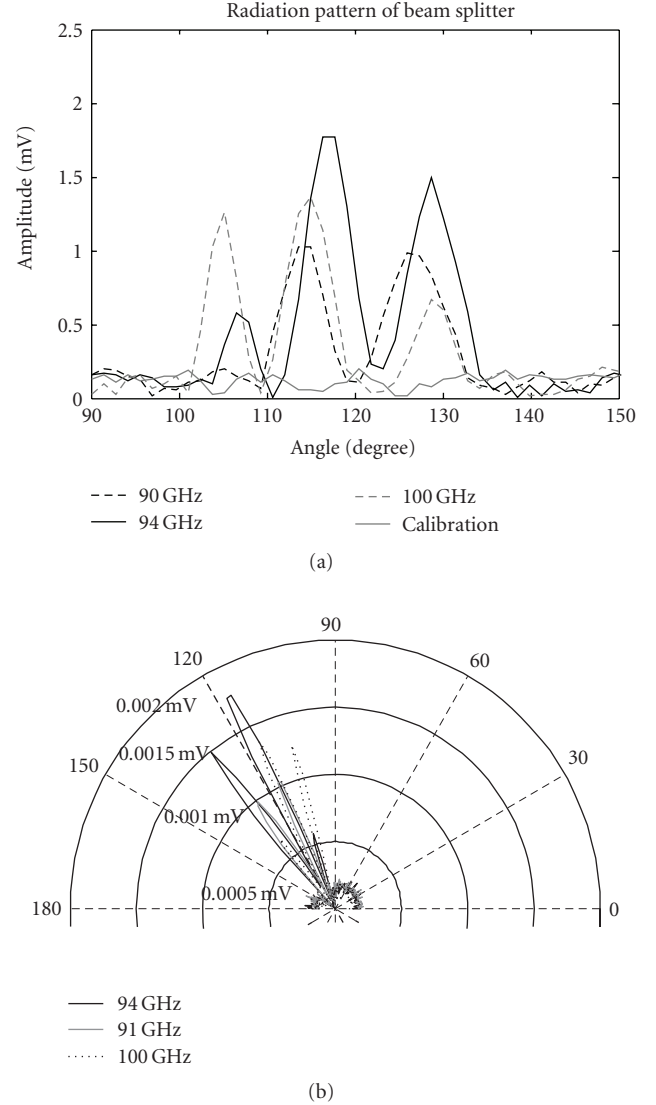


FIGURE 5: Measured near field radiation pattern of beam splitter array at different incident frequencies: (a) rectangular plot (b) polar plot.

3.1. Measurement results of beam splitter

The radiation patterns of the arrays were measured with backward-wave oscillator (BWO) in motorized setup. The measurement was carried out with 45° angular position of the antenna axis to the BWO millimeter wave source axis (in measurement Figures 5(b) and 7(b)). The antenna broad side axis was at 135°. At 94 GHz measurement, two lobes were obtained at 130° and 118° due to the phase variation of beam splitting. The measured rectangular and polar radiation patterns of the beam splitter are shown in Figures 5(a) and 5(b), respectively. In Figure 5(a), the calibration of the measurement system is shown (marked in legend). This is the radiation pattern without antenna and just with the antenna holder. A result shows a good calibration for the antenna measurement setup.

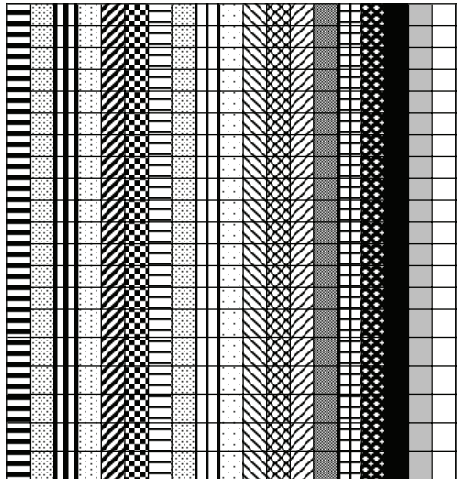


FIGURE 6: Schematic drawing of coherent destroying diffuser. (Patterns correspond to the phase values listed in Table 1.)

The measurement radiation patterns at 90 GHz, 94 GHz, and 100 GHz frequencies are presented. The results show that at each frequency, we get two main lobes on both sides of the antenna broad side axis. The position of lobes changes with frequency as the phase values of the FSS cells changes with frequency. Figure 5(b) shows the radiation patterns in polar plot. Maximum reflection for side lobes is obtained at 94 GHz. With the decreasing or increasing of measurement frequency, the side lobes reflection power decreases.

4. COHERENCE DESTROYING DIFFUSER

As explained for beam splitter in Section 3, the columnar array of FSS cells mounted on a dielectric substrate, each column represents a delay element. The delay of each column is determined by its slot length. To realize the random phase diffuser system, the columns of beam splitter FSS array of Figure 4 were reshuffled to design the diffuser array. To get random phase pattern, the columns of Figure 4 were the reshuffled as shown in Figure 6.

4.1. Measurement results of diffuser

As already mentioned, the amounts of phase delay listed in Table 1 were calculated at 94 GHz. So, the change of frequency will introduce different set of phase values at the desired frequency. Due to the random reshuffling of the FSS columns, reflection at each frequency will be diffused reflection, as the delay element of the array introduces random phases unlike focusing of beam splitter. The reflected beams are no longer coherent due to the fact that a random phase introduce from the random positioning of the FSS cells. At each frequency, the reflection is also diffused reflection. The measurement results are shown in Figure 7. The same calibration shown in Figure 5(a) was used for this measurement. For simplicity, the measurement radiation patterns are presented at 85 GHz, 90 GHz, 94 GHz, 100 GHz, 105 GHz, and 110 GHz. Figure 7(a) shows that

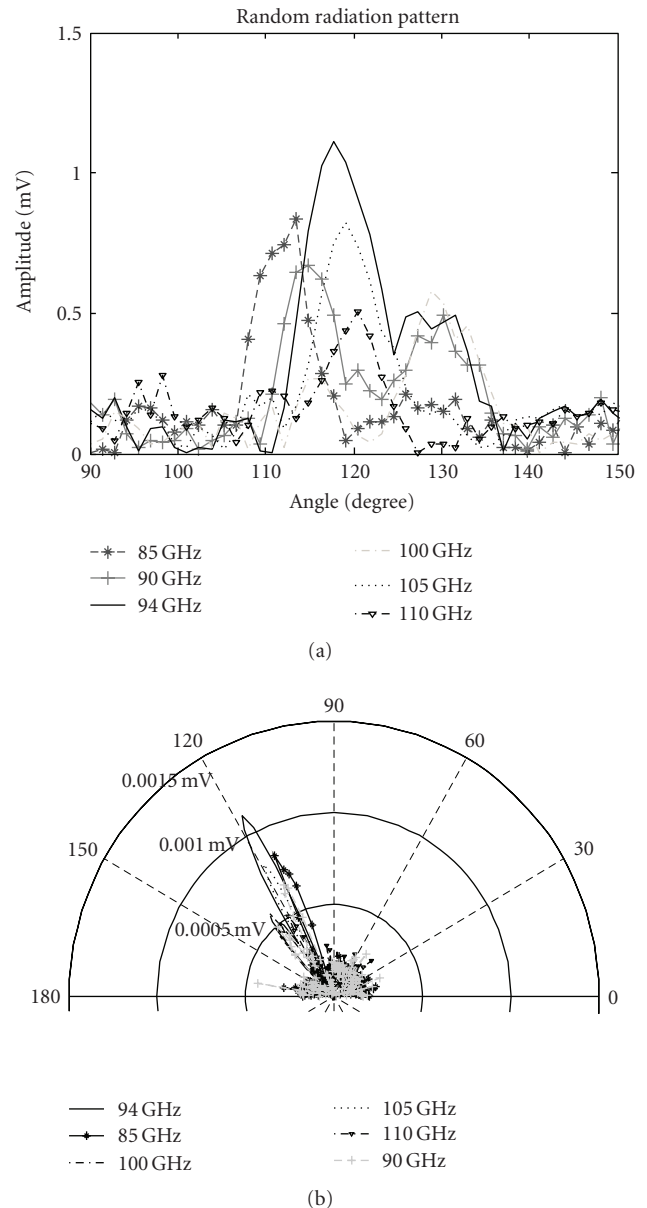


FIGURE 7: Measured near field radiation pattern of random phase diffuser: (a) rectangular plot (b) polar plot.

every measurement is different in amplitude direction than the others. The maximum reflection power obtained at 94 GHz and there is no side lobes like the beam splitter. For the sake of representation, the angular position of the detector from 90° to 150° is shown in rectangular plots of Figures 5(a) and 7(a).

5. CONCLUSION

We have designed a coherence destroying diffuser system using passive FSS array. We explained the slot length dependence phase variation properties of FSS, and also showed how phase delay can be controlled by changing slot lengths. We presented the design of mm-wave beam splitter

as deterministic function which split the coherent beam in two directions and then shown the coherent destroyer by reshuffling the cell columns of beam splitter array. This coherent destroyer can also be used as multifrequency diffuser system. In multifrequency diffuser system, at each frequency, the radiation pattern is different, and also the reflection is diffused reflection, that is, the reflected signal is incoherent. This type of reflector array is capable to destroy the coherence of the coherent mm-wave sources as the array behaves like a phase modulator which introduces random phases. In multifrequency diffuser approach, the frequency difference should be large enough, since a small difference generates quite similar speckle distributions [12, 13]. The bandwidth of the proposed diffuser is whole W-band, which gives the freedom to use enough frequency differences as multifrequency diffuser.

ACKNOWLEDGMENTS

This work was partially funded by the Vrije Universiteit Brussel (VUB-OZR), the Flemish Fund for Scientific Research (FWO- G.0041.04), and the Flemish Institute for the encouragement of innovation in science and technology (IWT-SBO 231.011114).

REFERENCES

- [1] I. Ocket, B. Nauwelaers, G. Koers, and J. Stiens, "Fast modeling and optimization of active millimeter wave imaging systems," in *Proceedings of the 36th European Microwave Conference (EuMC '06)*, pp. 1559–1562, Manchester, UK, September 2006.
- [2] I. Jaeger, J. Stiens, G. Koers, G. Poesen, and R. Vounckx, "Hadamard speckle reduction for millimeter wave imaging," *Microwave and Optical Technology Letters*, vol. 48, no. 9, pp. 1722–1725, 2006.
- [3] J. I. Trisnadi, "Speckle contrast reduction in laser projection displays," *Proc. SPIE*, vol. 4657, pp. 131–137, 2002.
- [4] S. Islam, J. Stiens, G. Poesen, I. Jäger, and R. Vounckx, "Frequency selective surface as a filter for active millimeter wave imaging," in *Proceedings of the 12th Microcol Conference*, pp. 137–140, Budapest, Hungary, May 2007.
- [5] R. Dubrovka, J. Vazquez, C. Parini, and D. Moore, "Equivalent circuit method for analysis and synthesis of frequency selective surfaces," *IEE Proceedings: Microwaves, Antennas and Propagation*, vol. 153, no. 3, pp. 213–220, 2006.
- [6] S. Biber, M. Bozzi, O. Gunther, L. Perreggrini, and L.-P. Schmidt, "Design and testing of frequency-selective surfaces on silicon substrates for submillimeter-wave applications," *IEEE Transactions on Antennas and Propagation*, vol. 54, no. 9, pp. 2638–2645, 2006.
- [7] S. Islam, J. Stiens, G. Poesen, I. Jaeger, G. Koers, and R. Vounckx, "Grounded frequency selective surfaces as W-band quasi-optical filters for active millimeter wave imaging," in *Proceedings of the Asia Pacific Microwave Conference*, vol. 3, pp. 2401–2404, Bangkok, Thailand, December 2007.
- [8] D. M. Pozar and T. A. Metzler, "Analysis of a reflect array antenna using microstrip patches of variable size," *Electronics Letters*, vol. 29, no. 8, pp. 657–658, 1993.
- [9] D. M. Pozar, S. D. Targonski, and H. D. Syrigos, "Design of millimeter wave micro-strip reflect-arrays," *IEEE Transactions on Antennas and Propagation*, vol. 45, no. 2, pp. 287–296, 1997.
- [10] J. A. Encinar, "Design of two-layer printed reflect arrays using patches of variable size," *IEEE Transactions on Antennas and Propagation*, vol. 49, no. 10, pp. 1403–1410, 2001.
- [11] N. Misran, R. Cahill, and V. F. Fusco, "Design optimisation of ring elements for broadband reflectarray antennas," *IEE Proceedings: Microwaves, Antennas and Propagation*, vol. 150, no. 6, pp. 440–444, 2003.
- [12] J. I. Trisnadi, "Hadamard speckle contrast reduction," *Optics Letters*, vol. 29, no. 1, pp. 11–13, 2004.
- [13] E. N. Grossman, A. Luukanen, and A. J. Miller, "Terahertz active direct detection imagers," in *Terahertz for Military and Security Applications II*, vol. 5411 of *Proceedings of SPIE*, pp. 68–77, Orlando, Fla, USA, April 2004.

Research Article

A New Fractal-Based Design of Stacked Integrated Transformers

Goran Stojanović, Milan Radovanović, and Vasa Radonić

Faculty of Technical Sciences, University of Novi Sad, Trg Dositeja Obradovića 6, 21000 Novi Sad, Serbia

Correspondence should be addressed to Goran Stojanović, sgoran@uns.ns.ac.yu

Received 1 December 2007; Accepted 29 February 2008

Recommended by Tibor Berceci

Silicon-based radio-frequency integrated circuits are becoming more and more competitive in wide-band frequency range. An essential component of these ICs is on-chip (integrated) transformer. It is widely used in mobile communications, microwave integrated circuits, low-noise amplifiers, active mixers, and baluns. This paper deals with the design, simulation, and analysis of novel fractal configurations of the primary and secondary coils of the integrated transformers. Integrated stacked transformers, which use fractal curves (Hilbert, Peano, and von Koch) to form the primary and secondary windings, are presented. In this way, the occupied area on the chip is lower and a number of lithographic processes are decreased. The performances of the proposed integrated transformers are investigated with electromagnetic simulations up to 20 GHz. The influence of the order of fractal curves and the width of conductive lines on the inductance and quality factor is also described.

Copyright © 2008 Goran Stojanović et al. This is an open access article distributed under the Creative Commons Attribution License, which permits unrestricted use, distribution, and reproduction in any medium, provided the original work is properly cited.

1. INTRODUCTION

Constant growth of wireless applications brought to an intensive need for mobile communications and mobile communication devices. Due to a growing need for wireless communication devices, radio frequency and wireless market is continuing its development. The integrated transformer is an essential component in many RF and microwave integrated circuits [1–8]. Although significant efforts have been made in order to improve the characteristics of integrated transformers [9–12], it is still a great problem to bring in piece the opposite demands for low cost, low supply voltage, and low power dissipation, but small occupied area and high frequency of operation in RF implementation of these transformers. Commonly used transformers are fabricated on lossy silicon substrate; hence they are from the start limited to a lower quality factor, coupling coefficient and high parasitic effects between the component and the substrate. Arbitrary transformer layouts also impact the transformer characteristics. Various transformers layouts including parallel winding, interwound winding, overlay winding, and concentric spiral winding were presented in [13]. Planar transformers generally have

lower self-inductance, parasitic capacitances, and coupling factor, but higher resonant frequency comparing with the stacked transformers, which engage less chip area and have higher inductance values and lower quality factor [14]. The width of conductive lines (usually have the square spiral shape), spacing between coils, and material used for their fabrication also have influence on overlay characteristics of the transformer. However, papers that present other layout geometries (apart from square spiral) of the primary and secondary coils are very rare.

The unique property of fractal curves is that, after an infinite number of iterations, their length becomes infinite although the entire curve fits into the finite area. This space-filling property can be exploited for the miniaturization of the integrated transformers. Due to the technology limitations such as a minimal line width and spacing achievable by the fabrication process and because of its degree of complexity, the ideal fractal cannot be built. Our research is limited to prefractals with a low degree of iteration (or low order). In this work, we present novel layouts of the primary and secondary windings in the shape of fractal curves and demonstrate a comprehensive analysis of the shape and order fractal curves influence on the inductance and quality factor

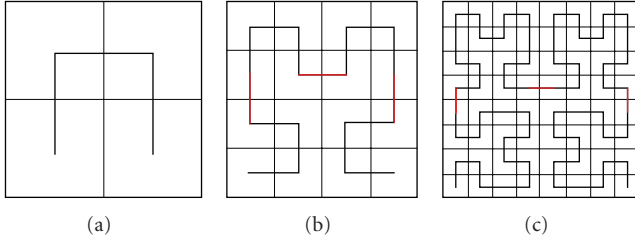


FIGURE 1: Hilbert curve (iteration 1, iteration 2, and iteration 3).

of the stacked transformers for RFICs applications. The simulation has been generated using the Microwave Office software package [15].

2. A BRIEF OVERVIEW OF USED FRACTAL CURVES

Fractals are a whole new set of geometrical objects featuring two main common properties: self-similarity and fractional dimension. There are many mathematical structures that are fractals; for example, Sierpinski's gasket, Peano curve, von Koch's snowflake, the Mandelbrot set, the Hilbert curve, and so forth [16–18]. In this paper, Hilbert curve, Peano curve, and von Koch curve have been used. The space-filling properties of these curves make them attractive candidates for use in the design of the primary and secondary windings of integrated fractal transformers.

Hilbert curve

Hilbert curves are built through an iterative procedure that generates almost self-similar structures. In addition, Hilbert curves are space-filling curves, meaning that in the limit the fractal curve fills the whole space. The capability to pack conductive lines in a small space following a Hilbert curve is very appealing for manufacturing windings of on-chip transformers. The first three steps in the construction of the Hilbert curve are shown in Figure 1.

Peano curve

The original Peano curve is a base-motif fractal that uses a line segment for the base and the motif depicted in Figure 2(a). To generate the Peano curve, it is necessary to start with a line segment and substitute it with the motif. After that, every one of the 9 line segments in the figure is taken and substituted with the motif again. At the end, a square is obtained as it is illustrated in Figure 2(c). In the motif, there are 9 identical line segments and the size of each is $1/3$ of the original line segment.

Koch curve

Koch curve is a fractal curve characterized by such properties as a curve that is infinitely long, contained within a finite region, and not differentiable at any point (they just have corners). A geometric construction scheme for the Koch curve is shown in Figure 3.

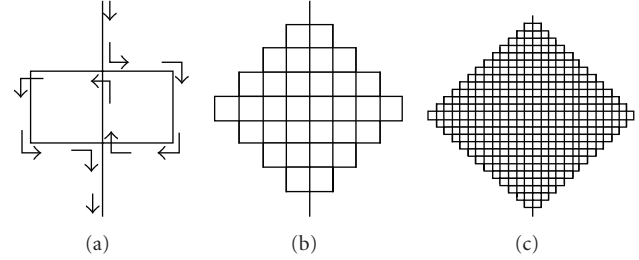


FIGURE 2: Peano curve (iteration 1, iteration 2, and iteration 3).

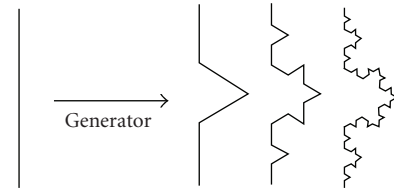


FIGURE 3: A geometrical construction of standard Koch curves.

3. DESIGN OF FRACTAL INTEGRATED TRANSFORMERS

Implementations and design of monolithic transformers consist of different trade-offs, which need to be considered in the geometry of the transformer layout. The inductance is determined by the primary or secondary windings (coils) lateral dimensions. Parasitic capacitances and resistances are determined by both lateral and vertical dimensions. Conventional configurations include interleaved and stacked transformer, with the spiral geometry of coils. These configurations offer varying trade-offs among self-inductance, mutual coupling coefficient, Q -factor, resonant frequency, and occupied area. For example, interleaved transformers (with square spiral shape) offer higher resonant frequency and medium coupling, whereas the stacked transformers offer high coupling and self-inductance but also high parasitic capacitances.

We have designed novel configurations of on-chip stacked transformers, where the primary and secondary windings have shapes of different fractal curves. Figure 4(a) depicts a schematic symbol and Figure 4(b) shows a stacked transformer model for simulation in the electromagnetic simulator Microwave Office. The main features of the transformers under study were assumed as follows. The silicon substrate was used with the thickness of $500\ \mu\text{m}$ and the resistivity of $10\ \Omega\cdot\text{cm}$ (Figure 4(c)). The thickness of metal layers for the primary and secondary coils is $1\ \mu\text{m}$. The oxide thickness between the silicon substrate and a metal layer for the secondary coil is $3\ \mu\text{m}$ and between metal layers for the secondary (a lower layer) and the primary (an upper layer) coils is $1\ \mu\text{m}$. Aluminum is used as a conductive material with conductivity $\sigma = 3.53 \cdot 10^7\ \text{S/m}$. As the secondary winding is closer to the substrate, it is expected that its losses would be higher than those in the primary winding and therefore quality factor of the secondary coil would be lower than for primary coil. It is important to note

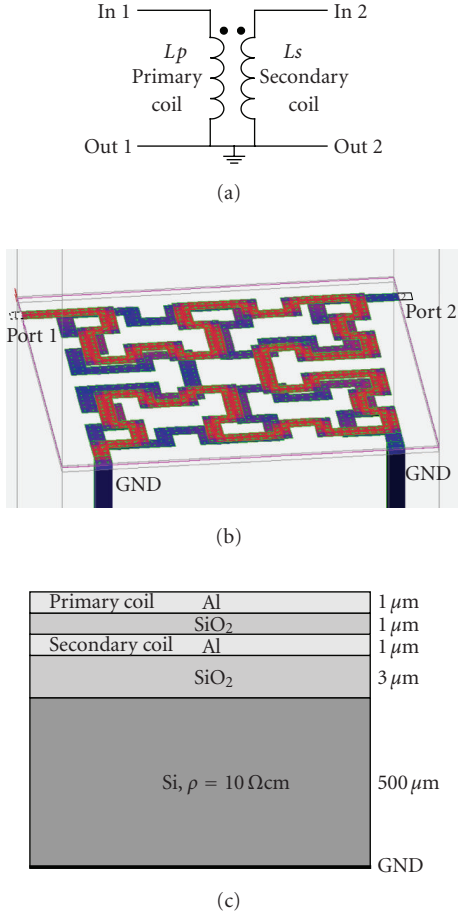


FIGURE 4: A stacked fractal transformer: (a) schematic symbol, (b) 3D model, and (c) the cross-section.

that the whole primary (and also secondary) coil occupies only one metal layer in contrast to all spiral realizations, which required more metal layers for underpass or overpass.

A stacked transformer depicted in Figure 4(b), where the primary and secondary coils have the shape of 3rd-order Hilbert curve, has turn ratio 1 : 1. Port 1 and port 2 are input ports for the primary and secondary coils, respectively, whereas the other terminals are grounded.

The losses in the conductive segments are taken into account through two parameters, which are presented in Figure 5. The low frequency parameter (R_{dc}) specifies the DC resistance of the planar conductor (in ohms/square). The DC resistance is the resistance of the conductor assuming a uniform current distribution in the cross-section of the conductor. The high frequency loss coefficient (R_{hf}) specifies the loss associated with the conductor at frequencies, where the thickness of the conductor is significantly thicker than the skin depth. Since the loss associated with the skin depth effects are proportional to the square root of frequency, the skin depth loss coefficient is multiplied by the square root of frequency to provide an ohms/square value that is used for loss computations. At low frequencies, the DC resistance is used in the computation of conductor loss, while at high frequencies the high frequency loss coefficient

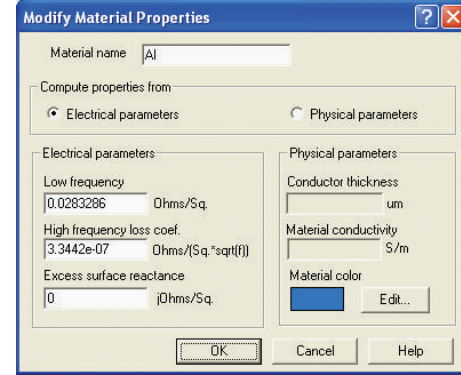


FIGURE 5: The electrical parameters of conductive material (Al) including high frequency loss coefficient.

is used to compute conductor loss. In the transition region (frequencies where the skin depth is close to the thickness of the conductor) both factors are used. In this paper, typical values of these parameters have been $R_{dc} = 0.02832$ and $R_{hf} = 3.34 \cdot 10^{-7}$, according to the metal thickness and conductivity, for the aluminum conductive layer.

4. RESULTS AND DISCUSSION

The layout topology of the windings of the integrated transformers strongly depends on the application of the transformer. In this paper, the stacked configuration of monolithic transformer is analyzed. Stacked transformer, or vertical coupling structure, represents a multiple conductor layer structure. This configuration has the advantage of area efficiency and higher mutual coupling between the windings due to placing the primary coil on top of the secondary. Stacked transformers mainly have high coupling factor (k -factor), up to 0.9, and high mutual inductance. The primary and the secondary windings are placed in adjacent metal layers causing different distances from the substrate. In order to improve its characteristics, the windings are placed in slightly offset position (horizontally or diagonally shifted), resulting in lower parasitic capacitance and consequently higher Q -factor and resonant frequency.

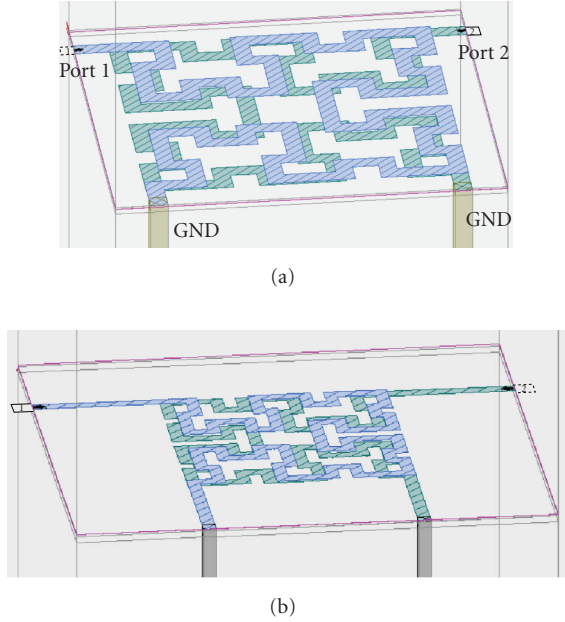
4.1. Transformer windings in the form of Hilbert curves

In this subsection, we investigate behavior of transformer parameters with variations of the Hilbert curves iteration and the width of conductive segments of the primary and secondary parts of the transformer.

In the first example, the primary and secondary windings are made in the form of Hilbert curve of the third order ($N = 3$). The width of the conductive lines for the primary and secondary windings (w_p and w_s) are $10 \mu\text{m}$ and after that $6 \mu\text{m}$ at overall occupied area $336 \mu\text{m} \times 336 \mu\text{m}$. Figure 6 shows a 3D view of these transformers. The performances of the proposed transformers were determined using EMSight, the EM simulator in Microwave Office. Figure 7 illustrates

TABLE 1: The performance comparison of different transformer realizations.

Ref.	Configuration	L_p [nH]	Q_p	SRF [GHz]
[11]	Differential square spiral transformer	0.8	5.2 peak @ 5 GHz	10
[12]	Interleaved 3 turn square spiral transformer	5.32	5.77 peak @ 2.95 GHz	6.2
[13]	Interleaved square spiral transformer	8.5	NA	4.9
[14]	Differential square spiral transformer	5.5	10 peak @ 1.7 GHz	NA
This work	Stacked transformer, Hilbert $N = 3$, $w = 10 \mu\text{m}$	0.6	5.95 peak @ 8.4 GHz	18.8

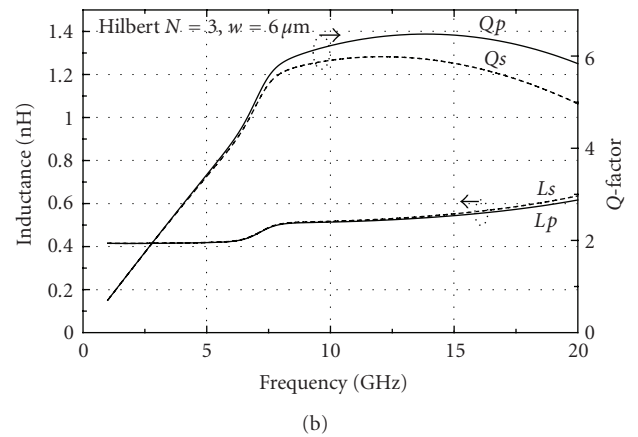
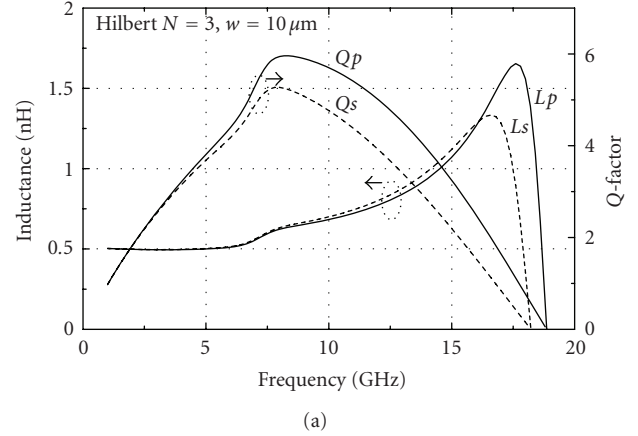
FIGURE 6: A monolithic stacked transformer realized with two 3rd-order Hilbert curve, (a) $w_p = w_s = 10 \mu\text{m}$, (b) $w_p = w_s = 6 \mu\text{m}$.

the inductance and Q -factor of transformer structures as a function of frequency.

From Figure 7 it can be seen that the inductances of the primary and secondary coils are approximately the same (ratio 1 : 1) in the wide frequency range. For the same order of fractal curves, greater values of the quality factor can be obtained for a smaller width of the metal trace. Figure 7 shows that a wider metal strip has a lower peak Q and resonant frequency, although it has a higher Q at low frequencies. This can be explained by the fact that wider metal traces lead to larger parasitic capacitances between coils and substrate, and consequently lower Q -factor and self-resonant frequency.

In the next simulation the order of fractal curve is increased. The primary and secondary winding are realized using 4th-order of Hilbert curve ($N = 4$) as can be seen in Figure 8. Technological parameters were the same as in the previous example.

The simulation results for the inductance and quality factor as a function of frequency are depicted in Figure 9, for the widths of metal strip of $10 \mu\text{m}$ and $6 \mu\text{m}$, respectively.

FIGURE 7: The inductance and quality factor as a function of frequency for stacked transformer, (a) 3rd-order Hilbert curve, $w_p = w_s = 10 \mu\text{m}$, (b) 3rd-order Hilbert curve, $w_p = w_s = 6 \mu\text{m}$.

It can be seen that the stacked Hilbert transformer with fractal curves of the 4th order achieves only the inductance improvement (due to longer total conductive lines), but Q -factor and self-resonant frequency are smaller comparing to the 3rd-order curves with the same widths of the primary and secondary coils.

The proposed Hilbert transformer with $w = 6 \mu\text{m}$ exhibited a simulated L_p around 1.3 nH at 3 GHz, which is approximately 25% lower than that of a Hilbert structure with $w = 10 \mu\text{m}$. However, the transformer with $w = 6 \mu\text{m}$ has higher values of the quality factor. This means that higher

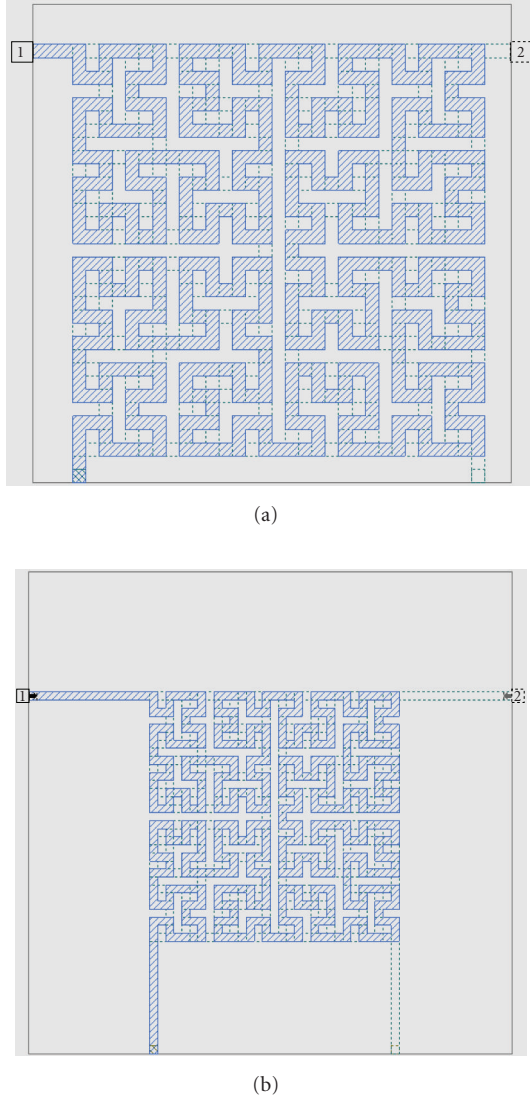


FIGURE 8: A top view of fractal transformers realized with two Hilbert curves $N = 4$, (a) $w_p = w_s = 10 \mu\text{m}$, (b) $w_p = w_s = 6 \mu\text{m}$.

Q value of a Hilbert transformer structures is mainly due to lower series resistance (and parasitic capacitance).

To conclude this subsection, it is important to point out that a good Q_p around 6, and Q_s around 5.3 (Figure 7(a)) were achieved at 8.4 GHz, respectively. This is better than results for differential or interleaved transformer with square spiral in open literature [11, 12]. Note that there is, also, a significant increase in the self-resonant frequency (SRF). The simulation results show that using Hilbert fractal layouts for the primary and secondary windings of stacked transformers, similar or better performances can be achieved comparing to the published results for monolithic transformers, as listed in Table 1.

This improving performance is evident regarding increasing SRF and Q -factor, whereas the inductance values are reasonably smaller due to higher value of the negative

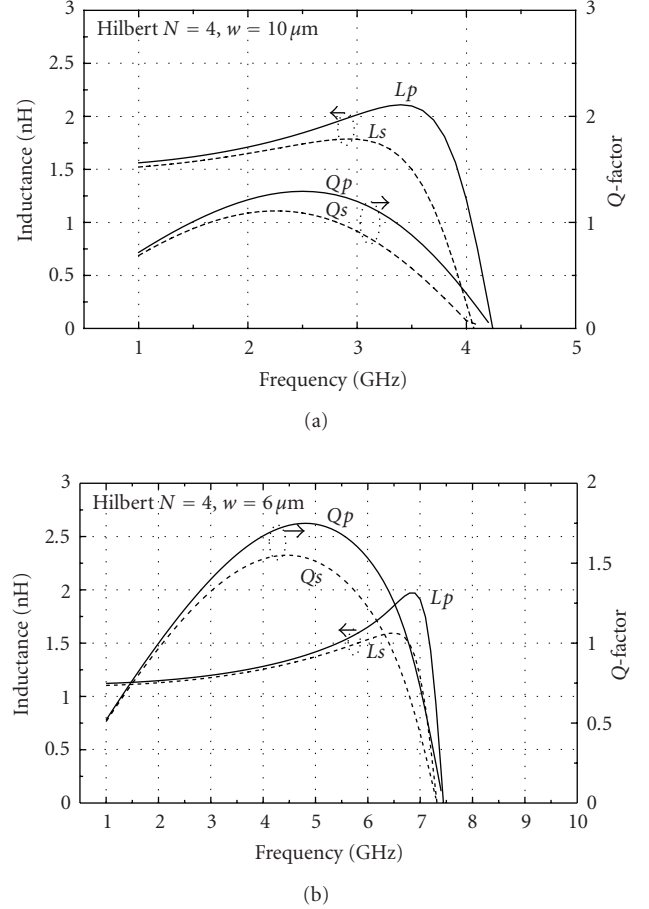


FIGURE 9: Frequency characteristics of the inductance and quality factor of integrated stacked transformer realized with 4th order of Hilbert curve (a) $w_p = w_s = 10 \mu\text{m}$, (b) $w_p = w_s = 6 \mu\text{m}$.

mutual inductance between segments of a conductive strip with the shape of Hilbert fractal curve.

4.2. The primary and secondary windings in the form of von Koch curves

In this subsection, the Koch fractal curves of the third and fourth order are used for realization of the primary and secondary windings of the stacked transformers. The geometrical and technological parameters are the same as in the earlier simulations. In the first realization, the primary and secondary coils are designed of three serially connected 3rd-order Koch curves with the width of conductive (aluminum) lines $w_p = w_s = 10 \mu\text{m}$ and after that $w_p = w_s = 6 \mu\text{m}$. To compare results for this fractal curves and Hilbert ones, the overall area is the same as in the previous cases. The 3D and the top view of the primary and secondary windings are depicted in Figure 10, for $w_p = w_s = 10 \mu\text{m}$. In order to minimize the parasitic capacitance between the primary and the secondary coils of transformers, the secondary coil is rotated with the respect to the primary ones for an angle of 90 degrees.

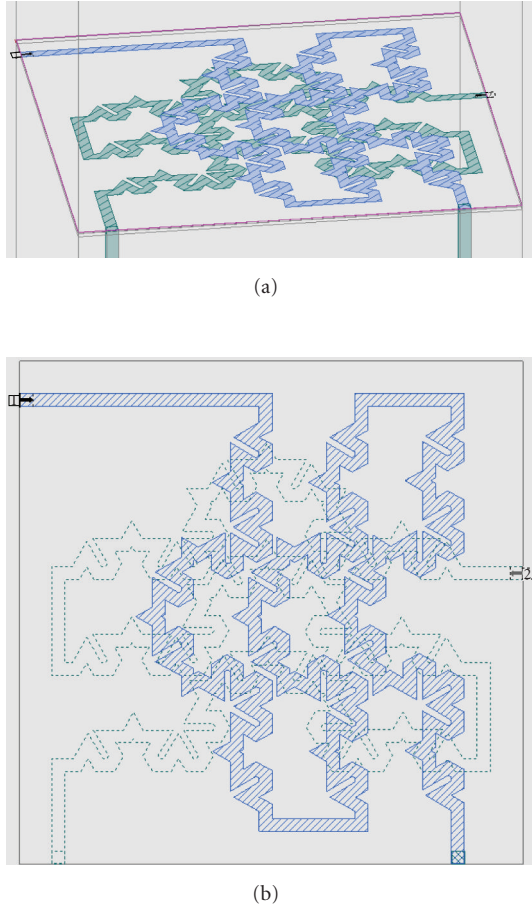


FIGURE 10: A Koch fractal transformer, (a) 3D view (b) the top view.

In Figure 11, dependence of the primary and secondary inductances and corresponding quality factors are shown as a function of frequency for $w_p = w_s = 10 \mu\text{m}$ (Figure 11(a)) and for $w_p = w_s = 6 \mu\text{m}$ (Figure 11(b)).

Although the primary and the secondary are designed to have the same shape and the width of conductive lines, obtained values of their inductance and corresponding values of quality factor are slightly different due to the existence of the back-side metallization. The current induced in the metallization layer lowers the inductance values in both transformer structures, since it flows in the opposite direction than the current in windings. The inductance of the secondary winding is more affected because it is placed closer to the metallization. It can be observed that with an increase of frequency, Q -factor grows initially and reaches its maximal value. At higher frequencies, substrate losses and the ac resistance of conductive lines increases faster than the inductive reactance, which results in a decrease of the quality factor appears. The higher self-resonant frequency is obtained for the transformer with the smaller line width due to the low parasitic capacitances between windings and metallization plane and therefore this structure can be used in the widest frequency range.

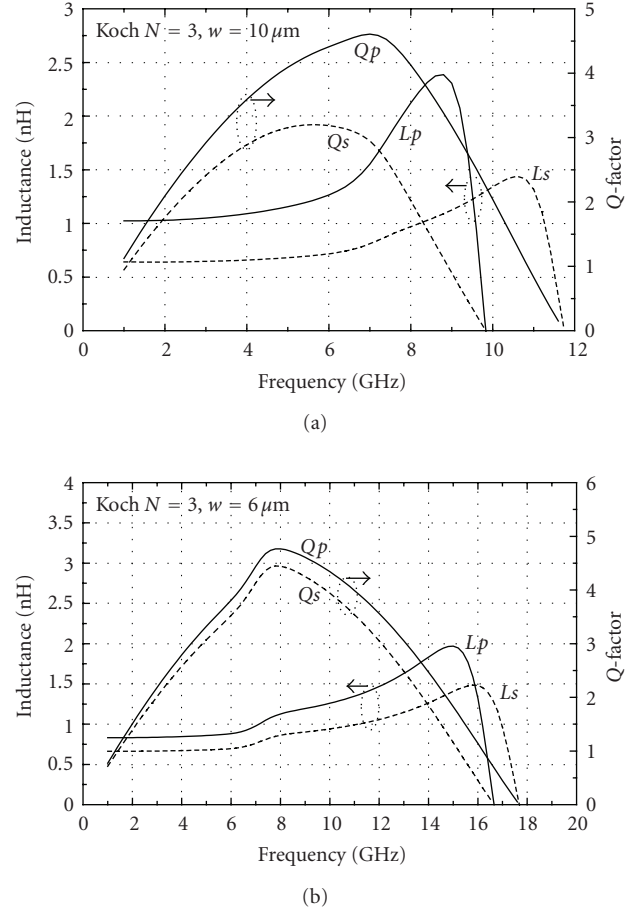


FIGURE 11: Dependence of Q -factor and inductance as a function of frequency for transformer with (a) $w_p = w_s = 10 \mu\text{m}$, (b) $w_p = w_s = 6 \mu\text{m}$.

4.3. The primary and secondary windings in the form of Peano curves

The Peano fractal curves of the second order are also used for realization of the primary and secondary coils of integrated stacked transformer. The layout of the transformer is shown in Figure 12 (3D view in Figure 12(a) and the top view in Figure 12(b)) with $w_p = w_s = 6 \mu\text{m}$. As can be seen, the primary and secondary winding are slightly shifted with the aim of the minimization of the parasitic capacitance between the coils.

The simulation results for the inductance and quality factor are presented in Figures 13(a) and 13(b). Figure 13(a) shows the obtained values of Q -factors for the primary coil (Q_p) and the secondary coil (Q_s), and for corresponding inductances with $w_p = w_s = 10 \mu\text{m}$, whereas Figure 13(b) shows these results for the structure with $w_p = w_s = 6 \mu\text{m}$. In this case, better values of the quality factor were obtained for the structure with $w_p = w_s = 10 \mu\text{m}$ ($Q_p = 4.7$, and $Q_s = 3.4$ at 7.5 GHz). The higher Q_p and Q_s for this structure are attributed to a larger distance between neighboring segments (greater step) that means lower overall capacitance between the primary (and secondary) coil and the silicon substrate.

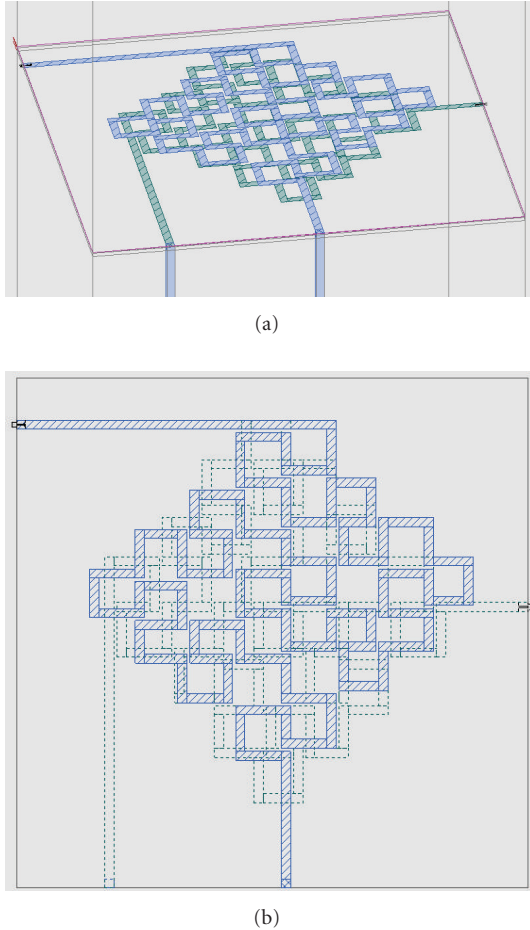
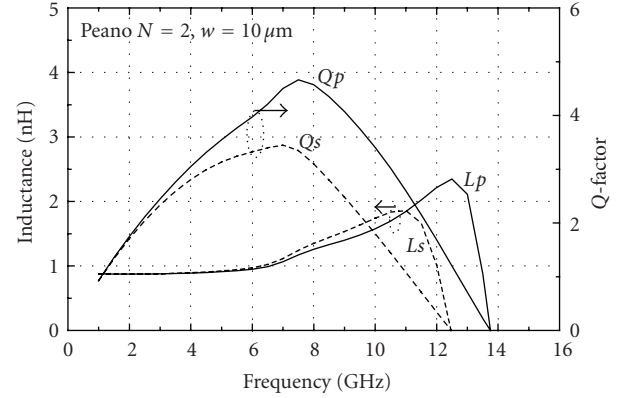


FIGURE 12: The Peano ($N = 2$) fractal transformer: (a) 3D view, (b) the top view.

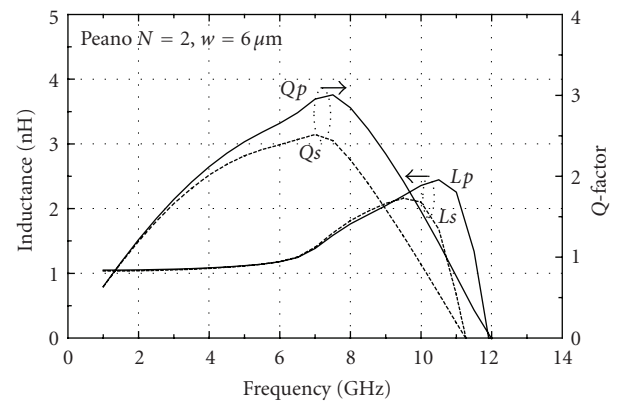
Comparing proposed integrated transformers it can be concluded that the configuration with 3rd-order Hilbert curve has a maximal value of the Q -factor and self-resonant frequency, afterwards realizations with Koch and Peano curves. The minimal Q -factor has the stacked transformer with 4th-order Hilbert curve thanks to the largest occupied area and as a result the biggest parasitic capacitance value. As can be seen from Figure 7(b), the best Q_p around 6.8, and Q_s around 5.9 were achieved at approximately 12 GHz. It is important to emphasize that by comparison with published results there is also a significant increase in self-resonant frequency in the presented transformer structures.

5. CONCLUSION

The integrated transformer characteristics and performances greatly depend on geometrical and process parameters. In this paper, the novel fractal stacked transformers were analyzed using full-wave EM simulations and compared in terms of the inductance and quality factor. Simulation results show that using fractal layouts for the primary and secondary windings, similar or better performances can be achieved in comparison with earlier published results for monolithic



(a)



(b)

FIGURE 13: Q -factor and inductance versus frequency for Peano transformer with (a) $w_p = w_s = 10 \mu\text{m}$, (b) $w_p = w_s = 6 \mu\text{m}$.

transformers with square spiral geometry. The presented results mean that transformer configurations with fractal curves can be very useful for RF-IC designers to design high-performance RF and microwave integrated circuits.

REFERENCES

- [1] Y. K. Koutsoyannopoulos and Y. Papananos, "Systematic analysis and modeling of integrated inductors and transformers in RF IC design," *IEEE Transactions on Circuits and Systems II*, vol. 47, no. 8, pp. 699–713, 2000.
- [2] Y.-S. Choi, J.-B. Yoon, B.-I. Kim, and E. Yoon, "A high-performance MEMS transformer for silicon RF ICs," in *Proceedings of the 15th IEEE International Conference on Micro Electro Mechanical Systems (MEMS '02)*, pp. 653–656, Las Vegas, Nev, USA, January 2002.
- [3] J. Y. Park and J. U. Bu, "Packaging compatible microtransformers on a silicon substrate," *IEEE Transactions on Advanced Packaging*, vol. 26, no. 2, pp. 160–164, 2003.
- [4] J. Y. Park, Y. J. Chang, and J. U. Bu, "Monolithically integrated 3D micro-inductors and micro-transformers for RF applications," in *Proceedings of the 8th International Symposium on Advanced Packaging Materials (ISAPM '02)*, pp. 362–363, Stone Mountain, Ga, USA, March 2002.

- [5] Y. J. Yoon, Y. Lu, R. C. Frye, and P. R. Smith, "Modeling of monolithic RF spiral transmission-line balun," *IEEE Transactions on Microwave Theory and Techniques*, vol. 49, no. 2, pp. 393–395, 2001.
- [6] H. Y. D. Yang and J. A. Castaneda, "Design and analysis of on-chip symmetric parallel-plate coupled-line balun for silicon RF integrated circuits," in *Proceedings of IEEE Radio Frequency Integrated Circuits Symposium (RFIC '03)*, pp. 527–530, Philadelphia, Pa, USA, June 2003.
- [7] A. M. Niknejad and R. G. Meyer, "Analysis, design, and optimization of spiral inductors and transformers for Si RF ICs," *IEEE Journal of Solid-State Circuits*, vol. 33, no. 10, pp. 1470–1481, 1998.
- [8] A. H. Aly and B. Elsharawy, "Modeling and measurements of novel high k monolithic transformers," in *Proceedings of IEEE MTT-S International Microwave Symposium*, vol. 2, pp. 1247–1250, Philadelphia, Pa, USA, June 2003.
- [9] A. Zolfaghari, A. Chan, and B. Razavi, "Stacked inductors and transformers in CMOS technology," *IEEE Journal of Solid-State Circuits*, vol. 36, no. 4, pp. 620–628, 2001.
- [10] K. T. Ng, B. Rejaei, and J. N. Burghartz, "Substrate effects in monolithic RF transformers on silicon," *IEEE Transactions on Microwave Theory and Techniques*, vol. 50, no. 1, pp. 377–383, 2002.
- [11] O. El Gharniti, E. Kerhervé, J.-B. Bégueret, and P. Jarry, "Modeling of integrated monolithic transformers for silicon RF IC," in *Proceedings of the 11th IEEE International Conference on Electronics, Circuits and Systems (ICECS '04)*, pp. 137–140, Tel Aviv, Israel, December 2004.
- [12] J. Jaehning, D. R. Allee, E.-B. El-Sharawy, T. L. Alford, N. Yazdi, and D. J. Allstot, "Monolithic transformers in a five metal CMOS process," in *Proceedings of IEEE International Symposium on Circuits and Systems (ISCAS '02)*, vol. 2, pp. 807–810, Phoenix, Ariz, USA, May 2002.
- [13] J. R. Long, "Monolithic transformers for silicon RF IC design," *IEEE Journal of Solid-State Circuits*, vol. 35, no. 9, pp. 1368–1382, 2000.
- [14] M. Straayer, J. Cabanillas, and G. M. Rebeiz, "A low-noise transformer-based 1.7 GHz CMOS VCO," in *Proceedings of IEEE International Solid-State Circuits Conference (ISSCC '02)*, vol. 1, pp. 286–287, San Francisco, Calif, USA, February 2002.
- [15] Microwave Office 2001, Applied Wave Research, Inc.
- [16] H. O. Peitgen, H. Jürgens, and D. Saupe, *Chaos and Fractals: New Frontiers of Science*, Springer, New York, NY, USA, 1992.
- [17] P. Emp, S. Joan, and S. C. del Vallès, *Fractal Miniaturization in RF and Microwave Networks*, Fractus, Barcelona, Spain, 2001.
- [18] Fractalcoms final report, Project no. IST-2001-33055, <http://www.tsc.upc.es/fractalcoms/>.

Research Article

High Efficiency and Broadband Microstrip Leaky-Wave Antenna

Onofrio Losito

Department of Innovation Engineering, University of Lecce, Via per Monteroni, 73100 Lecce, Italy

Correspondence should be addressed to Onofrio Losito, onofrio.losito@unile.it

Received 1 December 2007; Accepted 8 May 2008

Recommended by T. Kalkur

A novel layout of leaky-wave antennas based on tapered design has been proposed and investigated. The new tapered leaky-wave antenna (LWA) was designed running a simple procedure which uses an FDTD code, and using a suitable metal walls down the centerline along the length of the antenna connecting the conductor strip and the ground plane, which allows to use only half of the structure, the adoption of a simple feeding, and the reduction of sidelobes. The good performance of this new tapered microstrip LWA, with reference to conventional uniform microstrip LWAs, is mainly the wider band of 33% for VSWR < 2, higher gain (12 dBi), and higher efficiency (up to 85%). Furthermore, from the theoretical analysis we can see that, decreasing the relative dielectric constant of the substrate, the bandwidth of the leaky-wave antenna becomes much wider, improving its performance.

Copyright © 2008 Onofrio Losito. This is an open access article distributed under the Creative Commons Attribution License, which permits unrestricted use, distribution, and reproduction in any medium, provided the original work is properly cited.

1. INTRODUCTION

Progress in the recent years has been obtained on the development of leaky-wave antennas based on the higher order mode of microstrip [1, 2]. The LWAs possess the advantages of low-profile, easy matching, fabrication simplicity, and frequency/electrically scanning capability. But in some application especially for point-to-point communication, the main beam variation of LWA should be as low as possible. A tapered steps microstrip LWA, in which each step can irradiate in subsequent ranges of frequency, is a possible solution to obtain a fixed mainbeam LWA [3]. Unfortunately, in this antenna the impedance mismatch between subsequent steps reduces the bandwidth, furthermore the excitation of higher order mode without dominant mode perturbation requires more elaborate feeding scheme. A curved design of tapered antennas with a physical grounding structure along the length of the antenna allows to reduce the impedance mismatch, suppressing the dominant mode (bound mode). This solution improves the band the gain, the efficiency, and simplifies its feeding. Moreover, due to the image theory it is possible to design only half antenna with the same property of entire, reducing the dimensions of the uniform microstrip LWA. The performance of the efficiency and

band of this LWA can be improved further, if we use a substrate with relative dielectric constant that approached 1.

In this paper, we have proposed such new curve tapered LWA as discussed in the following section.

2. DESIGN OF MICROSTRIP CURVE LWA

We can explain the character of microstrip LWAs through the solution of the dispersion characteristic equation obtained with full-wave analysis methods. This solution allows to evaluate the radiation region of leaky-wave through the complex propagation constant $k = \beta - j\alpha$, where β is the phase constant of the first higher mode, and α is the leakage constant. The complexity of full wave analysis [4, 5] to solve the propagation characteristics suggests to use an easy FDTD algorithm which use a PML boundary condition, as proposed in [6], to obtain the normalized phase constant and attenuation constant. The leakage radiate phenomena, from the propagation characteristics, can only be noted above the cutoff frequency of higher order mode, and below the frequency such that, the phase constant is equal at the free space wave number.

From these characteristics of curves we know the frequency range of the leaky-mode radiation, that can be



FIGURE 1: Layout of multisection LWA.



(a)



(b)

FIGURE 2: (a) Layout of curve tapered LWA Type II. (b) Cross-section of LWA Type II with a physical grounding structure along the length of the antenna which connects the conductor strip and the ground plane.

indicated in the more useful way for the design of our antenna [3]:

$$\frac{c}{2w_{\text{eff}}\sqrt{\epsilon_r}} = f_c < f < \frac{f_c\sqrt{\epsilon_r}}{\sqrt{\epsilon_r - 1}}. \quad (1)$$

From (1) we can see that as the width of the antenna decreases, the cutoff frequency increases shift toward high frequency. This behavior allows to design a multisection microstrip LWA according [3] superimposing different sections in which each section can radiate in a different and subsequence to frequency range, obtaining a broadband antennas. In this way, each section should be into bound region, radiation region, or reactive region, permitting the power, to uniformly radiated at different frequencies. Moreover, we note from (1) that using a substrate material with relative dielectric constant which approached 1, the leaky-wave antenna bandwidth become much wider and increased drastically. Unfortunately, this multisection LWA (layout Type I in Figure 1(a)) shows ripples in return loss curve, spurious sidelobes, and impedance mismatch. Our idea to reduce ripples and sidelobes is to design a smooth contour antenna using the same contour of the cutoff phase constant or attenuation constant curve ($\alpha_c = \beta_c$). This curve was obtained varying the frequency for different width and length of each microstrip section, as mentioned in [7], employing the equation

$$\beta_c = c_1 f^2 + c_2 f + c_3. \quad (2)$$

This equation is given by linear polynomials interpolation of the cutoff point of the dispersion characteristic, where $c_1 = 0.13$, $c_2 = 5.4$, $c_3 = -10.41$. Further reduction of ripples and spurious sidelobes can be obtained using a suitable metal

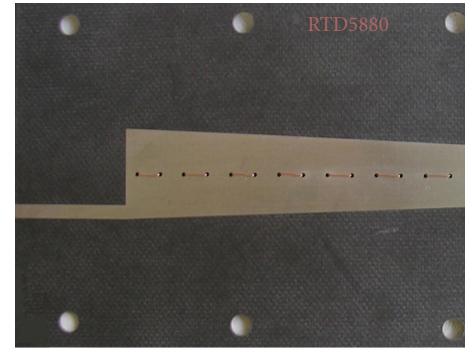


(a)

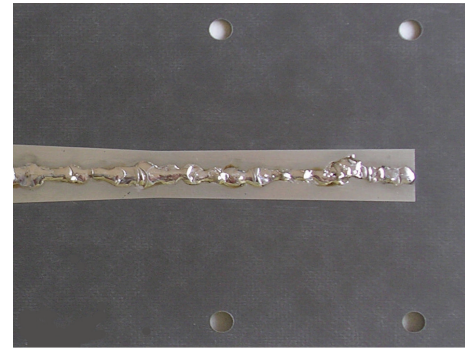


(b)

FIGURE 3: (a) Layout of half tapered LWA. (b) Cross-section of half LWA.



(a)



(b)

FIGURE 4: (a) A prototype of tapered LWA with wires in the holes. (b) The soldering made in the centerline of the antenna to cover the wires in the holes.

walls down the centreline connecting the conductor strip and the ground plane that allows the adoption of a simple feeding planar line (layout Type II in Figure 2).

This physical grounding structure suppresses the fundamental mode, forcing the energy to propagate in the next higher mode. As mentioned previously, it is possible to design only half of the entire curve tapered LWA. The half curve tapered LWA is characterized by the same property of the entire, but with the dimensions reduced of the 20% from the entire tapered LWA and reduced of the 60% from the uniform microstrip LWA. The antenna layout Type III (half curve tapered LWA) shown in Figure 3 was optimized through a 3D electromagnetic simulator (CST Microwave



FIGURE 5: A prototype of half curve tapered leaky-wave antenna..

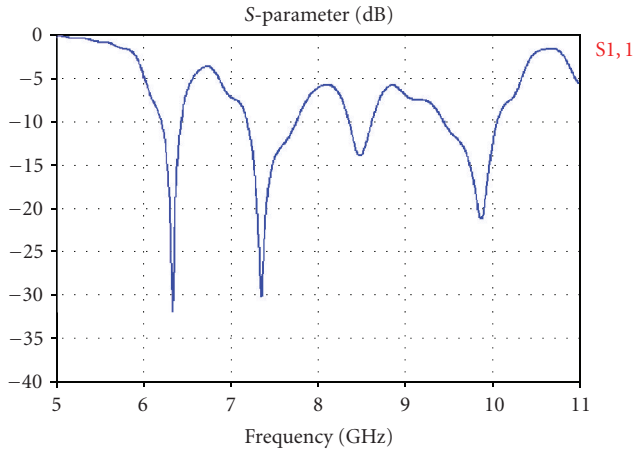


FIGURE 6: Simulated return loss of multisecton LWA Type I.

Studio), and the return loss, the radiation pattern, and antenna efficiency were compared with the multisecton LWA (Type I) and with curve tapered LWA (Type II). A prototype of tapered LWA was designed and fabricated on RT/Duroid 5880 substrate, with $\epsilon_r = 2.32$ and a thickness of 0.787 mm. The length of the LWA was chosen to be 120 mm, to allow 90% radiation at an upper frequency of 9.5 GHz, with a 15 mm start width, and 8.9 mm of final width. A sequence of covered wires was inserted in the holes made in the centerline of the antenna to obtain a simple physical grounding structure along all the length of antenna (see Figure 4).

Moreover, a prototype of half tapered LWA was designed and fabricated with the same substrate mentioned previously, applying an adhesive conductor at the edge centerline, to connect the conductor strip and the ground plane, along all the length of antenna (see Figure 5).

This layout, therefore, improves the band, (33% for $VSWR < 2$), the gain (12 dBi), and the efficiency (up to 85%) with reference to the conventional uniform microstrip LWAs [8] (which have band of 22% for $VSWR < 2$, peak gain up to 10 dBi, and efficiency up to 75%).

3. THEORETICAL AND EXPERIMENTAL RESULTS

To excite the higher-order mode TE₁₀ in our LWA is necessary simply by an asymmetrical planar feedline of 50Ω . In fact, the physical grounding structure along the centreline of the LWA allows to suppress the dominant mode excited in the antenna. The multisecton tapered antenna Type I was made as an open circuit, with a 15 mm start width and 8.9 mm of final width designed using for-section calculation according to [3], while the smooth contour of the LWA Type II was designed through (2). As said previously, the

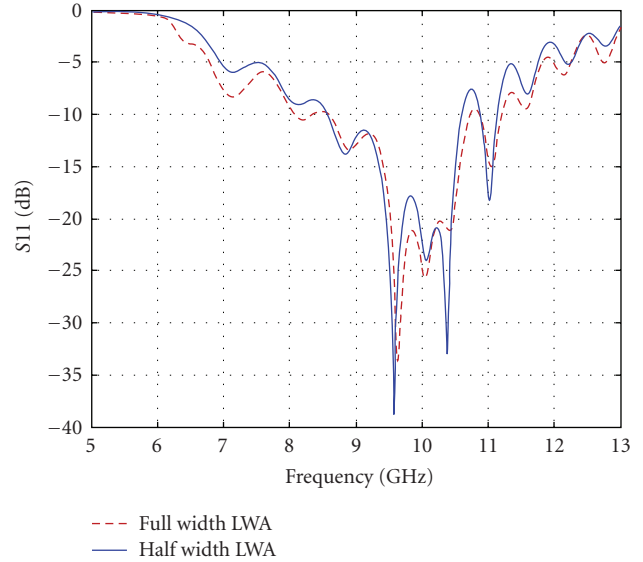
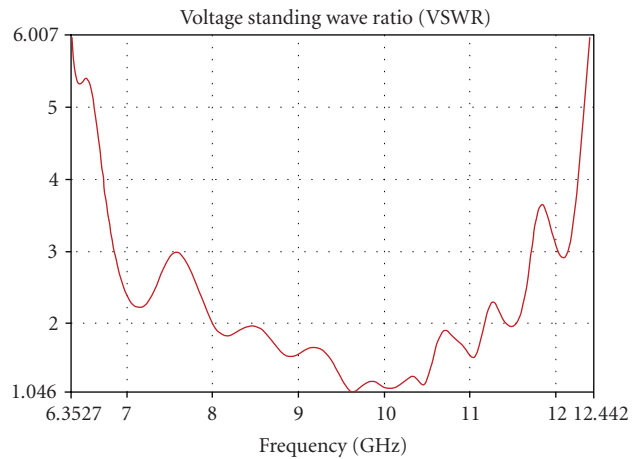
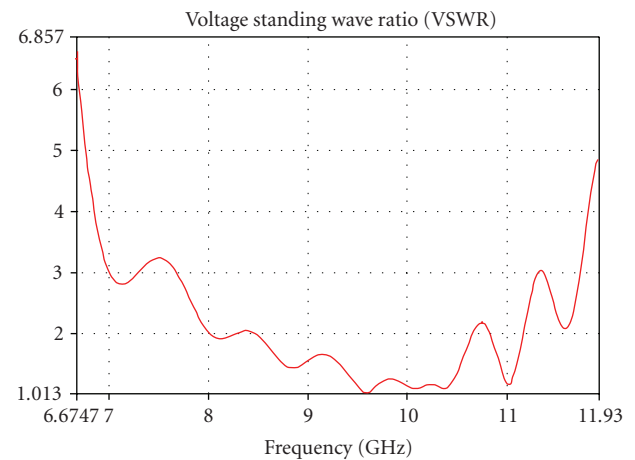


FIGURE 7: Simulated return loss (S11) of tapered LWA (Type II) and half tapered LWA (Type III) obtained by 3D electromagnetic simulator.



(a)



(b)

FIGURE 8: (a) Simulated VSWR of LWA Type II. (b) Simulated VSWR of LWA Type III.

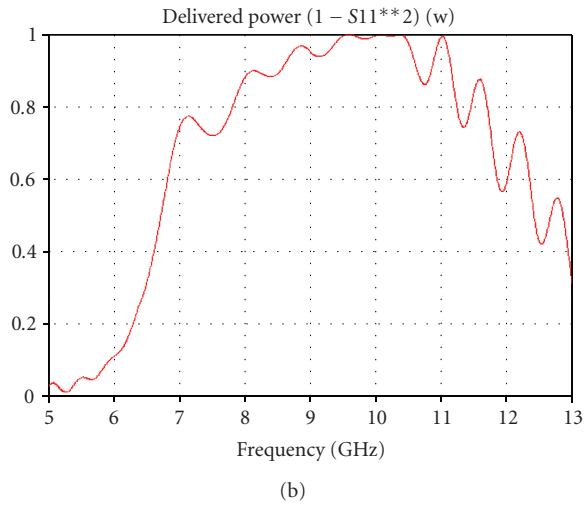
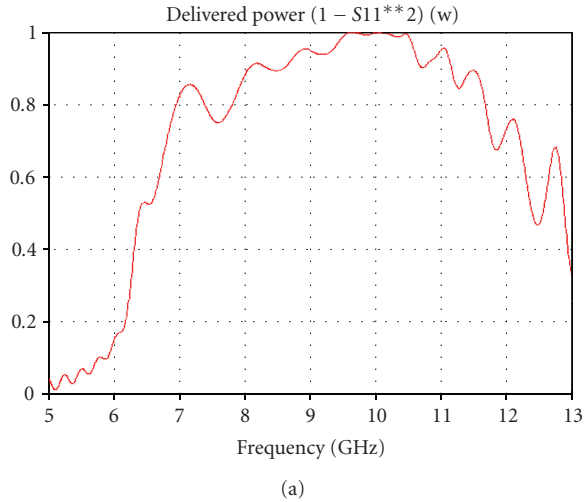


FIGURE 9: (a) Simulated efficiency LWA Type II. (b) Simulated efficiency LWA Type III.

antenna Type III was obtained using only half of transversal dimension of antenna Type II, and both (Type II and Type III) were made as an open-circuit LWA like Type I. We have implemented the simulations using a substrate of thickness of 0.787 mm and relative dielectric constant of 2.32. From the return loss (S_{11}) of Type I, we note that it is below -10 dB only in three short-range frequencies (see Figure 6), while S_{11} of Type II and Type III is practically the same, below -10 dB from 8 to 11.2 GHz as shown in Figure 7. Moreover, the VSWR of LWAs Type II and Type III ($VSWR < 2$ between 8.01 and 11.17 GHz) are in agreement like the antenna efficiency (about 85% in the same range frequency) as shown in Figures 8(a)-8(b) and Figures 9(a)-9(b). The main lobe pattern of LWAs Type I and Type III at 9.5 GHz is shown in Figures 10 and 11. From these figures, we can see a reduction of sidelobe, the peak of gain of LWA Type III up to 12 dBi, and only few degree of mainlobe variation between Type I to Type III. The results of the measured return loss of half LWA (Type III) and the measured E-field pattern

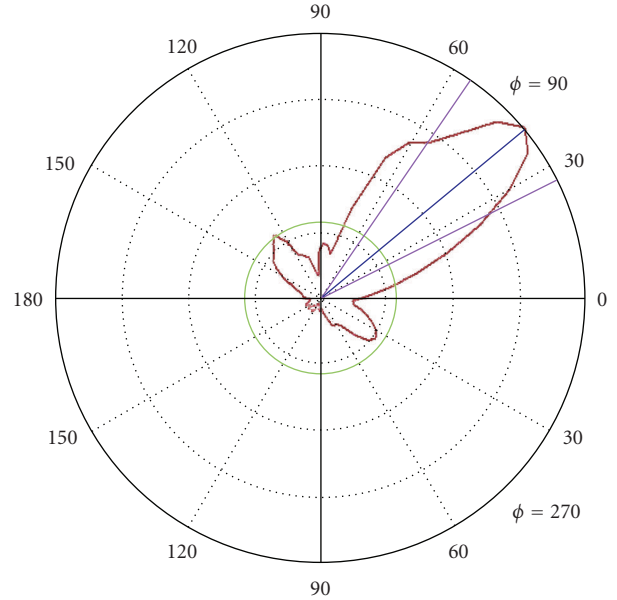


FIGURE 10: Radiation patterns of electric field (H plane) LWA Type III, at 9.5 GHz.

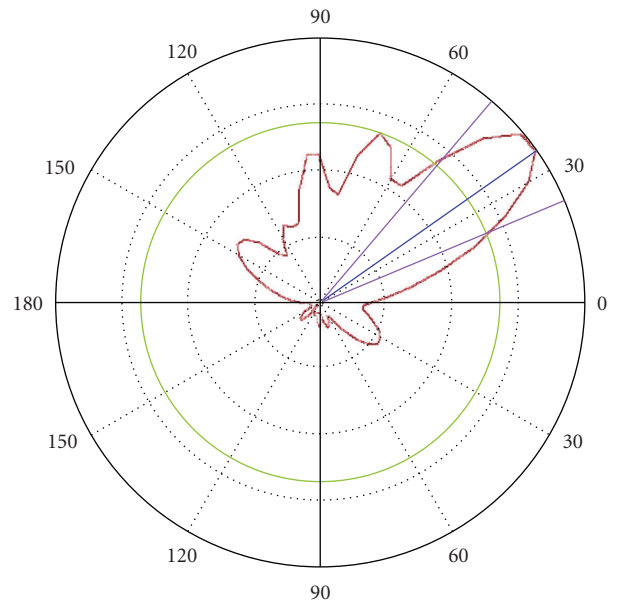


FIGURE 11: Radiation patterns of electric field (H plane) LWA Type I, at 9.5 GHz.

(at 8 GHz) of the half LWA (Type III), compared to the simulated return loss and the simulated E-field pattern (at 8 GHz) plotted in Figures 12 and 13, show a good agreement.

These results indicate a high performance of antenna Type III (33% for $VSWR < 2$, high antenna efficiency, and high power gain) compared with uniform LWAs (20% for $VSWR < 2$, peak power gain up to 10 dBi) as mentioned in [8]. Nevertheless, this performance was obtained reducing up to 60% the uniform antenna's dimensions.

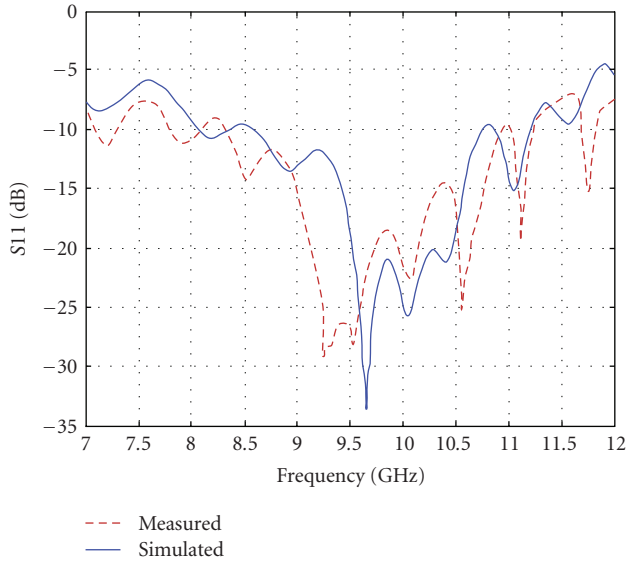


FIGURE 12: The measured and simulated return loss of half tapered LWA.

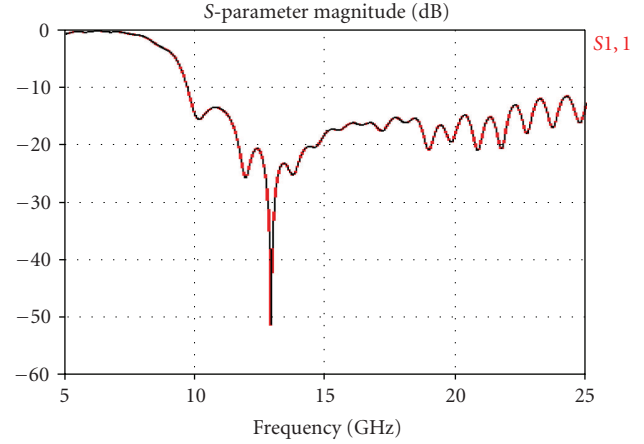


FIGURE 14: Simulated return loss LWA type III with relative dielectric constant 1.1.

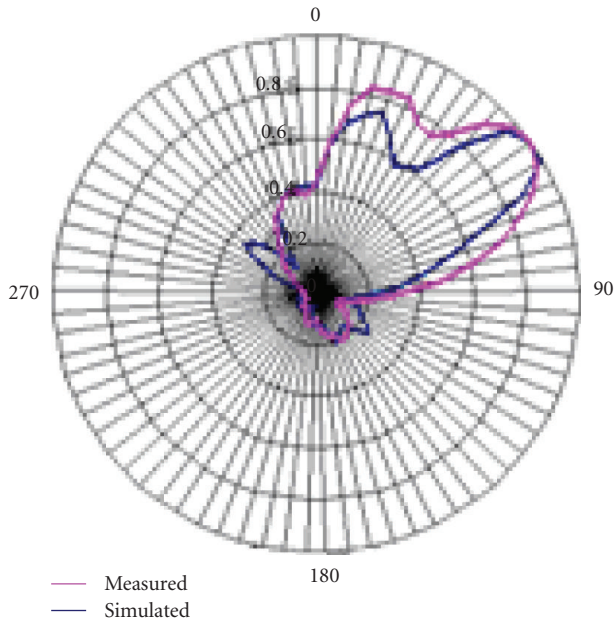


FIGURE 13: The measured and simulated radiation patterns of E field of half tapered LWA (at 8 GHz).

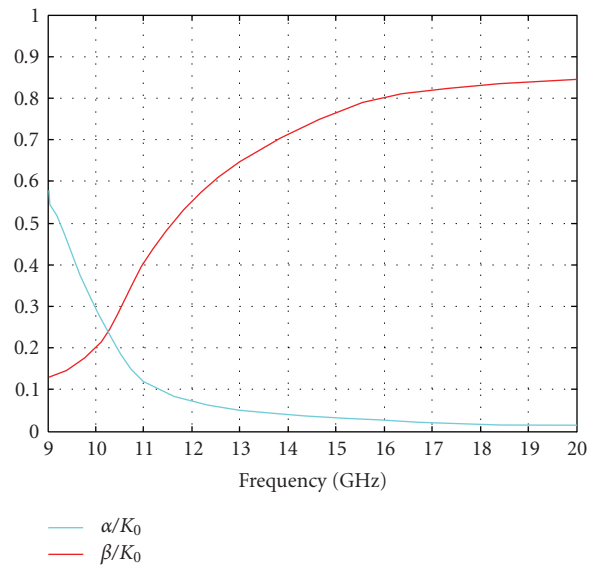


FIGURE 15: FDTD dispersion characteristics of LWA Type III first high mode with relative dielectric constant 1.1 and width 12 mm.

Finally, from (1) we note also that if the relative dielectric constant approaches 1, the cutoff frequency shifts toward high frequency and the upper limit of radiation region frequency becomes infinite, increasing drastically the bandwidth of LWA, as we can see from the simulation return loss of antenna Type III obtained with a ϵ_r 1.1 shown in Figure 14. Moreover, from the dispersion equation solved with FDTD for ϵ_r 1.1 and for an average width of antenna Type III (12mm) we note (see Figure 15) flat values of β near 0.8 and flat values of α near 0. This produces a low variation

of mainlobe angle ($\vartheta = \cos^{-1}(\beta/K_0)$) for a wide range of high frequency and a narrow shape of the same mainlobe.

4. CONCLUSIONS

In this study, a new design of broadband microstrip leaky-wave antenna from 8 to 11 GHz was proposed with high added value. An FDTD code was used to determinate the propagation constant of LWA, which was necessary for designing a smooth contour of LWA, obtained from the

interpolation of the cutoff phase constant or attenuation constant curve calculated by varying the frequency of a multisection broadband microstrip LWA. The simulations and the measured results, of this curve tapered microstrip leaky-wave antenna with a physical grounding structure along its length, demonstrate the good performance compared to conventional uniform microstrip LWAs (wider band and higher gain). This performance improves when ϵ_r approaches 1 and indicates that this structure is attractive for the design of high-performance microstrip leaky-wave antennas for microwave and millimeter wave applications.

REFERENCES

- [1] W. Menzel, "A new traveling-wave antenna in microstrip," *Archiv für Elektronik und Übertragungstechnik*, vol. 33, no. 4, pp. 137–140, 1979.
- [2] A. A. Oliner, "Leakage from higher modes on microstrip line with application to antennas," *Radio Science*, vol. 22, no. 6, pp. 907–912, 1987.
- [3] W. Hong, T.-L. Chen, C.-Y. Chang, J.-W. Sheen, and Y.-D. Lin, "Broadband tapered microstrip leaky-wave antenna," *IEEE Transactions on Antennas and Propagation*, vol. 51, no. 8, pp. 1922–1928, 2003.
- [4] T. Itoh and R. Mittra, "Spectral-domain approach for calculating the dispersion characteristics of microstrip lines," *IEEE Transactions on Microwave Theory and Techniques*, vol. 21, no. 7, pp. 496–499, 1973.
- [5] E. Kuester, R. Johnk, and D. Chang, "The thin-substrate approximation for reflection from the end of a slab-loaded parallel-plate waveguide with application to microstrip patch antennas," *IEEE Transactions on Antennas and Propagation*, vol. 30, no. 5, pp. 910–917, 1982.
- [6] G. M. Zelinski, M. L. Hastriter, M. J. Havrilla, J. S. Radcliffe, A. J. Terzuoli, and G. A. Thiele, "FDTD analysis of a new leaky traveling wave antenna," in *Proceedings of the IEEE/ACES International Conference on Wireless Communications and Applied Computational Electromagnetics*, pp. 152–155, Honolulu, Hawaii, USA, April 2005.
- [7] O. Losito, "A new design of broadband microstrip leaky-wave antenna," in *Proceedings of the 23rd Annual Review of Progress in Applied Computational Electromagnetics (ACES '07)*, Verona, Italy, March 2007.
- [8] Y. Qian, B. C. C. Chang, T. Itoh, K. C. Chen, and C. K. C. Tzuang, "High efficiency and broadband excitation of leaky mode in microstrip structures," in *Proceedings of IEEE MTT-S International Microwave Symposium Digest (MWSYM '99)*, vol. 4, pp. 1419–1422, Anaheim, Calif, USA, June 1999.

Research Article

Material Parameter Measurements for Microwave Antireflection Coating Development

Lajos Nagy

Department of Broadband Infocommunications and Electromagnetic Theory, Budapest University of Technology and Economics, Goldmann György tér 3, 1111 Budapest, Hungary

Correspondence should be addressed to Lajos Nagy, nagy@mht.bme.hu

Received 3 December 2007; Accepted 17 March 2008

Recommended by Tibor Berceli

The main steps for characterization and measurement of microwave absorbent materials in the 1–10 GHz range are introduced. The coaxial reflection-transmission type of material parameter measurement is analyzed in detail and the main measurement error is corrected. The microscopic material parameter measurement concept is also presented using different mixing rule laws to determine the material parameters of the single particles from the macroscopic parameters. Two-dimensional FDTD simulations have been used to model the behavior of mixed electric and magnetic type of material.

Copyright © 2008 Lajos Nagy. This is an open access article distributed under the Creative Commons Attribution License, which permits unrestricted use, distribution, and reproduction in any medium, provided the original work is properly cited.

1. INTRODUCTION

Antireflection coatings are widely used for optical and high-frequency applications such as microwave absorbing materials for electromagnetic compatibility or decreasing RCS for stealth applications. Even though a single-layer coating may be sufficient to obtain low reflection coefficients, its efficiency is usually reduced to a narrow bandwidth and to a specific polarization and incidence angle.

In order to extend the performance of antireflection coatings to wider ranges of frequency and incidence, a multilayered structure has to be considered.

The optimization of such complex architectures may consist in measurement of macroscopic and microscopic material parameters. This article presents a new calibration flow graph analysis and analytical equation to evaluate the correcting terms. Measurement and simulated results are presented to validate the calibration proposed and to correct the sample size deviation [1].

2. MEASUREMENTS

2.1. Macroscopic material parameter measurements

The material samples are placed in a coaxial line and two complex parameters are measured, the reflection and the transmission coefficients.

The widely used measurement method of macroscopic material parameters is based on the Nicolson and Ross system. A sample of material which has complex relative permittivity ϵ_R and permeability μ_R fills a coaxial waveguide section, as shown in Figure 1. TEM electromagnetic wave is propagated along the coaxial line with the material sample and the scattering parameters (S_{11} and S_{12}) are measured using reference planes on the two faces of the sample. The closed form equations derived by Nicolson and Ross are the following:

$$\begin{aligned}V_1 &= S_{21} + S_{11}, \\V_2 &= S_{21} - S_{11}, \\ \Gamma &= \frac{1 - V_1 V_2}{V_1 - V_2} \pm \sqrt{\left(\frac{1 - V_1 V_2}{V_1 - V_2}\right)^2 - 1}, \\ c_1 &= \left(\frac{1 + \Gamma}{1 - \Gamma}\right)^2, \\ c_2 &= -\left[\frac{c}{\omega d} \ln\left(\frac{1 - V_1 \Gamma}{V_1 - \Gamma}\right)\right]^2,\end{aligned}\tag{1}$$

from which the electrical and magnetic material parameters follows:

$$\begin{aligned}\mu_R &= \sqrt{c_1 c_2}, \\ \epsilon_R &= \sqrt{\frac{c_1}{c_2}}.\end{aligned}\tag{2}$$

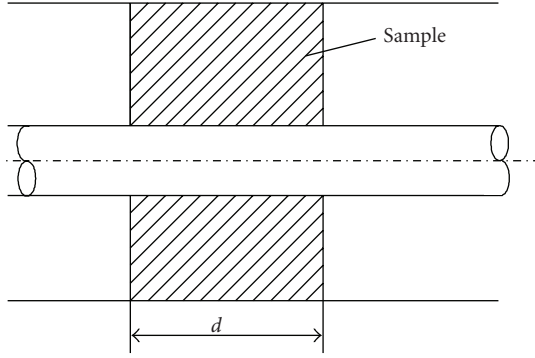


FIGURE 1: Coaxial line with annular disk of material.

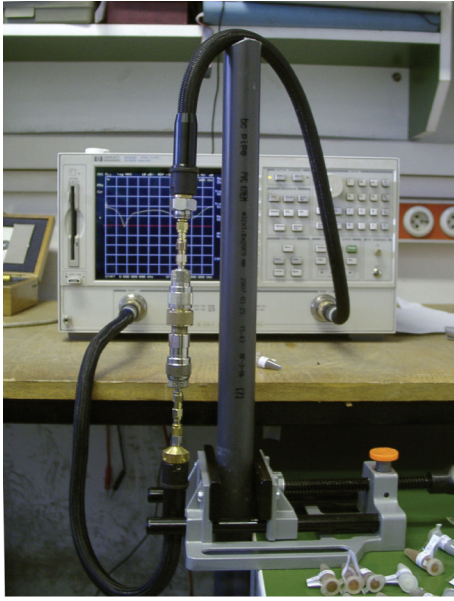


FIGURE 2: Measurement setup.

The sample holder used with the support of teflon beads and the removable connector is shown in Figure 4.

Figure 4 shows the signal flow graph for the measurement system with connectors and the sample holder in the middle. The S^a and S^b represent the reflections and transmissions of the connectors and joints, but not including the sample holder itself which is an air-filled coaxial line in empty stage and has S^o scattering matrix. The resulting S-matrix is S^e .

The S^a and S^b only differ in terms of S_{12} and S_{21} ; this leads to the length difference of the two conductors inside the support beads and connectors:

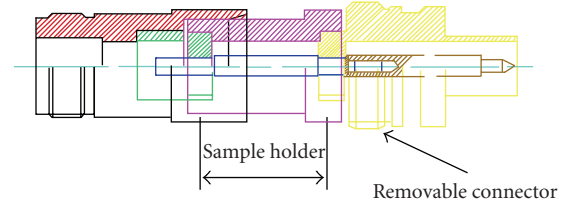
$$\begin{aligned} S_{11}^a &= S_{11}^b, \\ S_{22}^a &= S_{22}^b. \end{aligned} \quad (3)$$

The sample holder is assumed to be symmetric, reciprocal, lossless, and nonreflecting; therefore,

$$\begin{aligned} S_{12}^o &= S_{21}^o = e^{-jkd}, \\ S_{11}^o &= S_{22}^o = 0. \end{aligned} \quad (4)$$



(a)



(b)

FIGURE 3: Coaxial line sample holder.

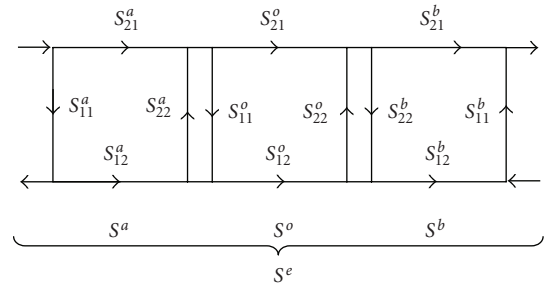


FIGURE 4: Signal flow graph of sample holder.

The resulting S-matrix S^e and S^a , and S^b is assumed to be reciprocal; therefore,

$$\begin{aligned} S_{12}^a &= S_{21}^a, \\ S_{12}^b &= S_{21}^b, \\ S_{12}^e &= S_{21}^e. \end{aligned} \quad (5)$$

The sample holder has a removable connector only on one side, therefore, directly only S^a can be measured using a short load at various positions in the air-filled sample holder.

There are 4 unknowns in (3)–(5) which can be determined by using 4 measurements, from which there are two reflection measurements for S^a using short load at two different positions and there is the measurement of S^e .

The calibration measurements result in the following four equations:

$$\begin{aligned} \Gamma_{m1} &= S_{11}^a - S_{21}^a \cdot S_{12}^a \frac{1}{1 + S_{22}^a}, \\ \Gamma_{m2} &= S_{11}^a - S_{21}^a \cdot e^{-j2kl} \cdot S_{12}^a \frac{1}{1 + S_{22}^a \cdot e^{-j2kl}}, \end{aligned} \quad (6)$$

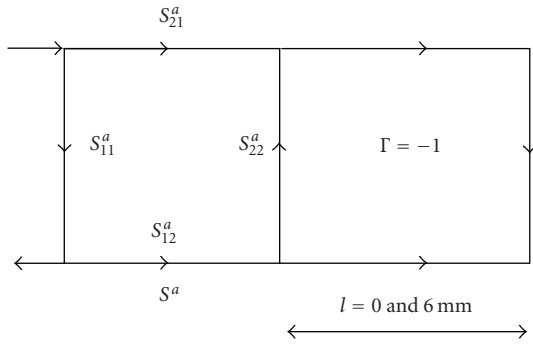
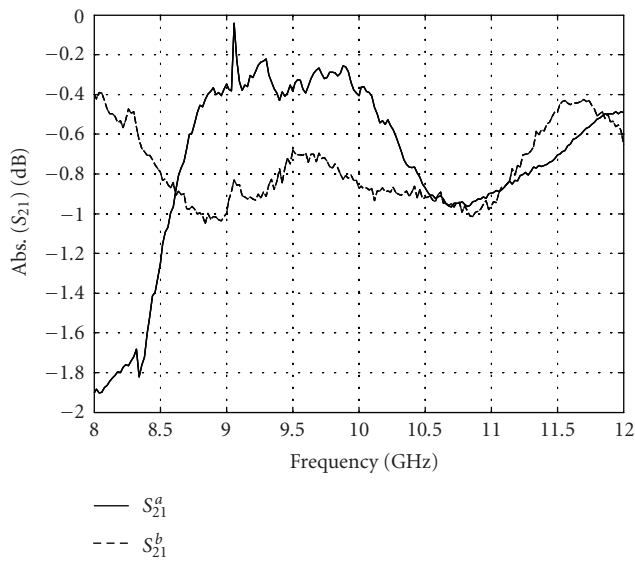
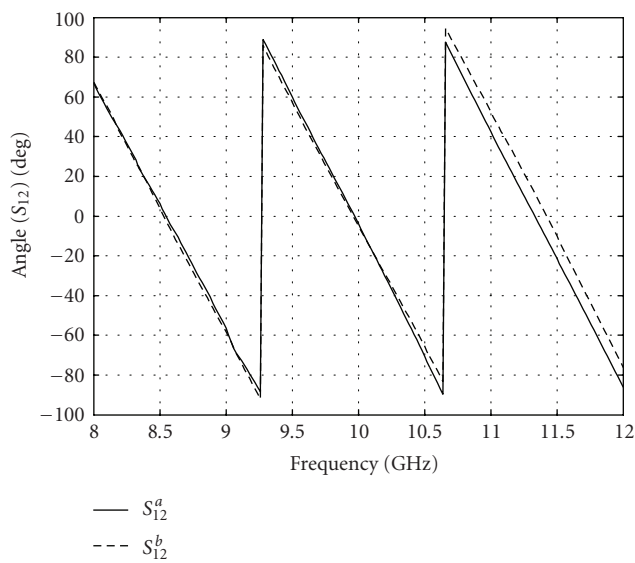


FIGURE 5: Reflection measurements for S^a .



(a)



(b)

FIGURE 6: S_{12}^a and S_{12}^b used for compensation of measurements.

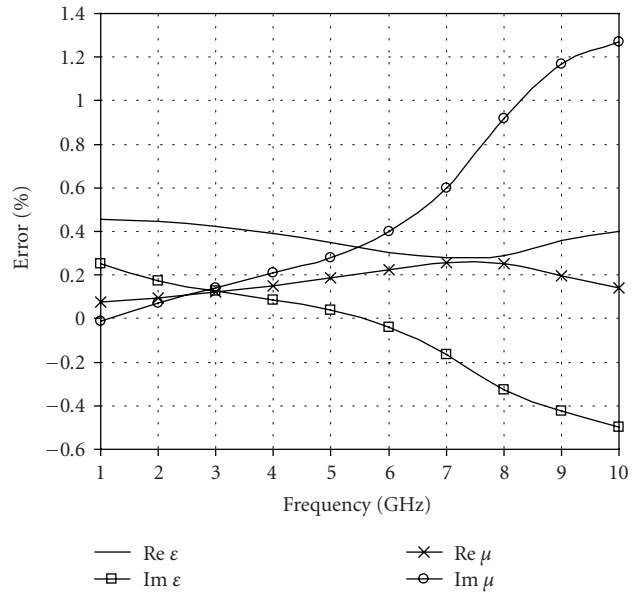


FIGURE 7: Higher mode propagation effect.

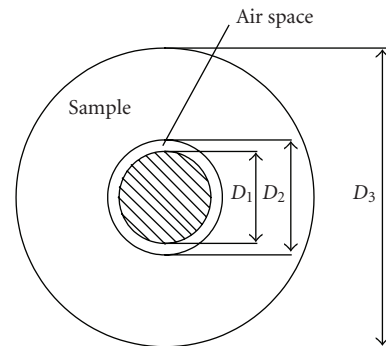


FIGURE 8: Sample diameters for air gap correction.

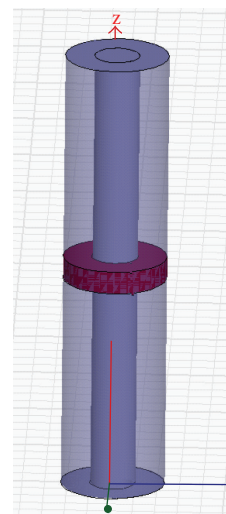


FIGURE 9: HFSS model of sample holder.

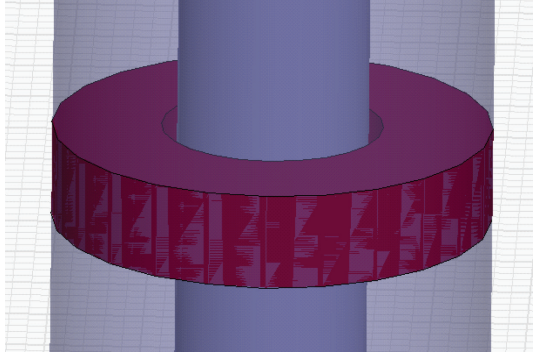


FIGURE 10: Modeling of sample air gap.

where Γ_{m1} and Γ_{m2} are the two measured reflection coefficients for S^a using short load at two different positions:

$$\begin{aligned} S_{11}^e &= S_{11}^a + S_{21}^a \cdot e^{-j2kd} \cdot S_{22}^b \frac{1}{1 - S_{22}^a \cdot S_{22}^b \cdot e^{-j2kd}} S_{12}^a, \\ S_{21}^e &= S_{21}^a \cdot e^{-jkd} \frac{1}{1 - S_{22}^a \cdot S_{22}^b \cdot e^{-j2kd}} S_{21}^b. \end{aligned} \quad (7)$$

The solutions for the four unknowns are

$$(S_{22}^a)_{1,2} = \frac{-K_1(e^{-j2kl} + e^{-j2kd}) \pm \sqrt{Q - Z}}{2 \cdot (K_2 e^{-j2kd} + K_1 e^{-j2k(l+d)})}, \quad (8)$$

$$S_{12}^a = \sqrt{\frac{(S_{11}^e - \Gamma_{m1})(1 + S_{22}^a)(1 - e^{-j2kd} \cdot (S_{22}^a)^2)}{1 + S_{22}^a \cdot e^{-j2kd}}}, \quad (9)$$

$$S_{11}^a = \Gamma_{m1} + \frac{(S_{12}^a)^2}{1 + S_{22}^a}, \quad (10)$$

$$S_{12}^b = \frac{S_{21}^e (1 - e^{-j2kd} (S_{22}^a)^2)}{S_{12}^a \cdot e^{-jkd}}, \quad (11)$$

where $Q = K_1^2(e^{-j2kl} + e^{-j2kd})^2$ and $Z = 4(K_1 - K_2)(K_2 e^{-j2kd} + K_1 e^{-j2k(l+d)})$,

$$\begin{aligned} K_1 &= \frac{\Gamma_{m2} - \Gamma_{m1}}{1 - e^{-j2kl}}, \\ K_2 &= S_{11}^e - \Gamma_{m1}, \\ |S_{22}^a| &\leq 1. \end{aligned} \quad (12)$$

Figure 6 shows the angle of S_{12}^a and S_{12}^b evaluated from (9) and (11) and based on calibration measurements. There is only a slight difference between them which gives proofs to the previous assumptions (3)–(5) but also confirms the small deviation in length and geometry between the two connector parts.

2.2. Measurement errors

The main sources of errors are the higher-order modes propagating on the coaxial sample holder, measuring line and the sample size with placement errors.

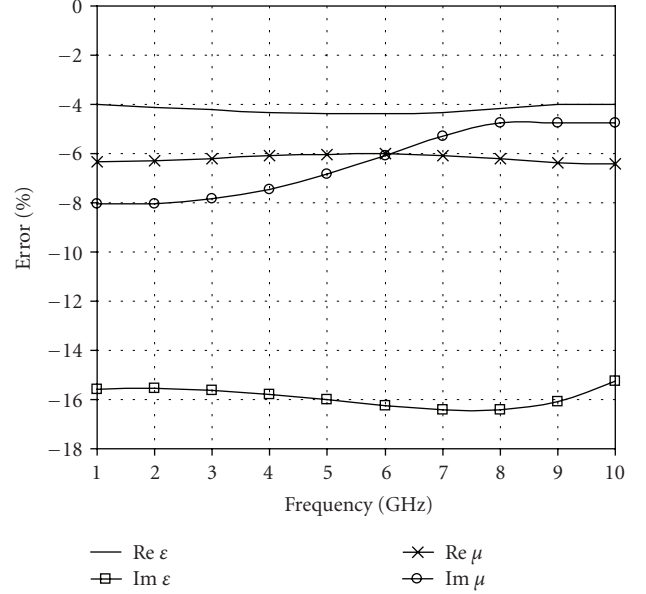


FIGURE 11: Material parameter measurement error caused by 0.1 mm air gap.

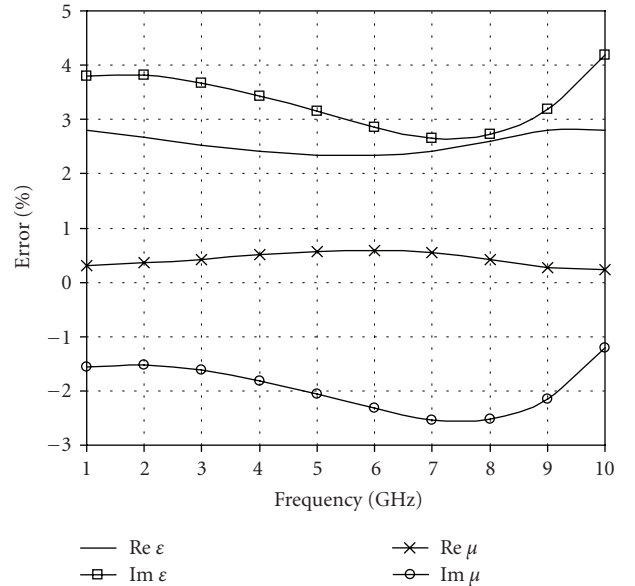


FIGURE 12: Measurement error corrected.

2.2.1. Higher mode propagation

The higher modes can be suppressed using smaller diameter coaxial line. This effect is illustrated in Figure 7 using 7/3 mm coaxial line outer/inner diameters. The relative measurement error for typical high-frequency ferrite material ($\epsilon = 2 - 0.8j$, $\mu = 5 - 1j$) is below 1.5%. The error reduction or the measurement frequency extension is possible by reducing the measurement line diameter.

The main effect was investigated and analyzed, which is related to the sample size and causes the main errors in measurements.

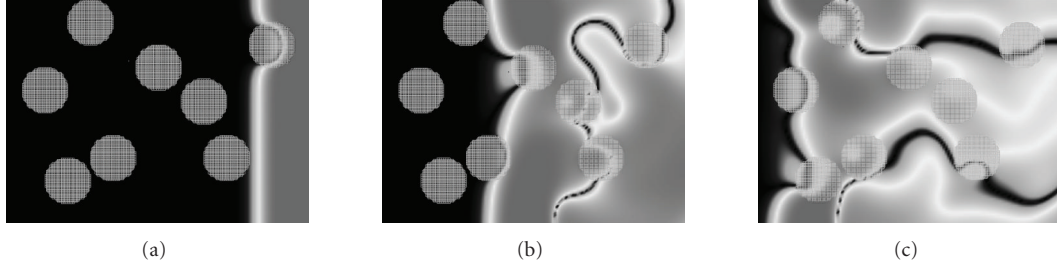


FIGURE 13: Plane wave propagating between randomly distributed small particles.

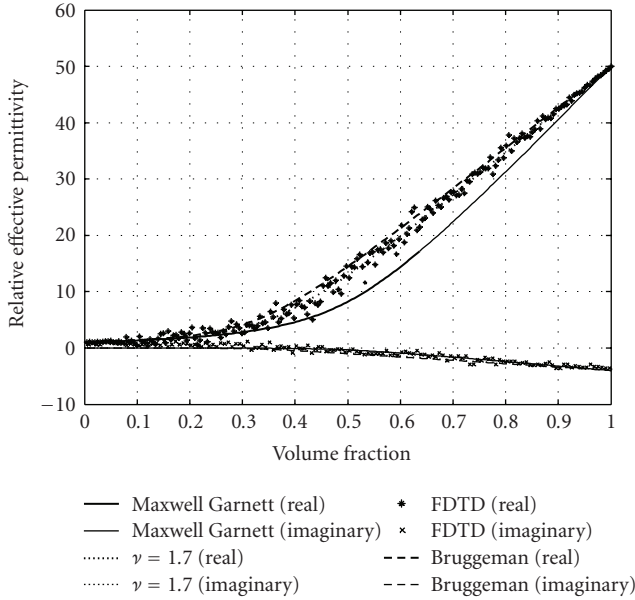


FIGURE 14: Mixing rules and FDTD simulation results of material mixture.

2.2.2. The effect of air gap between the sample and the coaxial line

The effect of a small air gap caused by manufacturing tolerances was investigated. The measuring error is more significant in case if the air gap is at the inner conductor of the coaxial line so this effect was analyzed.

The effect causes error in permittivity and permeability. The error in permittivity can be corrected with a simple correction routine. The corrected values are

$$\begin{aligned} \text{Re } \epsilon_{\text{corr.}} &= \text{Re } \epsilon_{\text{meas.}} \frac{\ln(D_3/D_2)}{\ln(D_3/D_1) - \text{Re } \epsilon_{\text{meas.}} \ln(D_2/D_1)}, \\ \text{Im } \epsilon_{\text{corr.}} &= \text{Re } \epsilon_{\text{corr.}} \frac{\text{Im } \epsilon_{\text{meas.}}}{\text{Re } \epsilon_{\text{meas.}}} \left(1 + \text{Re } \epsilon_{\text{corr.}} \frac{\ln(D_2/D_1)}{\ln(D_3/D_2)} \right). \end{aligned} \quad (13)$$

Similar expressions can be derived for the permeability correction.

For proving the correction equations, simulations were performed using the HFSS 3D simulator and using the arrangement in Figures 9-10.

The effect of 0.1 mm air gap on the electrical parameters is shown in Figure 11, where the imperfect sample size is modeled and from the HFSS simulated S_{11} and S_{12} values the ϵ and μ were calculated using (1)-(2). Then the correction equations (13) are used and the remaining errors are presented in Figure 12.

With the above correction, the measuring error can be decreased to 4% in the frequency range of 1–10 GHz for typical materials for air gap less than 0.1 mm.

3. MICROSCOPIC MATERIAL PARAMETERS

The material parameters of small sizes of particles in nano-materials cannot be measured directly by using the conventional measuring methods, thus indirect procedure is suggested. The nanoparticles are solved in known fluid material and in known volume fraction.

Estimating of material parameters of particles in host materials there exist different mixing rules depending on particle interaction effects. The main mixing rules are

Maxwell Garnett mixing rule

$$\epsilon_{\text{eff}} = \epsilon_e + 2f\epsilon_e \frac{\epsilon_i - \epsilon_e}{\epsilon_i + \epsilon_e - f(\epsilon_i - \epsilon_e)}, \quad (14)$$

and Bruggeman mixing rule [2]

$$(1-f) \frac{\epsilon_e - \epsilon_{\text{eff}}}{\epsilon_e + 2\epsilon_{\text{eff}}} + f \frac{\epsilon_i - \epsilon_{\text{eff}}}{\epsilon_i + 2\epsilon_{\text{eff}}} = 0, \quad (15)$$

where ϵ_{eff} is the effective permittivity of the mixture, where spherical inclusions with permittivity ϵ_i occupy a volume fraction f in a host material ϵ_e .

The Maxwell Garnett and Bruggeman are the special cases of a general mixing rule

$$\frac{\epsilon_{\text{eff}} - \epsilon_e}{\epsilon_{\text{eff}} + 2\epsilon_e + \nu(\epsilon_{\text{eff}} - \epsilon_e)} = f \frac{\epsilon_i - \epsilon_e}{\epsilon_i + 2\epsilon_e + \nu(\epsilon_{\text{eff}} - \epsilon_e)}. \quad (16)$$

The ν dimensionless parameter $\nu = 1$ gives the Maxwell Garnett rule, $\nu = 2$ gives the Bruggeman formula, and $\nu = 3$ gives the coherent potential approximation.

A similar mixing formula (Bruggeman) can be obtained for the permeability

$$f \frac{\mu_i - \mu_{\text{eff}}}{\mu_i + \mu_{\text{eff}}} + (1-f) \frac{\mu_e - \mu_{\text{eff}}}{\mu_e + \mu_{\text{eff}}} = 0, \quad (17)$$

where μ_{eff} is the effective permeability of the mixture, and spherical inclusions with permeability μ_i occupy a volume fraction f in a host material μ_e .

Two-dimensional simulation using an FDTD solver is applied to prove and illustrate the indirect nanoparticle material parameter determination method. Small particles are randomly distributed in two-dimensional areas and an incident wave is propagating on this area, influenced by them. From simulated macroscopic material parameters (16), (17) are verified and the ν is determined for practical application [3, 4].

The FDTD simulation results show an effective permittivity, which is close to Bruggeman's approximation but using an error minimization $\nu = 1.7$ gives an optimum curve (for $\varepsilon_i = 50 - j*4.0$, $\varepsilon_e = 2.0 - j*0$).

4. CONCLUSION

The main steps of characterization and measurement of microwave absorbent materials in the 1–10 GHz range are introduced for macroscopic and microscopic material parameter determination. The coaxial reflection-transmission type of material parameter measurement is analyzed in detail and measurement error is corrected. Genetic algorithm concept of optimization multilayer antireflection coating is summarized. Two-dimensional FDTD simulations were presented to model the behavior of mixed electric and magnetic type of material.

ACKNOWLEDGMENTS

This work was supported by the ACE2 European FP6 framework program and OMF0252/2007 Project.

REFERENCES

- [1] L. Nagy, "An improved TDR method for determining material parameters," in *Proceedings of the 13th General Assembly of the International Union of Radio Science (URSI '90)*, Prague, Czechoslovakia, August 1990.
- [2] D. A. G. Bruggeman, "Berechnung verschiedener physikalischer Konstanten von heterogenen Substanzen. I. Dielektrizitätskonstanten und Leitfähigkeiten der Mischkörper aus isotropen Substanzen," *Annalen der Physik*, vol. 416, no. 7, pp. 636–664, 1935.
- [3] K. K. Kärkkäinen, A. H. Sihvola, and K. I. Nikoskinen, "Analysis of a three-dimensional dielectric mixture with finite difference method," *IEEE Transactions on Geoscience and Remote Sensing*, vol. 39, no. 5, pp. 1013–1018, 2001.
- [4] K. K. Kärkkäinen, A. H. Sihvola, and K. I. Nikoskinen, "Effective permittivity of mixtures: numerical validation by the FDTD method," *IEEE Transactions on Geoscience and Remote Sensing*, vol. 38, no. 3, pp. 1303–1308, 2000.

Research Article

Prospects of 4H-SiC Double Drift Region IMPATT Device as a Photo-Sensitive High-Power Source at 0.7 Terahertz Frequency Regime

Moumita Mukherjee,¹ Nilratan Mazumder,² and Sitesh Kumar Roy³

¹ Centre of Advanced Study in Radiophysics and Electronics, University of Calcutta 1, Girish Vidyaratna Lane, Kolkata 700009, India

² International Institute of Information Technology, Visva Bharati University, X-1, 8/3, Block-EP, Sector V, Salt Lake Electronics Complex, Kolkata 700091, India

³ Centre of Millimeterwave Semiconductor Devices and Systems, Centre of Advanced Study in Radiophysics and Electronics, University of Calcutta 1, Girish Vidyaratna Lane, Kolkata 700009, India

Correspondence should be addressed to Moumita Mukherjee, mou_mita_m@yahoo.com

Received 4 December 2007; Accepted 14 March 2008

Recommended by Tibor Berceci

The dynamic performance of wide-bandgap 4H-SiC based double drift region ($p^{++}pnm^{++}$) IMPATT diode is simulated for the first time at terahertz frequency (0.7 Terahertz) region. The simulation experiment establishes the potential of SiC based IMPATT diode as a high power ($2.5 \times 10^{11} \text{ Wm}^{-2}$) terahertz source. The parasitic series resistance in the device is found to reduce the RF power output by 10.7%. The effects of external radiation on the simulated diode are also studied. It is found that (i) the negative conductance and (ii) the negative resistance of the diode decrease, while, the frequency of operation and the quality factor shift upward under photoillumination. Holes in 4H-SiC based IMPATT are found to dominate the modulation activities. The inequality in the magnitude of electron and hole ionization rates in the semiconductors may be correlated with these findings.

Copyright © 2008 Moumita Mukherjee et al. This is an open access article distributed under the Creative Commons Attribution License, which permits unrestricted use, distribution, and reproduction in any medium, provided the original work is properly cited.

1. INTRODUCTION

Terahertz (THz) science and technology are rapidly developing all over the world. There is strong interest in the exploitation of the THz frequency range in virtually all fields of basic natural science (physics, chemistry, and biology) as well as medicine [1]. Terahertz applications and technologies for operation in the range between 300 GHz to 10 THz (1 millimeter to 30 micrometers) are attracting increased interest from military and security fields. Scientists all over the world are searching for high-power solid-state sources that can be employed as efficient THz source. Impact avalanche transit time (IMPATT) diodes are the most powerful solid-state sources at mm and sub-mm-wave frequencies and are widely used in various civilian and space communication systems as well as in high-power radars, missile seekers, and so forth. The conventional IMPATT diodes fabricated on gallium arsenide (GaAs) and silicon (Si) are found to be reliable, but these are limited by power and operating frequencies due to the fundamental

limitations of the material parameters. To meet the gradual demand of high-power THz solid-state sources, extensive research is being carried out for development of high-power (Watt level) IMPATT devices that can be operated at high-frequency region. One approach is to employ power combining technique to increase the output power of the IMPATT devices, but it is practically difficult to combine large number of devices. The other option is to develop IMPATT devices from wide bandgap (WBG) semiconductors having high-critical electric field (E_C) and high-thermal conductivity (K) [2]. High value of E_C as well as high-saturation drift velocity of charge carriers ($v_{sn,sp}$), is essential criterion for selecting suitable base semiconductor material for IMPATT fabrication, since the RF power density (P_{RF}) of an IMPATT device is proportional to $E_C^2 \cdot v_s^2$. Moreover, to achieve good thermal stability in THz devices, the base material should have high value of thermal conductivity (K) also. Considering all these facts, WBG semiconductor silicon carbide (SiC) is an automatic choice for designing of high-power IMPATT, because this material offers at least

(i) $10 \times E_c$, (ii) $1.5 \times v_s$, and (iii) $3 \times K$, in comparison to those of conventional Si, GaAs, and indium phosphide (InP). That means, SiC IMPATTs are likely to produce $400 \times P_{RF}$ than its counterparts. The expected excellent performances of WBG SiC-based devices can be assessed by figures of merit (FOM). Keyes' FOM considers the speed of transistors and their thermal limitation, and Johnson's FOM considers the high-frequency and high-power capability of devices. Taking Keyes' and Johnson's FOM for Si as unity, the Keyes' and Johnson's FOM for GaAs are 0.45 and 7.1, respectively, while those of 4H-SiC are 5.1 and 278 [2]. Following the FOMs for high-frequency and high-temperature operation SiC is found to be superior to both Si and GaAs. The availability of 4H-SiC polytypes in bulk wafer form [3, 4] has helped SiC to emerge as relatively mature wide bandgap semiconductor technologies. So, in the light of the maturity of the fabrication technology and the unique material parameters, WBG semiconductors, especially, SiC appear to be the best choice, overall, for the next decade of device development particularly at THz region. At low-frequency region, the superiority of 4H-SiC-based IMPATT over the traditional IMPATTs is already reported [5]. But the prospects of SiC as high-power THz source are still not explored. The authors in this paper have reported for the first time the potential of 4H-SiC as a suitable base material for THz IMPATT device. Presently, two SiC polytypes are popular in SiC research: 6H-SiC and 4H-SiC. Although both the polytypes have similar properties, 4H-SiC is preferred over 6H-SiC because the carrier mobilities in 4H-SiC are isotropic, that is, identical along the two planes (parallel and perpendicular to c -axis) of the hexagonal semiconductor, whereas in 6H-SiC, carriers exhibit anisotropic mobility. Moreover, it is already reported that the high-frequency performance of 4H-SiC IMPATT is far better than its 6H-SiC counterpart in terms of V_B as well as P_{RF} [6]. Thus, the possibility of generating high power from an IMPATT has been investigated by studying the DC and small-signal properties of WBG 4H-SiC-based flat profile DDR (double drift region, $p^{++} p n n^{++}$) IMPATT diode simulated for operation at THz regime.

Parasitic positive series resistance (R_S) is a crucial parameter that limits power dissipation and causes burn out problem in high frequency IMPATTs. Apart from the contribution from substrate, the p-n junction diode parameters, especially, the width of the depletion layer, doping density, and so forth, also contribute to R_S . Moreover, the contact resistance of the device contributes significantly to the total parasitic series resistance. The authors have determined the value of R_S of the simulated IMPATT device considering contribution from the substrates, undepleted epitaxial layer and ohmic contacts. The authors have evaluated the values of R_S for the designed diode through a generalized simulation technique, and its effect on exploitable power level of the device has also been simulated.

Optical control of the dynamic properties of THz IMPATT device can have tremendous application in advanced radars and space communication systems. Basic process involved is that, when a photon (due to optical /other radiation) of energy $h\nu$ greater than the bandgap of the

semiconductor is absorbed at the edges of the reversed biased p-n junction of an IMPATT diode, creation of additional electron-hole pairs takes place within the active region of the diode. These photogenerated carriers give rise to photocurrent and thereby enhance the existing thermal leakage current in the IMPATT diode. The enhanced leakage current alters the avalanche phase delay in the diode, which subsequently modifies the phase and magnitude of terminal current in the device oscillator circuit. The previous experimental [7] as well as theoretical [5, 6] studies on optically illuminated IMPATT diodes indicated that the photogenerated carriers reduce the efficiency and power output of the devices, but increase the tuning range of the devices in the mm-wave frequency band. Moreover, a recent report on the effect of ionizing radiation on Si IMPATT diode characteristics establishes that control of IMPATT performance by any external radiation is an emerging technique that is currently being explored for important application possibilities [8]. These interesting results for photoilluminated IMPATTs have prompted the authors to investigate theoretically the role of external radiation in modulating the dynamic properties of the 4H-SiC DDR THz IMPATT. A modified simulation scheme has been used for this purpose.

2. THEORY OF SIMULATION TECHNIQUE

The simulation method consists of three parts: (i) dc analysis, (ii) small-signal analysis, and (iii) simulation technique for studying illumination effect. The IMPATT diode is basically a p-n junction diode that operates when it is reverse-biased to avalanche breakdown condition. A one-dimensional model of the p-n junction has been considered in the present analysis. The following assumptions have been made in the simulation of dc and small-signal behavior of 4H-SiC DDR IMPATT diodes: (i) the electron and hole velocities have been taken to be saturated and independent of the electric field throughout the space charge layer, (ii) the effect of carrier space-charge has been considered, and (iii) the effect of carrier diffusion has been neglected.

4H-SiC DDR diode is first designed and optimized through a generalized double iterative simulation technique used for analysis of IMPATT action [9]. The method involves iteration over the magnitude of field maximum (E_m) and its location in the depletion layer. The electric field and carrier current profiles are obtained through simultaneous solution of Poisson and current continuity equations. The experimental values of material parameters, namely, realistic field dependence of ionization rates, saturated drift velocities, and mobility of charge carriers in 4H-SiC [10] are incorporated in the present analysis. The junction temperature is assumed to be 300 K. The device dimensions, doping, and current densities of the diode (shown in Table 1) are optimized for operation at around 700 GHz after several computer runs.

The small-signal analysis of the IMPATT diode is carried out through a double iterative simulation technique [9], used to solve two second-order differential equations involving diode resistance (Z_R) and reactance (Z_X). The small-signal admittance characteristics (negative conductance ($-G$))

TABLE 1: Design parameters of 4H-SiC impatt at thz frequency.

DDR diode type	Doping conc. (n region) (10^{24} m^{-3})	Doping conc. (p region) (10^{23} m^{-3})	Width of the n region (nm)	Width of the p region (nm)	Current density (10^{10} A m^{-2})
4H-SiC	3.0	3.0	80.0	80.0	1.37

versus susceptance (B) plots), device negative resistance, and device quality factor ($Q = B/G$) of the optimized SiC DDR diode are determined by this technique after satisfying the appropriate boundary conditions [11]. The total integrated negative resistance (Z_R) and reactance (Z_X) of the diodes at a particular frequency ω can be determined from the numerical integration of the resistivity (R) and the reactivity (X) profiles over the depletion layer (depletion layer width is w) as follows:

$$Z_R = \int_0^w R dx, \quad (1)$$

$$Z_X = \int_0^w X dx.$$

Diode impedance is expressed as $Z(x, \omega) = R(x, \omega) + jX(x, \omega)$.

Moreover, the total diode impedance $Z_{\text{total}}(\omega)$ is obtained by

$$Z_{\text{total}}(\omega) = \int_0^w Z(x, \omega) dx = Z_R + jZ_X. \quad (2)$$

The diode total negative conductance (G) and susceptance (B) have been calculated from the following expressions:

$$G = -\frac{Z_R}{(Z_R)^2 + (Z_X)^2}, \quad B = \frac{Z_X}{(Z_R)^2 + (Z_X)^2}. \quad (3)$$

G and B are function of RF voltage (V_{RF}) and frequency such that the steady-state condition for oscillation is given by [12]

$$g(\omega) = -G(\omega) - \{B(\omega)\}^2 R_S(\omega), \quad (4)$$

where g is load conductance. G , B , and g are normalized to the area of the diode. The relation provides minimum uncertainty in g at low-power oscillation threshold. The authors have evaluated R_S from the admittance characteristics using the realistic analysis of Gummel and Blue [13], and Alderstein et al. [12] without any drastic assumption. Under the small-signal condition, V_{RF} (amplitude of the RF swing) has been taken as $V_B/2$, assuming 50% modulation of the breakdown voltage V_B . For such a small value of V_{RF} , R_S has been calculated by considering the value of g nearly equal to the diode conductance (G) at resonance. The maximum RF power density (P_{RF}) from the device is obtained from the expression:

$$P_{\text{RF}} = \frac{V_{\text{RF}}^2 G_P}{2}. \quad (5)$$

The diode negative conductance at the optimum frequency ($-G_p$) is normalized to the area of the diode. The space step for the present simulation technique is set

as $\sim 10^{-10}$ m. The validity of this simulation method was reported earlier for subterahertz and THz IMPATT diodes [11, 14].

The leakage current (J_s), entering the depletion region of the reversed biased p-n junction of an IMPATT diode, is normally due to thermally generated electrons and holes [$J_s = J_{ns(\text{th})} + J_{ps(\text{th})}$], and it is so small that electron and hole current multiplication factor,

$$M_{n,p} = \frac{J_0}{[J_{ns(\text{th})} \text{ or } J_{ps(\text{th})}]}, \quad [J_0 = \text{bias current density}] \quad (6)$$

can be considered to be infinitely large. Thus, the enhancement of the leakage current under optical illumination of the devices is manifested as the lowering of M_n , p . In a DDR IMPATT structure, the composition of photocurrent may be altered by shining a laser beam selectively on the p^{++} or n^{++} side of the device through fabricated optical windows of appropriate diameter, keeping the diode mounted in a microwave cavity. Thus, the electron saturation current and also the hole saturation current might be enhanced separately, which would produce changes in the small-signal behavior of SiC-based device. The top mounted (TM) and flip chip (FC) structures, shown in Figure 1, illustrate the optical illumination schemes for generation of electron and hole dominated photocurrents, respectively. In order to assess the role of leakage current in controlling the dynamic properties of 4H-SiC IMPATT oscillators, simulation studies are carried out by the authors on the effect of M_n (keeping M_p very high $\sim 10^6$) and M_p (keeping M_n very high $\sim 10^6$) on (i) the small signal negative conductance, (ii) the RF power, and (iii) device negative resistance (Z_{RP}) of flat profile 4H-SiC DDR IMPATT. The details of mathematical calculations based on modified boundary conditions due to enhancement of leakage current are described elsewhere [11].

3. RESULTS AND DISCUSSIONS

The optimized design parameters of the unilluminated SiC DDR IMPATT diode for which M_n and M_p are both large ($= 10^6$) are mentioned in the last section. The DC and high-frequency properties of the simulated diode are reported in Table 2 and will be discussed first. Table 2 shows that the THz IMPATT diode based on SiC breaks down at 55.3 V. The simulated diode is capable of generating a maximum P_{RF} of $2.8 \times 10^{11} \text{ Wm}^{-2}$ with efficiency 10.5 %.

Table 3 shows the value of R_S at 0.7 THz for the simulated diode. The small-signal values of negative conductance (G), susceptance (B), and expected values of load conductance (g , at low-power oscillation threshold) are also reported in Table 3. The value of R_S for 4H-SiC IMPATT is found

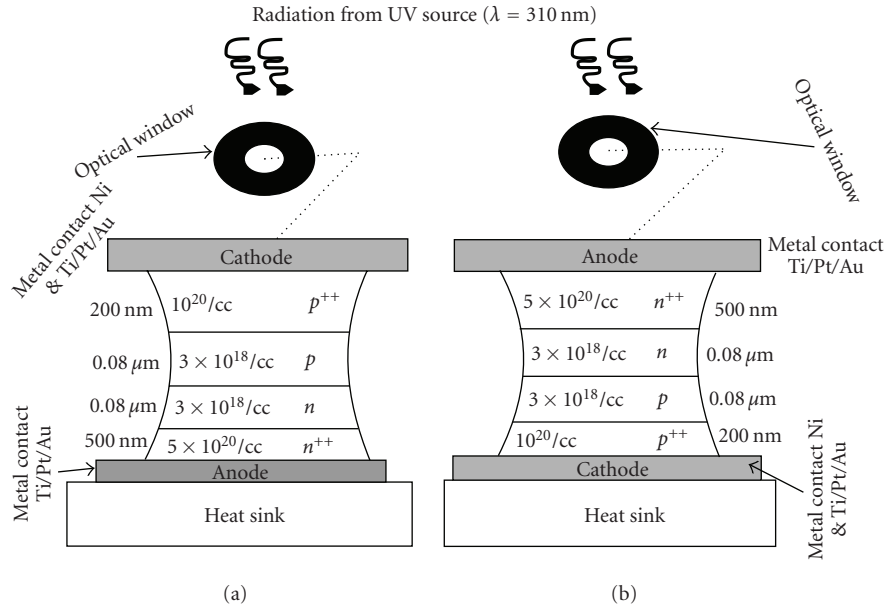


FIGURE 1: Schematic diagram of (a) top mounted and (b) flip chip DDR IMPATT diode under optical-illumination.

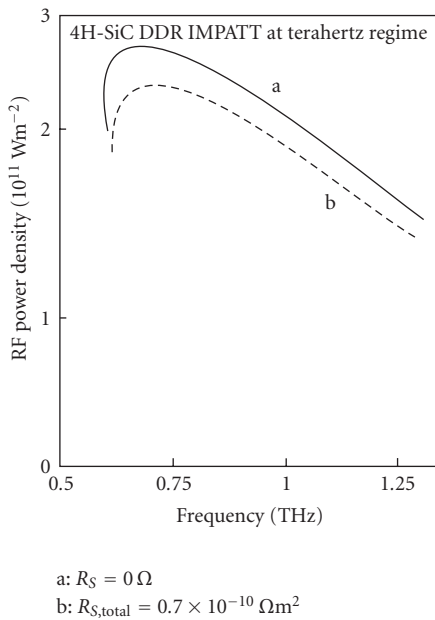


FIGURE 2: Effect of series resistance on RF power density of 4H-SiC Terahertz IMPATT diode.

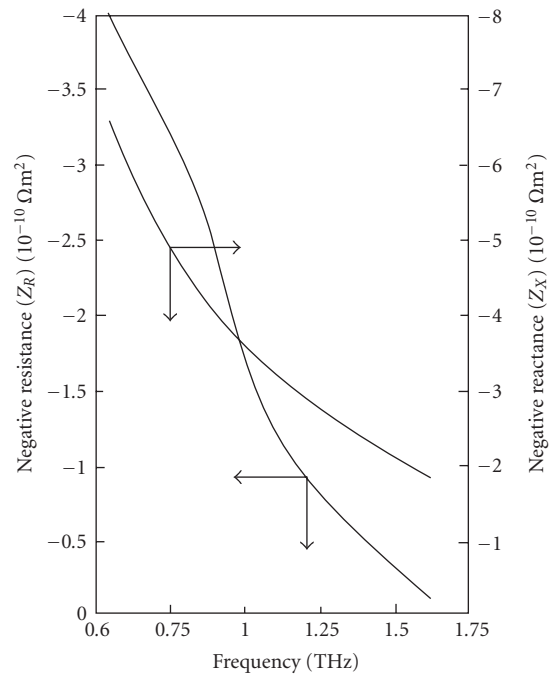


FIGURE 3: Impedance plots of 4H-SiC IMPATT diode at Terahertz region.

to be $0.49 \times 10^{-10} \Omega m^2$. Ohmic contact resistance may put a severe restriction on the high frequency (THz level) performance of the wide bandgap IMPATT devices and thus the presence of contact resistance should be included in the realistic consideration of parasitic positive series resistance. A very recent study showed that ohmic contact to n-SiC are formed by using pure Ni-based layer with a thin underlying Si layer. By this technique, a stable and low n-SiC contact resistivity of $\sim 10^{-7} \Omega cm^2$ can be realized in practice [15].

Very low specific contact resistance for p-SiC has not been achieved in reality. Using alloy composition such as Ni/Al to p-SiC, a contact resistivity $\sim 10^{-6} \Omega cm^2$ can be realized in practice [16]. It is noteworthy to mention that, in order to get appreciable power (Watt level) from a THz source, low specific contact resistance ($\sim 10^{-7} \Omega cm^2$) should be achieved, since at THz region intrinsic diode negative resistance is usually very small. It may be predicted that, further increasing the doping concentration of p-SiC semiconductor

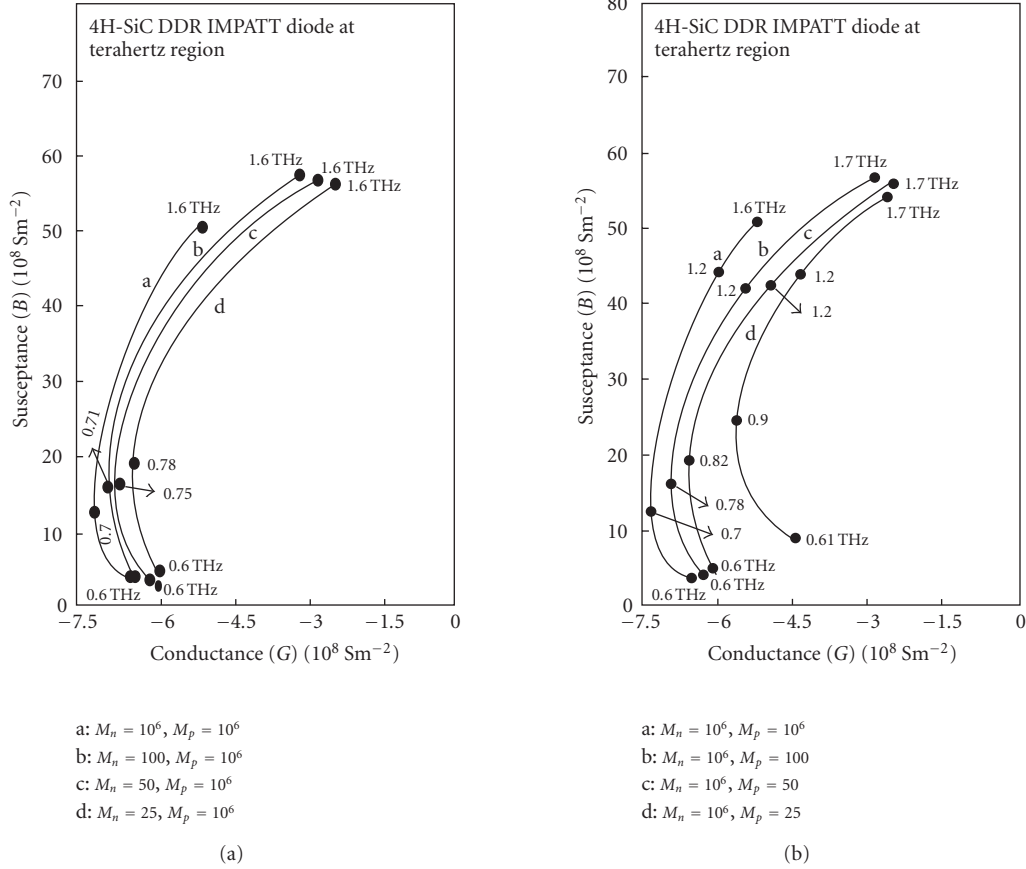


FIGURE 4: (a) Effect of electron dominated photo-current on 4H-SiC DDR IMPATT diode at terahertz region. (b) Effect of hole dominated photo-current on 4H-SiC DDR IMPATT diode at terahertz region.

TABLE 2: DC and small-signal properties of 4H-SiC IMPATT diode.

Diode parameters	4H-SiC DDR IMPATT
E_m (10^8 V m $^{-1}$)	5.25
V_B (V)	55.3
η (%)	10.5
f_p (THz)	0.7
$-G_p$ (10^8 S m $^{-2}$)	7.40
$-Q_p$	1.6
P_{RF} ($R_s = 0.0 \Omega$) (10^{11} Wm $^{-2}$)	2.8
P_{RF} ($R_{s,total} = 0.7 \Omega$) (10^{11} Wm $^{-2}$)	2.5

material, a desired contact resistivity $\sim 10^{-7} \Omega \text{ cm}^2$ may be achieved in reality. Hence, more realistic values of effective parasitic series resistance ($R_{S,total}$, including the contribution of contact resistance) become approximately $0.7 \times 10^{-10} \Omega \text{ m}^2$ for 4H-SiC IMPATT. Measurement of such a low contact resistance may be possible with transmission line measurement (TLM) technology. The effect of $R_{S,total}$ on P_{RF} of the diode is shown in Figure 2. It is reflected in Figure that even in the presence of aforesaid $R_{S,total}$ an appreciable RF power density of $2.5 \times 10^{11} \text{ Wm}^{-2}$ may be obtained from the simulated THz device.

Figure 3 shows the small-signal impedance plot for the THz diode. The graphs show that the device possesses negative resistance for all frequencies above the avalanche frequency (f_a), where its reactance is capacitive. This is due to the fact that, in the oscillating frequency range, the magnitude of Z_R is found to be small compared to Z_X . This is also evident from Figure 3, that the values of $|-Z_R|$ and $|-Z_X|$ decrease as the operating frequency increases.

The effects of electron and hole dominated photocurrents on the THz performance of the WBG IMPATT are presented in Table 4. The table shows that the values of $|-G_p|$ of the diode decrease with the lowering of M_n and M_p . At the same time, the frequency range over, which the device exhibits negative conductance, shifts towards higher frequencies with the lowering of M_n as well as M_p . The output data for illuminated TM and FC flat DDR IMPATT diodes (see Table 4) indicate that the value of negative conductance at peak frequency $|-G_p|$ decreases by 6.7% when M_n reduces from 10^6 to 25 for SiC-based THz device, while for the similar lowering of M_p , $|-G_p|$ decreases by 23.0%. The identical trend is reflected in Figures 4(a) and 4(b), where the admittance plots of SiC-based photoilluminated THz device are plotted. The figures show that the effect of hole dominated photocurrent in modulating the admittance characteristics is much prominent than the

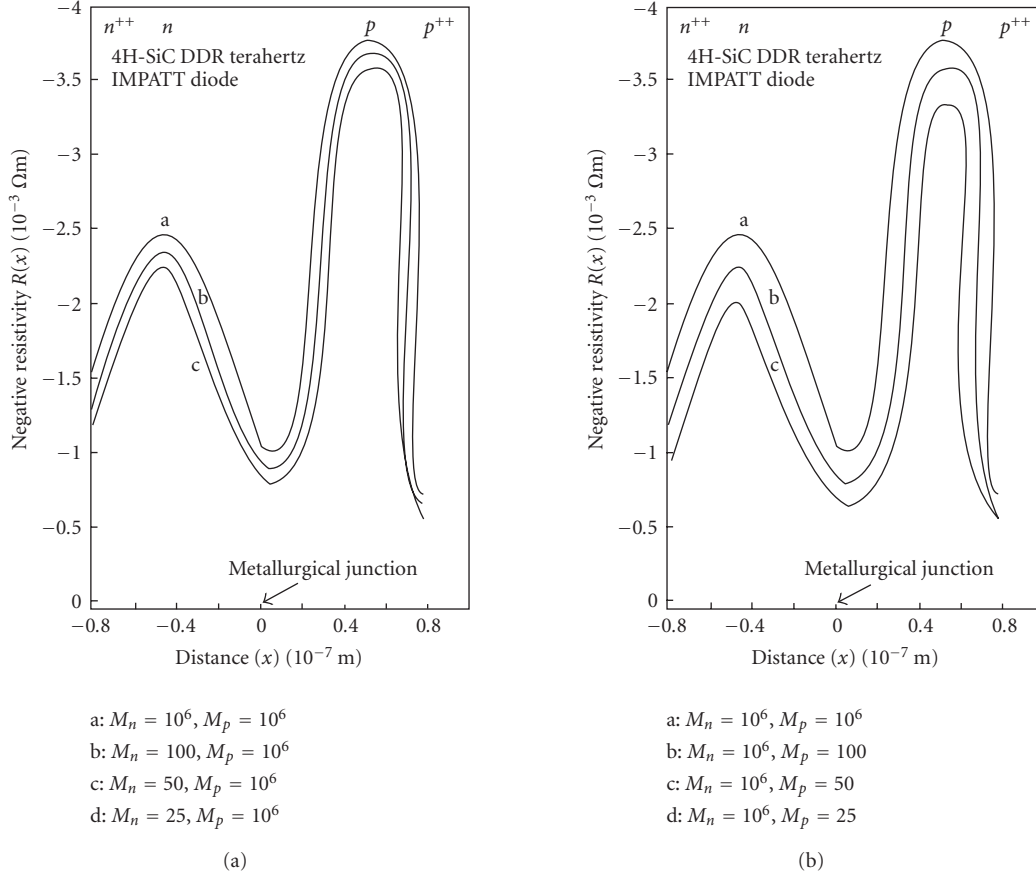


FIGURE 5: (a) Effect of electron dominated photo-current on negative resistivity profile of 4H-SiC DDR IMPATT diode. (b) Effect of hole dominated photo-current on negative resistivity profile of 4H-SiC DDR IMPATT diode.

TABLE 3: Series resistance of 4H-SiC IMPATT at 0.7 THz.

Negative conductance ($-G$) (10^8 Sm^{-2})	Susceptance (B) (10^8 Sm^{-2})	Load conductance (10^8 Sm^{-2})	Series resistance (R_S) ($10^{-10} \Omega\text{m}^2$)	Negative resistance ($-Z_R$) ($10^{-10} \Omega\text{m}^2$)
7.4	12.0	6.7	0.49	3.8

electron dominated photocurrent. The optimum frequency of oscillation (f_p) for the illuminated SiC diode increases by 11.4% as M_n reduces from 10^6 to 25. However, for the similar variation of M_p , the upward shift of f_p is much higher (29.0%).

Figures 5(a) and 5(b) show the profiles of negative resistivity at the peak frequencies corresponding to different values of M_n ($M_p = 10^6$) and M_p ($M_n = 10^6$) for SiC-based diode, respectively. Negative resistivity profiles give a physical insight into the region of the depletion layer that contributes to RF power. In each case, the profiles are characterized by two negative resistivity peaks in the middle of the two drift layers of the diode interspaced by a dip in the avalanche region. It is observed from the figures that due to the enhancement of electron and hole photocurrents, the negative resistivity peaks in the electron, and hole drift layers are depressed gradually. It is also found that the

decrease in the magnitude of the negative resistivity peaks is more pronounced for variation of M_p corresponding to hole dominated photocurrent than for the same variation of M_n corresponding to electron dominated photocurrent.

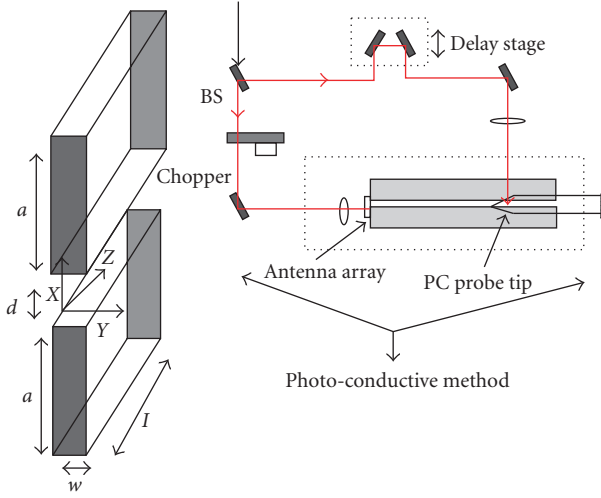
Simulation study also depicts that in case of 4H-SiC DDR IMPATT, as M_n is decreased from 10^6 to 25, there occurs a 54.0% decrease in the diode negative resistance ($-Z_{Rp}$). On the other hand, as M_p changes from 10^6 to 25, $-Z_{Rp}$ reduces by 74.3% (see Table 4).

The variations of power output with optimum frequency for different values of M_n and M_p are also shown in Table 4. Again, it is found from the study that the magnitude of device quality factor at optimum frequency of oscillation $| -Q_p |$ increases appreciably for a decrease of M_p compared to the same change of M_n values (see Table 4).

The enhancement of leakage currents by electron and hole dominated photocurrents thus leads to a decrease of

TABLE 4: Variation of small-signal properties of 4H-SiC DDR IMPATT under optical-illumination.

M_n	M_p	f_p (THz)	$-G_p$ (10^8 Sm^{-2})	$-Z_{Rp}$ ($10^{-10} \Omega \text{ m}^2$)	P_{RF} (10^{11} Wm^{-2})	$-Q_p$
10^6	10^6	0.70	7.4	3.8	2.82	1.6
100	-	0.71	7.2	2.6	2.75	2.08
50	-	0.75	7.1	2.1	2.71	2.39
25	-	0.78	6.9	1.7	2.63	2.75
10^6	100	0.78	7.0	2.5	2.67	2.14
-	50	0.82	6.4	1.6	2.45	2.97
-	25	0.90	5.7	0.95	2.18	4.2

FIGURE 6: Waveguide geometry: $d = 270 \mu\text{m}$, $w = 300.0 \mu\text{m}$, and $l = 140.0 \text{ mm}$.

$-Z_{Rp}$, $-G_p$, and P_{RF} along with a simultaneous upward shift of f_p . While the photo-generated leakage current dominated by holes modulates the DC and high-frequency properties of the device appreciably, that dominated by electrons has relatively less effect in modulating the same. For the mm-wave Si DDR, it was reported that the electron saturation current was more dominant in changing the P_{RF} and the f_p [7]. In Si, the electron ionization rate is greater than the hole ionization rate. This means that by controlling the DDR IMPATT action through more ionizing carriers in Si, a higher frequency shift may be achieved. By the same logic, it can also be concluded that in 4H-SiC, holes are more ionizing carriers than electrons, since 4H-SiC DDR IMPATT under optical illumination at THz region is more sensitive to hole dominated photocurrent. This relative predominance of hole leakage current in optical control of 4H-SiC DDR IMPATT performance can be attributed to the inequality of the ionization coefficient values in 4H-SiC [10].

The thermal conductivity of 4H-SiC ($\sim 500 \text{ W m}^{-1} \text{ K}^{-1}$) is very high. This helps the SiC IMPATT to dissipate the generated heat quickly from the junction. Moreover, if a diamond heat sink is employed for the practical realization of 4H-SiC THz IMPATT device, the effective thermal conductivity will increase to such a high value that the junction temperature will not increase significantly over the ambient (300 K), though the device yields a P_{RF} of $2.5 \times 10^{11} \text{ Wm}^{-2}$.

Due to lack of any experimental data on SiC THz IMPATT diode, the simulation results could not be compared. However, the nature of variation of THz properties of the designed diode under photoillumination has a trend agreement with the experimental results of Si-based IMPATT diode at lower frequency region. It may be mentioned here that a large-signal computer simulation may provide improved quantitative information regarding the influence of optical illumination on the frequency tuning as well as RF power output, but the nature of response to optical illumination, as predicted by the small-signal analysis, will remain unchanged.

4. CONCLUSION

The current simulation study establishes that 4H-SiC-based DDR IMPATT diode can generate high power even at a frequency as high as 0.7 THz. In the earlier reported paper [14], the frequency of operation was limited to 0.5 THz only. Moreover, in the present paper, the authors have realistically simulated the value of total parasitic series resistance for THz SiC IMPATT, which includes the contribution both from the diode as well as from ohmic contact resistance, while, in the previous article [14], the series resistance due to contact metals was not considered. Based on the information of total series resistance, provided in this paper, one can get more accurate idea of exploitable power level from the SiC DDR diode at THz region. Further, the effect of external radiation on this device at 0.7 THz seems to be significantly prominent. It is thus expected that the photo-irradiated 4H-SiC DDR IMPATT at still higher frequencies will have better frequency tuning capability. A discussion on feasibility of experimental validation was not incorporated in the previous article [14]. In the present paper, the authors will discuss below the possibility of experimental verification of optical illumination on the 4H-SiC DDR diode. The realization of 4H-SiC THz IMPATT diode may be done through the following process steps.

Device fabrication following usual process steps like photolithography, deposition of metal contacts, and mesa formation by reactive ion etching.

Characterization of THz properties may be possible with a dielectric coplanar wave guide, the device being an integral part of the waveguide.

For terahertz (0.1–1 THz) power transmission, a metallic slit waveguide, fabricated by sawing a $270 \mu\text{m}$ wide slit

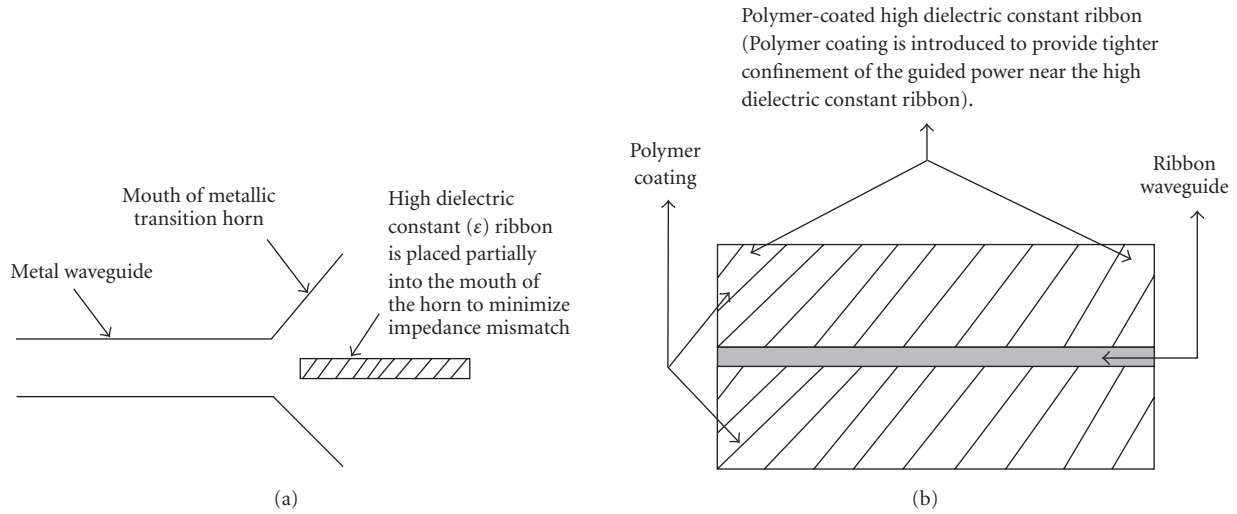


FIGURE 7: (a) Rectangular metal waveguide to high dielectric constant ribbon waveguide transition [17]. (b) Longitudinal cross-sectional geometry of a polymer-coated high dielectric constant ribbon. The thickness and the width of the high dielectric constant ribbon are $0.0635\lambda_0$ and $0.635\lambda_0$, respectively. The thickness of the polymer coating is approx. $0.25\lambda_0$, and the width is approx. $0.635\lambda_0$. The dielectric constant of the ribbon is 10 while that of the polymer is 2.04 [17].

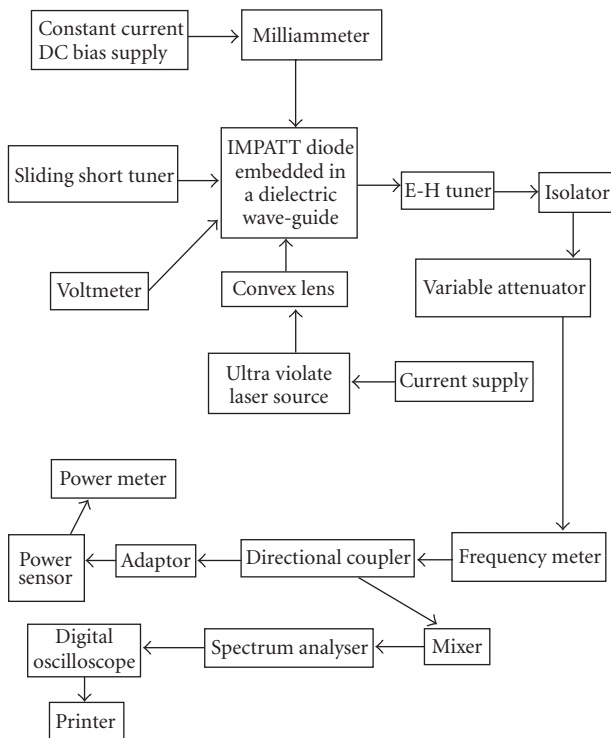


FIGURE 8: Experimental setup for optical illumination experiment on 4H-SiC IMPATT diode at THz region.

through a 140 mm wide and 300 μm thick silicon slabs may be used (see Figure 6) [18]. For higher frequency (3 THz) power transfer, a ribbon-like structure fabricated from ceramic alumina may be utilized [17]. The schematic diagrams of the structures are shown in Figures 7(a) and 7(b).

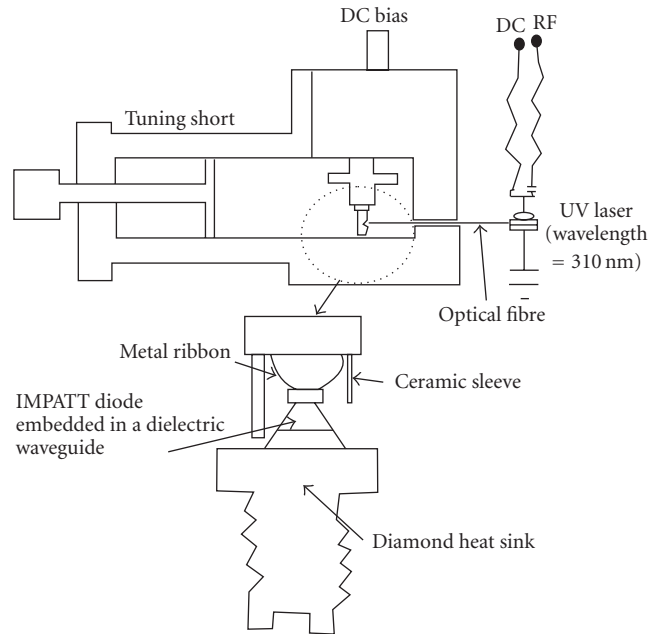


FIGURE 9: Optical experimental setup for THz IMPATT diode.

Measurements of THz power and frequency may be done with a THz vector network analyzer (VNA) or, by employing photoconductive method (as shown in right-hand diagram of Figure 6).

An arrangement similar to that shown in Figures 8 and 9, appropriately modified to include the photoconductive detection of THz power and frequency, can be used for optical illumination experiment on 4H-SiC IMPATT. The intensity of radiation may be experimentally increased by a convex lens as indicated in Figure 8.

It is concluded that these findings may be utilized for realizing optically integrated THz modules for effective applications in THz communication and in interstellar explorers.

ACKNOWLEDGMENTS

The authors (Moumita Mukherjee) and (Nilratan Mazumder) wish to express their gratitude to the Director, International Institute of Information Technology, Kolkata for his interest in the work. Moumita Mukherjee is grateful to Defence Research and Development Organisation (DRDO), New Delhi, India for awarding her a Senior Research Fellowship to carry out this work. Preliminary simulation results of Ka-band 4H-SiC IMPATT diodes were published in Proceedings of 12th Microcoll Conference on Microwave Communication, held during May 14–16 2007 in Budapest, Hungary, pp. 187–190.

REFERENCES

- [1] P. H. Siegel, "Terahertz technology," *IEEE Transactions on Microwave Theory and Techniques*, vol. 50, no. 3, pp. 910–928, 2002.
- [2] V. V. Buniatyan and V. M. Aroutiounian, "Wide gap semiconductor microwave devices," *Journal of Physics D*, vol. 40, no. 20, pp. 6355–6385, 2007.
- [3] R. Madar, "Silicon carbide in contention," *Nature*, vol. 430, no. 7003, pp. 974–975, 2004.
- [4] R. Yakimova and E. Janzén, "Current status and advances in the growth of SiC," *Diamond and Related Materials*, vol. 9, no. 3–6, pp. 432–438, 2000.
- [5] M. Mukherjee, N. Mazumder, and A. Dasgupta, "Analysis of photo-illuminated millimeter wave high power IMPATT oscillator," in *Proceedings of the 12th Microcoll Conference on Microwave Communication (MOW '07)*, pp. 187–190, Budapest, Hungary, May 2007.
- [6] M. Mukherjee and N. Mazumder, "Effect of optical illumination on 4H-SiC DDR IMPATT diodes at 140 GHz," in *Proceedings of the 3rd International Conference on Computers and Devices for Communication (CODEC '06)*, pp. 298–301, Kolkata, India, December 2006.
- [7] H. P. Vyas, R. J. Gutmann, and J. M. Borrego, "Effect of hole versus electron photocurrent on microwave—optical interactions in impatt oscillators," *IEEE Transactions on Electron Devices*, vol. 26, no. 3, pp. 232–234, 1979.
- [8] M. B. Tagaev, "Effect of ionizing radiation on the silicon IMPATT diode characteristics," *Turkish Journal of Physics*, vol. 23, no. 6, pp. 985–988, 1999.
- [9] S. K. Roy, M. Sridharan, R. Ghosh, and B. B. Pal, "Computer method for the dc field and carrier current profiles in the IMPATT device starting from the field extremum in the depletion layer," in *Proceedings of the 1st Conference on Numerical Analysis of Semiconductor Devices (NASECODE I)*, J. H. Miller, Ed., pp. 266–274, Dublin, Ireland, June 1979.
- [10] "Electronic Archive: New Semiconductor Materials, Characteristics and Properties," <http://www.ioffe.ru/SVA/NSM/Semicond/SiC>
- [11] M. Mukherjee, N. Mazumder, S. K. Roy, and K. Goswami, "GaN IMPATT diode: a photo-sensitive high power terahertz source," *Semiconductor Science and Technology*, vol. 22, no. 12, pp. 1258–1267, 2007.
- [12] M. G. Adlerstein, L. H. Holway Jr., and S. L. G. Chu, "Measurement of series resistance in impatt diodes," *IEEE Transactions on Electron Devices*, vol. 30, no. 2, pp. 179–182, 1983.
- [13] H. K. Gummel and J. L. Blue, "A small signal theory of avalanche noise in IMPATT diodes," *IEEE Transactions on Electron Devices*, vol. 14, no. 9, pp. 569–580, 1967.
- [14] M. Mukherjee and N. Mazumder, "Optically illuminated 4H-SiC terahertz IMPATT device," *Egyptian Journal of Solids*, vol. 30, no. 1, pp. 87–102, 2007.
- [15] P. Friedrichs, "Technological challenges for manufacturing power devices in SiC," in *Proceedings of the CS MANTECH Conference*, pp. 221–224, Austin, Tex, USA, May 2007.
- [16] H. Vang, M. Lazar, P. Brosseard, et al., "Ni-Al ohmic contact to p-type 4H-SiC," *Superlattices and Microstructures*, vol. 40, no. 4–6, pp. 626–631, 2006.
- [17] C. Yeh, F. Shimabukuro, and P. H. Siegel, "Low-loss terahertz ribbon waveguides," *Applied Optics*, vol. 44, no. 28, pp. 5937–5946, 2005.
- [18] M. Wächter, M. Nagel, and H. Kurz, "Metallic slit waveguide for dispersion-free low-loss terahertz signal transmission," *Applied Physics Letters*, vol. 90, no. 6, Article ID 061111, 3 pages, 2007.

Research Article

Modeling and Measurements of Novel Monolithic Filters

Aly H. Aly,¹ Badawy El-Sharawy,¹ and Adalbert Beyer²

¹ Department of Electrical Engineering, Arizona State University, Tempe, AZ 85287-7206, USA

² Department of Electrical Engineering and Communications, University of Duisburg-Essen, Campus Duisburg, 47057 Duisburg, Germany

Correspondence should be addressed to Adalbert Beyer, adalbert.beyer@uni-duisburg-essen.de

Received 27 December 2007; Accepted 24 June 2008

Recommended by T. Kalkur

This paper presents novel multilayer tuneable high Q -filters based on hairpin resonators including ferroelectric materials. This configuration allows the miniaturization of these filters to a size that makes them suitable for chip and package integration and narrow-band applications. The main focus was miniaturizing filters with coupled loops using multilayer dielectric substrates. A further goal was to increase the quality factor of these distributed filters by embedding high dielectric materials in a multilayer high- and low- k (dielectric constant) substrate that is supported by LTCC technology. An improved W-shape bandpass filter was proposed with a wide stopband and approximately 5% bandwidth.

Copyright © 2008 Aly H. Aly et al. This is an open access article distributed under the Creative Commons Attribution License, which permits unrestricted use, distribution, and reproduction in any medium, provided the original work is properly cited.

1. INTRODUCTION

At microwave frequencies, the parallel-coupled-resonator filters [1] and the hairpin resonator filters [2] are the most widely used filters because of their design, ease of fabrication, and low cost. However, these filters have some disadvantages such as: large size, high loss, especially when the number of coupled resonators is increased, low stopband rejection, and spurious response at the filter's harmonics.

Many filter topologies were explored using coupled-line theory in strip line and microstrip to improve the performance. A cross-coupled topology was proposed [3] to create controlled attenuation poles or transmission zeros by allowing different coupling paths with different phases for the input signal. These transmission zeros are created in the stopband either above, below, or between resonances to enhance filter rejection [4, 5]. A drawback of this technique is the high loss of the filter, especially when zeros are placed near the resonant frequency. Another drawback is the bandwidth asymmetry created from concentration of rejection on one stopband (above or below resonance) and relaxed on the other band. Different coupling schemes for resonator filters were introduced in [6].

Stepped impedance hairpin resonators were introduced in [7] to reduce the resonator size and enhance the performance. In [8], the hairpin resonator's length is further

decreased by capacitive loading at the end of the resonator. The main disadvantage of capacitive loaded resonators is the high loss due to the increased resonator capacitance. This explains why all of the applications of this filter use high-temperature superconductors (HTSs) [9] which have a limited usage in wireless applications. Slow-wave open-loop resonators were presented in [10]. These allow for various elliptic and quasielliptic function responses to be realized at the expense of high insertion loss. This loss limits this filter to HTS applications. Another coupled-line filter using defected ground structure (DGS) was presented in [11] in which a defect in the ground plane below the coupled lines added more transmission zeros to the resonance characteristics of the filter. Utilizing this DGS may not be applicable in terms of filter integration and fabrication. Zigzag hairpin comb resonators have been proposed in [12], to further reduce the size, but the filter is suffering from a very high capacitance from winding the hairpin resonators. This winding increases the losses, which is why this filter was only utilized in HTS technology where conductor loss is of no concern.

Besides the improvement in the resonator structure, feed structures also play an important role in optimizing the performance the filters. Different feed topologies have been used such as: parallel-coupled-feed structure [1], tapped-line [13, 14], and the end-coupled feed structures. Most of the feed structures are capacitively coupled feeds or electric field

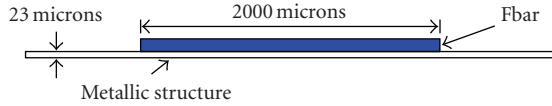


FIGURE 1: FBAR coupled to a microstrip line.

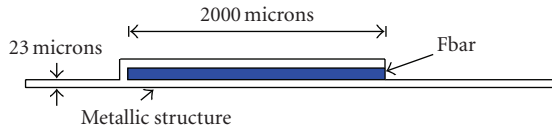


FIGURE 2: FBAR coupled to a microstrip hairpin with side coupling.

coupling, which can increase the overall capacitance of the filter and reduce Q . Optimization of the feed location and length controls the strength of the coupling, which controls bandwidth and Q .

The progress and feasibility of filter integration are usually coupled to filter tuning. Electronic tuning is used to compensate for manufacturing and process variations. Ferroelectric materials have been suggested for both filter tuning and size reduction [15–17]. Most ferroelectric materials have relative dielectric constant greater than 200. There is a tradeoff between material Q and tunableness. Materials like KTaO_3 have high Q , greater than 10 000 but have poor tunableness of less than 1% per $\text{V}/\mu\text{m}$. The preferred choice has been BaSrTiO_3 which has a relative dielectric constant equal or greater than 5000 and tunableness of 20% per $\text{V}/\mu\text{m}$ but has a poor Q of less than 100. The most common design is the lumped element filter with ferroelectric loaded capacitors [17]. This approach yields a low Q of less than 30 due to the low Q of the lumped elements.

This paper describes the properties of a multilayer dielectric mode filter coupled through hairpins to increase coupling and reduce size. Tight coupling is required to achieve low insertion loss. Medium k and high Q material, such as KTaO_3 , is inserted between two layers of high k material such as BaSrTiO_3 . The high k material pulls the fields inside the low k material to enhance both tunableness and Q . The present modes are EM dielectric modes in the ferroelectric material for the design of band-reject filter and oscillator applications.

Now, the paper is organized as follows. Section 2 describes some properties of the dielectric mode hairpin filters. In Section 3, the topic “multilayer filters” is treated. Section 4, an overview of the LTCC technology and the LTCC substrate configuration is shown. Section 5 presents the properties of hair-pin resonator filter. Section 6 presents the fabrication and measurements of different coupled-line filters, and the paper is concluded in Section 7.

2. DIELECTRIC MODE HAIRPIN FILTERS

Simple band-reject filters (BRFs) can be constructed using a dielectric resonator (DR) placed next to a microstrip line or by coupling ferroelectric bars made of KTaO_3 (with a relative dielectric constant of 240 and Q of about 10 000)

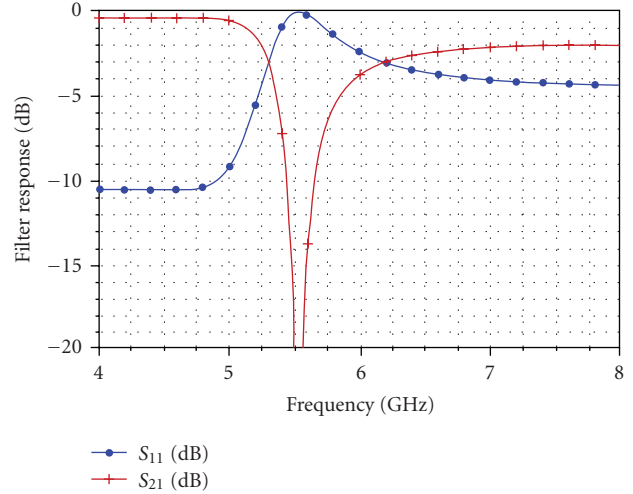


FIGURE 3: Frequency response of an FBAR coupled to a microstrip hairpin with side coupling.

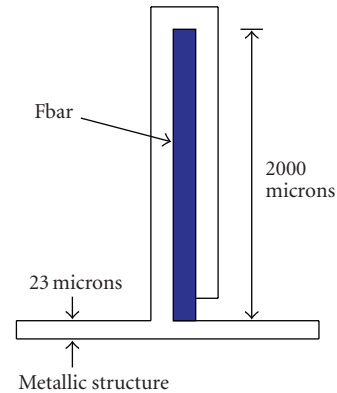


FIGURE 4: FBAR coupled to a hairpin with edge coupling.

to a 50 ohms microstrip line as shown in Figure 1. The present dimensions of the microstrip and ferroelectric bar are required for on-chip integration.

In order to increase the coupling and to enhance the filter characteristics, a hairpin is wrapped around the ferroelectric bar as shown in Figure 2.

The performance of the filter depicted in Figure 2 is calculated versus frequency using the HFSS software package from Ansoft, Pa, USA, and is shown in Figure 3.

A significant improvement in coupling and Q , as compared to the simple bar, is observed.

Next, the hairpin is coupled to the 50 ohms line at an edge of the hairpin as shown in Figure 4. Also the resonant frequency is reduced by a factor of 2 for the same bar dimension. When the field distribution is studied, it has been found that the loop of the hairpin produces a maximum magnetic field in the ferroelectric bar resulting in effectively a virtual ground at the loop. A maximum electric field occurs at the open end. Thus, the dimension of the resonant bar is reduced to $\lambda/4$ instead of $\lambda/2$ as compared to case of a conventional dielectric resonator. To verify the type of mode,

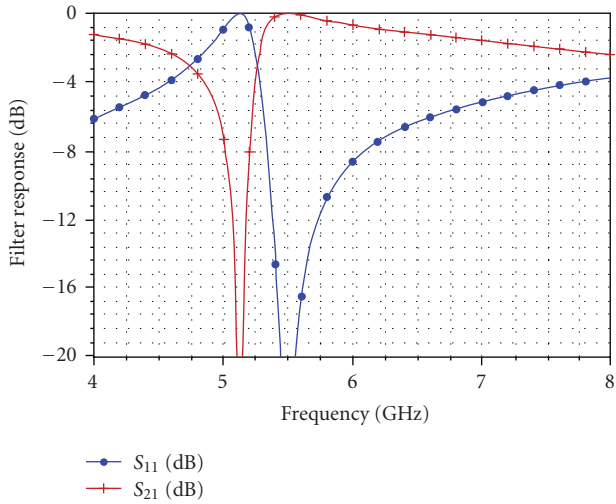


FIGURE 5: Frequency response of an FBAR coupled to a hairpin with edge coupling.

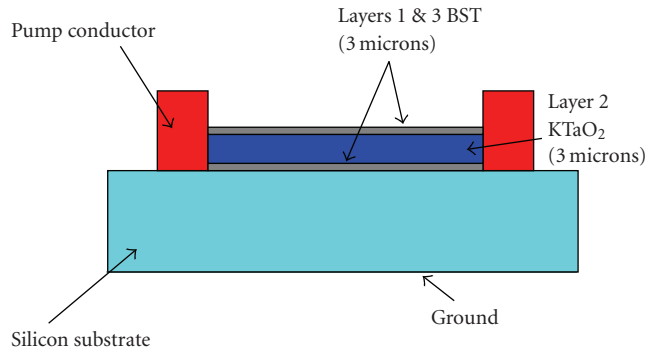


FIGURE 6: Geometry of a multilayer BRF.

the hairpin is coupled to the 50 ohms line at an edge of the hairpin as shown in Figure 4. The resonant frequency did not change significantly, as shown in Figure 5.

3. MULTILAYER FILTERS

The material, which is used in the above-described devices as ferroelectric bars, is made of KTaO_3 (with a relative dielectric constant of 240 and Q of about 10 000), and it has a very poor tuning, but fairly high Q . In order to increase the tunableness, another material, namely, a BaSrTiO_3 layer can be used in conjunction with KTaO_3 as shown in Figure 6. Thus, multilayer filter structures may be obtained.

In all of following simulations, a silicon dioxide substrate was used with an effective dielectric constant of 4 and a thickness of $15 \mu\text{m}$ which gives a 50-ohms microstrip line of $23 \mu\text{m}$ width. The conductor thickness is set to $10 \mu\text{m}$. Ferroelectric bars' width and thickness are optimized to give a high Q .

Figure 7 shows the response of a multilayer filter depicted in Figure 6. Here, a hairpin with $2 \mu\text{m}$ thick BaSrTiO_3 is used.

This picture also shows the new response when a 3-micron KTaO_3 is inserted in the middle of the BaSrTiO_3

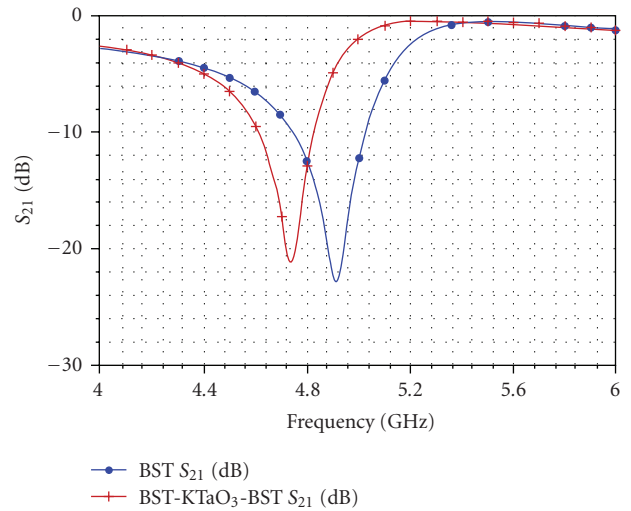


FIGURE 7: Frequency response of a multilayer structure.

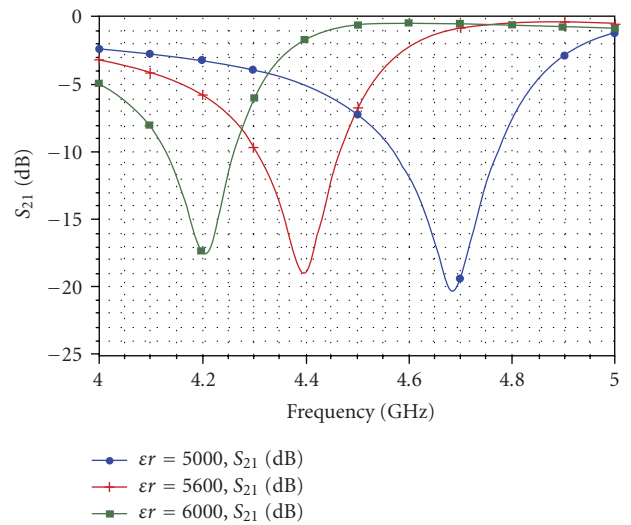


FIGURE 8: Frequency response (S_{21} (dB))—of tunable multilayer structure.

layer. The figure indicates an improvement in Q of up to 20%. The resonant frequency shifted downward as expected.

Subsequently, the tunableness of the multilayer structure is tested by applying a DC voltage between the hairpin and the ground plane of the microstrip line.

A decent tunableness in the order of 5% is predicted for a 20 volt variation in the DC voltage as shown in Figure 8.

4. LTCC SUBSTRATE CONFIGURATION

LTCC is a multilayer ceramic substrate technology. The multilayer architecture can be produced using stacked ceramic tapes that are used to apply conductive, dielectric, and/or resistive parts. These single sheets have to be laminated together and fired in one step at a relatively low temperature. This saves time, money, and reduces circuit dimensions. LTCC technology offers a high level of integration, buried

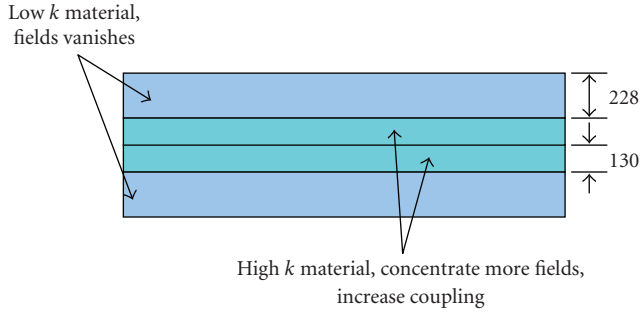


FIGURE 9: Cross-section of substrate layers using LTCC technology.

TABLE 1: LTCC material properties.

Kind of tape	k @ 2.5 GHz	Loss Factor @ 2.5 GHz
Hertape CT 707	6.37	$4.56 \times 10E - 3$
Hertape 765	68.7	$1.73 \times 10E - 3$

components, low loss, and system robustness. LTCC technology has been established in mobile communication techniques in the frequency range of a few GHz. LTCC has been investigated and has developed a good reputation for the high-frequency applications. Examples include: WLAN at 5 GHz [18], radar sensors at 24 GHz and 77 GHz [19], and digital radio networks operating from 20 to 60 GHz [20] have also been reported.

Advances in new materials and fabrication technologies opened a new window in improving filter performance. One of these technologies is LTCC. Due to its thick conductor, losses of the LTCC filter can be reduced. The filter size can be also reduced by using embedded high dielectric-constant substrates. Also, one of the major advantages of using LTCC is its low cost and short fabrication cycle. Filters presented in this paper are formed between a high k material ($k = 65$) followed by a low k material ($k = 6$). Figure 9 shows the cross-sectional area of the mixed k substrate.

Table 1 shows the material properties of the mixed k substrate measured at 2.5 GHz.

5. PROPERTIES OF HAIR-PIN RESONATOR FILTER

Figure 10 shows the concept of using a hair-pin line as a resonator to design a simple bandpass filter (BPF).

A single capacitively coupled hair-pin resonator is used. The folded resonator length is 8800 microns on the LTCC multilayer substrates that are described above. Dimensions of the filter were set to comply with the LTCC design rules. The spacing between the resonator and the capacitive feeds, S , is set to 125 microns, which is the minimum spacing between conductors. The thickness of the conductor is 10 microns. The filter was simulated using the HFSS package. The effective dielectric constant is $\epsilon_{\text{eff}} = 40$ and gives a resonance around 2.66 GHz.

Since the opposite sides of the hairpin resonator have opposite potentials, there is a virtual ground created at the center of the resonator. This makes the filter similar to the comb line filter [9] and makes this filter appropriate for

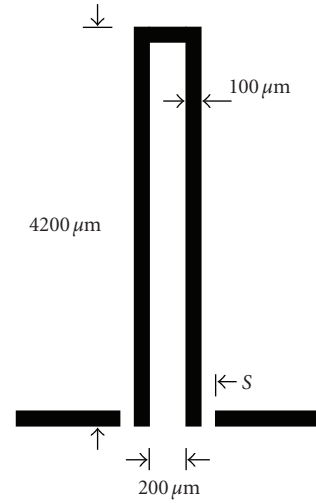


FIGURE 10: A single-resonator hair-pin filter with capacitance coupling at the input and output.

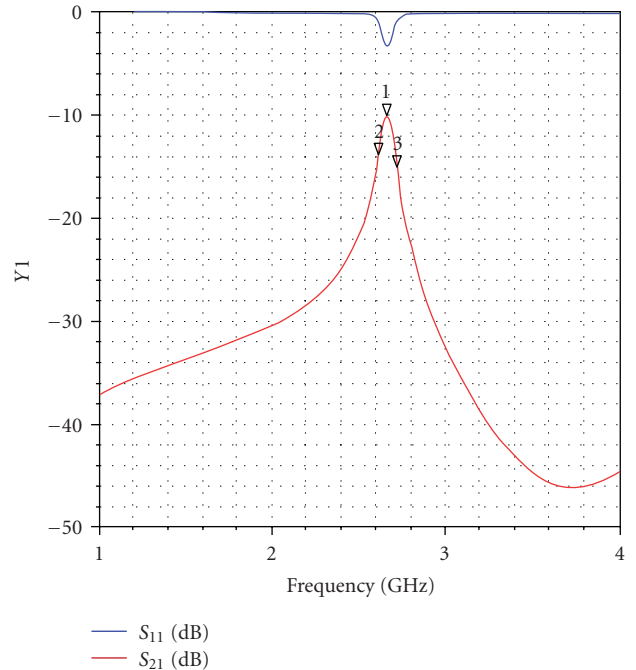


FIGURE 11: Simulated response of single hair-pin resonator filter with capacitive coupling.

planar applications that do not require vias connected to the ground plane.

Simulation results of the filter are shown in Figure 11.

It can be seen from the response of the filter that the insertion loss is very high ($\cong 10$ dB). This is due to the weak coupling between the feeds and the resonator. Weak coupling is desirable for narrow-bandwidth filter, but it comes at the expense of increasing filter loss.

To further illustrate the effect of changing the spacing S , Table 2 shows performance of the filter for different values of S .

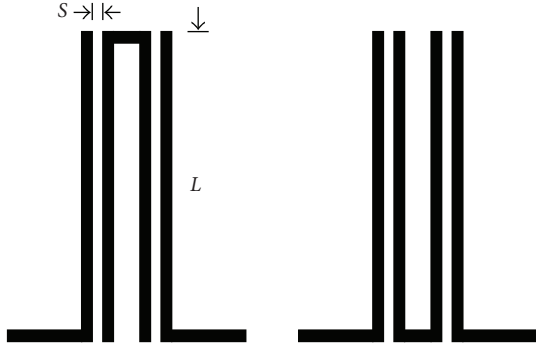


FIGURE 12: Single hair-pin resonator filter having two orientations with parallel coupled-feed lines.

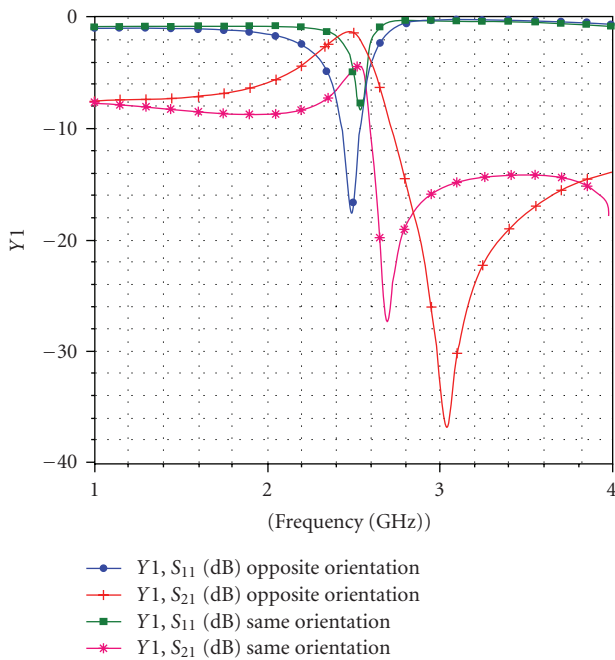


FIGURE 13: Simulated magnitude response of hair-pin resonator filter having two orientations with parallel coupled-feed lines.

TABLE 2: Effect of changing S on the filter response.

$S(\mu\text{m})$	f_r (GHz)	$I.L.$ (dB)	$R.L.$ (dB)	3 dB-B.W. (MHz)
100	2.66	10	3.31	73
50	2.65	6.9	5.17	80
25	2.61	6.25	5.91	91

It can be recognized from the table that there is a tradeoff between insertion loss and bandwidth.

The above discussion explains the basic operation of the hair-pin resonators. It is shown that narrow bandwidth can be obtained by using weak coupling at the expense of the insertion loss. This may render the filter useless in some applications. To increase coupling, parallel feed lines can be used to increase the coupling area. Figure 12 shows a single hair-pin filter with parallel feed lines.

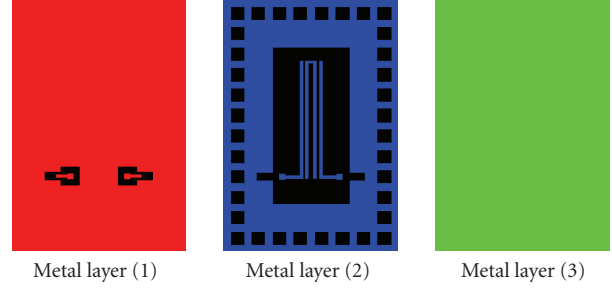


FIGURE 14: Configuration (1): metal layers.

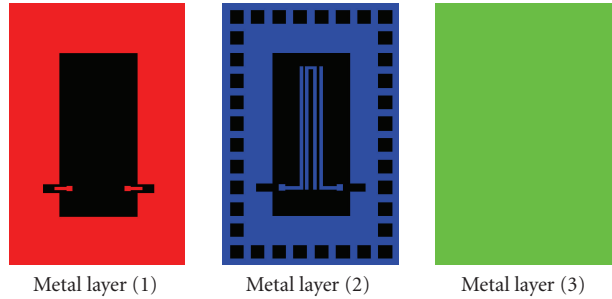


FIGURE 15: Configuration (2): metal layers.

While Figure 12 shows two different orientations of the resonator, with respect to the feed lines, in Figure 13 the responses of the filter are given.

It can be seen from the figure that if a resonator is in the same orientation as the feed line, then it has higher losses. This is because the crowding currents at coupling edges can increase loss [17]. A comparison between the two cases is shown in Table 3 in which the unloaded Q is higher for the opposite orientation.

6. FABRICATION AND MEASUREMENTS OF COUPLED-LINE FILTERS USING LTCC

The proposed coupled-line filter substrates will use embedded high dielectric material to reduce the size, and improve Q . Two filter configurations were considered in this layout. The first configuration is the strip-line configuration. A ground ring was formed around the filter to shield it and to connect the top and bottom metallization as shown in Figure 14.

In this layout, a minimum conductor width of 100 microns and a minimum metal spacing of 125 microns are considered. The second configuration is the microstrip configuration which was the same as configuration (1) without the top ground plane. The metallization of all layers for the second configuration is shown in Figure 15.

With a patch area of 76 mm by 76 mm, several filter structures using strip-line and microstrip, along with a calibration structure, were included in the layout. The latter is done for on-chip calibration and to exclude any parasitic effects in the measurement.

TABLE 3: Properties of the hair-pin resonator filter having two orientations with parallel coupled-feed lines.

	f_r (GHz)	$I.L.$ (dB)	$R.L.$ (dB)	3 dB-B.W. (MHz)	Q_l	Q_{ul}
Opposite orientation	2.47	1.31	17.6	400	6.2	44.2
Same orientation	2.53	4.18	8.39	220	11.5	30.1

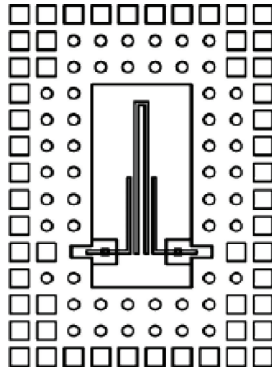


FIGURE 16: Layout of single hair-pin filter with parallel coupled-feed lines.

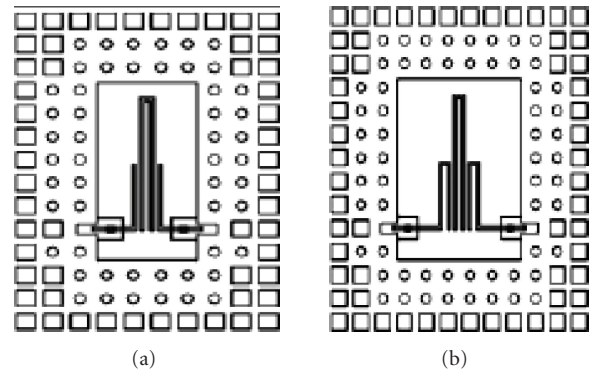
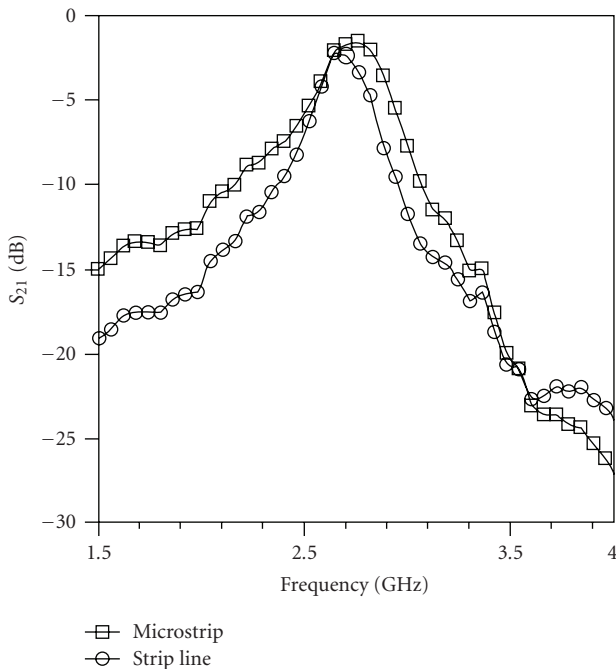


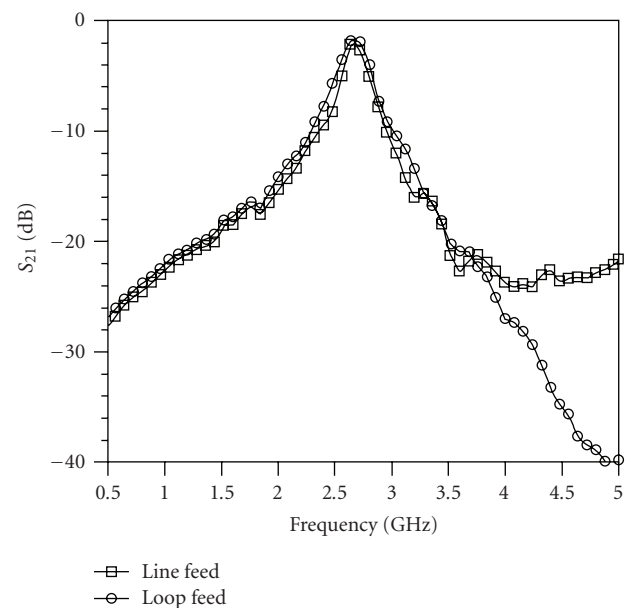
FIGURE 18: Single hair-pin resonator filter with (a) coupled-line feed and (b) loop.

FIGURE 17: S_{21} for single hair-pin filter with (a) strip line, and with (b) microstrip line configuration.

In the following, the measurement results of several coupled-line filters implemented using the mixed- k topology are reported.

6.1. Strip-line versus microstrip

Following the discussion in Section 4 about the parasitic effects on the filter performance, a single hair-pin resonator

FIGURE 19: S_{21} for hair-pin resonator filter with (a) coupled-line feed and (b) loop feeds.

filter with line feed was implemented in both the strip-line and the microstrip configurations. Figure 16 shows the filter layout.

The line feed was about a quarter the length of the hair pin ($\approx \lambda/8$). As predicted previously, the microstrip configuration gave lower losses and a better quality factor than the strip-line configuration due to lower loss in the ground plane. Figure 17 shows the S_{21} for both configurations.

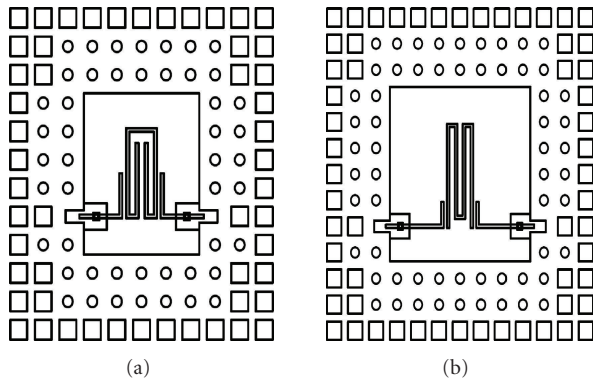


FIGURE 20: (a) Folded resonator, (b) *W*-shape resonator.

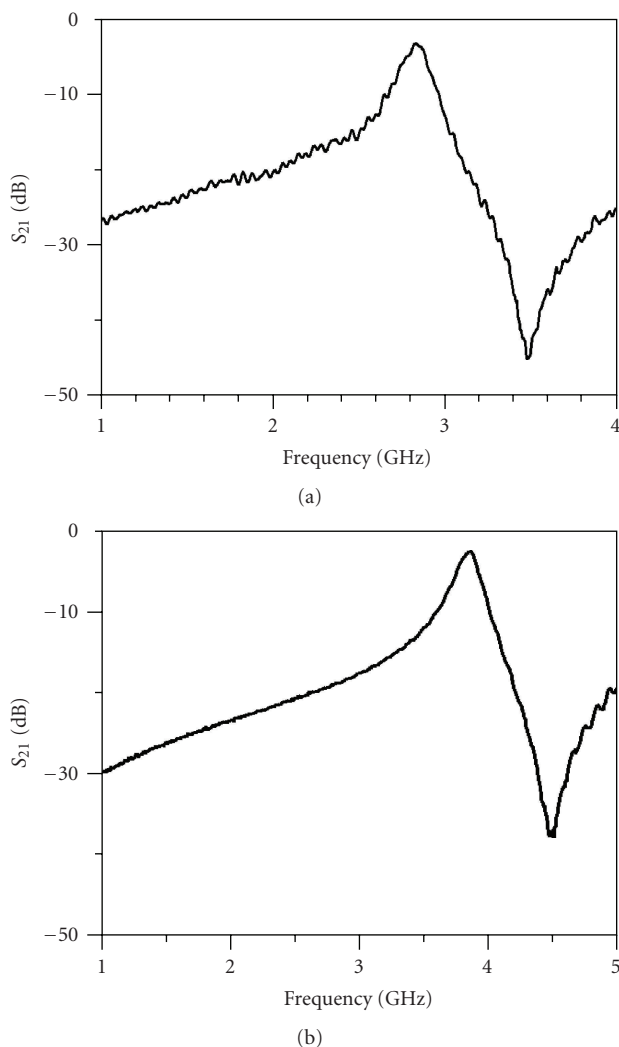


FIGURE 21: S_{21} (dB) for (a) capacitive (folded resonator) and (b) *W*-shape resonator.

6.2. Loop feeds versus coupled-line feeds

To investigate the feasibility of using a loop feed instead of a coupled-line feed, a hair-pin resonator filter was fabricated

using coupled line and loop feeds. Figure 18 shows the filter layout.

The filter responses are shown in Figure 19.

6.3. *W*-shape resonator

To reduce the size and increase Q , a new resonator configuration using the *W*-shape is presented and compared to the existing folded resonator shape as shown in Figure 20.

Results show (see Figure 21) that the *W*-shape resonator filter gives a quality factor of 79 compared to the folded resonator that gave a quality factor of about 58. The higher resonance frequency of the *W*-shape as compared to the folded resonator was an indication of less capacitance.

7. CONCLUSION

In this paper, integration of passive filters on silicon substrates is investigated. Simple hair-pin band reject filters (BRFs), that support dielectric mode, are presented. Ferroelectric bars were used as resonant elements, compared to transmission line hair-pin resonators; an improvement of about 10 in Q is achieved. Multilayer dielectric ferroelectric material is discussed and gives about 5% tunableness. Furthermore, the miniaturization of filters introduced was achieved by using an embedded high- k substrate configuration that is feasible using an LTCC process. An improved *W*-shape bandpass filter was proposed with a wide stopband and approximately 5% bandwidth.

ACKNOWLEDGMENTS

The authors are thankful to the German Government (DFG) for supporting this project. It was performed in frame of a visiting professorship with Duisburg-Essen University, Campus Duisburg, under Subject no. Du 128/15-1.

REFERENCES

- [1] S. B. Cohn, "Parallel-coupled transmission-line-resonator filters," *IRE Transactions on Microwave Theory and Techniques*, vol. 6, no. 2, pp. 223–231, 1998.
- [2] E. G. Cristal and S. Frankel, "Hairpin-line and hybrid hairpin-line/half-wave parallel-coupled-line filters," *IEEE Transactions on Microwave Theory and Techniques*, vol. 20, no. 11, pp. 719–728, 1972.
- [3] A. E. Williams, "A four-cavity elliptic waveguide filter," *IEEE Transactions on Microwave Theory and Techniques*, vol. 18, no. 12, pp. 1109–1114, 1970.
- [4] J. B. Thomas, "Cross-coupling in coaxial cavity filters—a tutorial overview," *IEEE Transactions on Microwave Theory and Techniques*, vol. 51, no. 4, part 2, pp. 1368–1376, 2003.
- [5] R. Levy, "Filters with single transmission zeros at real or imaginary frequencies," *IEEE Transactions on Microwave Theory and Techniques*, vol. 24, no. 4, pp. 172–181, 1976.
- [6] U. Rosenberg and S. Amari, "Novel coupling schemes for microwave resonator filters," in *IEEE MTT-S International Microwave Symposium Digest*, vol. 3, pp. 1605–1608, Seattle, Wash, USA, June 2002.

- [7] M. Makimoto and S. Yamashita, "Bandpass filters using parallel coupled stripline stepped impedance resonators," *IEEE Transactions on Microwave Theory and Techniques*, vol. 28, no. 12, pp. 1413–1417, 1980.
- [8] M. Sagawa, K. Takahashi, and M. Makimoto, "Miniaturized hairpin resonator filters and their application to receiver front-end MICs," *IEEE Transactions on Microwave Theory and Techniques*, vol. 37, no. 12, pp. 1991–1997, 1989.
- [9] G. L. Matthaei, N. O. Fenzi, R. J. Forse, and S. M. Rohfing, "Hairpin-comb filters for HTS and other narrow-band applications," *IEEE Transactions on Microwave Theory and Techniques*, vol. 45, no. 8, part 1, pp. 1226–1231, 1997.
- [10] J.-S. Hong and M. J. Lancaster, "Theory and experiment of novel microstrip slow-wave open-loop resonator filters," *IEEE Transactions on Microwave Theory and Techniques*, vol. 45, no. 12, part 2, pp. 2358–2365, 1997.
- [11] J.-S. Park, J.-S. Yun, and D. Ahn, "A design of the novel coupled-line bandpass filter using defected ground structure with wide stopband performance," *IEEE Transactions on Microwave Theory and Techniques*, vol. 50, no. 9, pp. 2037–2043, 2002.
- [12] G. L. Matthaei, "Narrow-band, fixed-tuned, and tunable bandpass filters with zig-zag hairpin-comb resonators," *IEEE Transactions on Microwave Theory and Techniques*, vol. 51, no. 4, part 1, pp. 1214–1219, 2003.
- [13] E. G. Cristal, "Tapped-line coupled transmission lines with applications to interdigital and combline filters," *IEEE Transactions on Microwave Theory and Techniques*, vol. 23, no. 12, pp. 1007–1012, 1975.
- [14] J. S. Wong, "Microstrip tapped-line filter design," *IEEE Transactions on Microwave Theory and Techniques*, vol. 27, no. 1, pp. 44–50, 1979.
- [15] G. Torregrosa-Penalva, G. López-Risueño, and J. I. Alonso, "A simple method to design wide-band electronically tunable combline filters," *IEEE Transactions on Microwave Theory and Techniques*, vol. 50, no. 1, pp. 172–177, 2002.
- [16] I. Vendik, O. Vendik, V. Pleskachev, A. Svishchev, and R. Wördenweber, "Design of tunable ferroelectric filters with a constant fractional band width," in *IEEE MTT-S International Microwave Symposium Digest*, vol. 3, pp. 1461–1464, Phoenix, Ariz, USA, May 2001.
- [17] A. Tombak, F. T. Ayguavives, J.-P. Maria, G. T. Stauf, A. I. Kingon, and A. Mortazawi, "Tunable RF filters using thin film barium strontium titanate based capacitors," in *IEEE MTT-S International Microwave Symposium Digest*, vol. 3, pp. 1453–1456, Phoenix, Ariz, USA, May 2001.
- [18] L. Lecheminoux and N. Gosselin, "Advanced design, technology & manufacturing for high volume and low cost production," in *Proceedings of the IEEE/CPMT 28th International Electronics Manufacturing Technology Symposium (IEMT '03)*, pp. 255–260, San Jose, Calif, USA, July 2003.
- [19] S. Holzwarth, R. Kulke, J. Kassner, and P. Uhlig, "Antenna integration on LTCC radar module for automotive applications at 24 GHz," in *The IMAPS Nordic Conference*, Helsingør, Denmark, September 2004.
- [20] R. Kulke, G. Möllenbeck, W. Simon, A. Lauer, and M. Ritweger, "Point-to-multipoint transceiver in LTCC for 26 GHz," in *The IMAPS Nordic Conference*, pp. 50–53, Stockholm, Sweden, September-October 2002.